



UNIVERSITEIT VAN PRETORIA
UNIVERSITY OF PRETORIA
YUNIBESITHI YA PRETORIA

**THE EXPERIMENTAL AND NUMERICAL INVESTIGATION OF THE INFLUENCE OF
SHAFT ROTATION ON LEAKAGE RATE OF NON-CONTACTING SEALS FOUND IN
TURBINE APPLICATIONS**

by

Jacobus Johannes Fourie WIID

Submitted in partial fulfilment of the requirements for the degree
Masters of Engineering (Mechanical Engineering)

in the

Department of Mechanical and Aeronautical Engineering
Faculty of Engineering, Built Environment and Information Technology

UNIVERSITY OF PRETORIA

Supervisors:

Prof KJ Craig

Dr CJH Thiart

Date of submission
February 2018

Abstract

THE EXPERIMENTAL AND NUMERICAL INVESTIGATION OF THE EFFECT OF SHAFT ROTATION ON LEAKAGE RATE OF NON-CONTACTING SEALS FOUND IN TURBINE APPLICATIONS

by

Jacobus Johannes Fourie WIID

Supervisors: Prof K.J. Craig

Dr C.J.H. Thiart

Department: Mechanical and Aeronautical Engineering

University: University of Pretoria

Degree: Master of Engineering (Mechanical Engineering)

Keywords: Labyrinth seal, Brush seal, Leakage rate, Shaft rotation, Leakage flow fields

This project was initiated by ESKOM power generation. ESKOM loses up to 22% of their steam energy in the HP turbines due to leakage at the turbine labyrinth seals. Therefore the need was expressed their need to implement improved sealing configurations. The aim of this study is to investigate the effect that shaft rotation has on the leakage rate of labyrinth and brush seals. This is done by means of experimental and numerical methods.

For many decades it was assumed that the shaft rotation has no or little effect on seal performance and therefore it was neglected in seal design. It was decided to investigate this subject, in order to assist and improve in future seal design and operation.

Both labyrinth and brush seals were investigated experimentally on a test rig. A real life application of the labyrinth or brush seals can be found in the power generation industry where a turbine shaft has a diameter of 300 mm and rotates at 3 000 rpm. The test rig was designed to assist in this application. Therefor the test rig had a shaft diameter of 150 mm with shaft speeds ranging between 0-10 000 rpm and with five different upstream pressures ranging from 1-5 bar. The same seals were then simulated using the commercial Computational Fluid Dynamics (CFD) package STAR-CCM+ with the bristle pack of the brush seal modelled as a porous medium. The coefficients of resistance for the porous medium were experimentally obtained. The two investigation methods are compared for the labyrinth and brush seals. The labyrinth and brush seals are also compared against each other.

The results show that the experimental leakage rates have a good correlation with those predicted by CFD. The CFD simulation provided detailed leakage flow fields and pressure distributions of both seals. It was found that shaft rotation has an influence on the leakage

rate of both seals. The leakage rate increased at higher shaft speeds, with the brush seal performing better than the labyrinth seal. An increase of up to 1.7% was found at 10 000 rpm for the labyrinth seal and 1.45% for the brush seal at 10 000 rpm.

Guidelines were created based on these results to assist with advanced seal design. It is recommended that these guidelines are used in future seal design and other research aspects of non-contacting seals in turbo machinery.

Acknowledgements

The success and final outcome of this dissertation could not be done without the assistance, funding and guidance from many people. I am very honoured and privileged for having them throughout the entire completion of this dissertation.

- Special thanks to Prof JA Wiid, for supporting and motivating me when times get tough. “Dankie”...
- Special thanks to Prof KJ Craig, for guidance and patience to allow me to grow in the research environment.
- Special thanks to Dr “Coenie” Thairt, for his insight and extensive knowledge in gas dynamics and granting me this opportunity to learn from the best.

Table of Contents

Abstract.....	i
Acknowledgements.....	iii
List of figures.....	vii
List of tables.....	ix
List of symbols.....	x
List of abbreviations.....	xii
Chapter 1 – Introduction.....	1
1.1. Background and motivation.....	1
1.2. Problem statement.....	2
1.2.1. Research Objectives.....	2
1.3. Layout of Dissertation.....	3
Chapter 2 – Literature review.....	4
2.1 Introduction.....	4
2.2. Types of seals.....	6
2.2.1. Labyrinth seals.....	6
2.2.2. Brush seals.....	7
2.2.3. Hybrid seal.....	7
2.2.4. Leaf seal.....	8
2.3. Research into Labyrinth seal performance.....	9
2.3.1. History of Labyrinth seal.....	9
2.3.2. Recent work on Labyrinth seals.....	9
2.4. Brush seal Research.....	11
2.4.1. History of Brush seal.....	11
2.4.2. Recent work on Brush seals.....	11
2.5. Summary.....	13
Chapter 3 – Experimental Method.....	14
3.1. Setups.....	14
3.1.1. Experimental setup components.....	16
3.1.2. Uncertainty in Experimental Data.....	16
3.2. Orifice design.....	17
3.3. Experimental Procedure.....	18
3.3.1. Calibration setup.....	18
3.3.2. Experimental setup.....	19
3.4. Summary.....	20

Chapter 4 – Numerical Method	21
4.1. Introduction	21
4.2. Geometry	21
4.2.1. Labyrinth Seal Geometry	21
4.2.2. Brush Seal Geometry	23
4.3. Boundary Conditions.....	24
4.4. Mesh	25
4.4.1. Mesh with refinements.....	25
4.4.2. Mesh independence	26
4.5. Material properties and solver settings.....	28
4.6. Porous Medium.....	29
4.7. Summary	31
Chapter 5 – Experimental and Numerical Results of Calibration setup	32
5.1. Introduction	32
5.2 Calibration exercise.....	32
5.2.1. Experimental Setup.....	33
5.2.2. Numerical setup.....	33
5.3. Results.....	34
5.4 Conclusion.....	42
Chapter 6 – Labyrinth and Brush seals Performance Analysis.....	43
6.1. Introduction	43
6.2. Labyrinth and Brush seal results	43
6.2.1. Error Analysis	48
6.2.2. Detailed CFD results.....	49
6.2.3. Velocity triangles.....	58
6.5. Seal Design guidelines.....	61
6.6. Summary	61
Chapter 7 – Conclusion and Recommendations.....	62
7.1. Introduction	62
7.2. Summary	62
7.3. Conclusion.....	64
7.4. Recommendations	65
References	66
Appendices.....	70
Appendix A – Orifice Design.....	71

Appendix B – Matlab codes for Test setups calculation	80
Appendix C – Calibration Certificate	83
Appendix D – Uncertainty in Experimental Data	92
D.1. Uncertainty method	92
D.2. Experimental Setup	93
D.3. Coefficient of Resistance setup	96
Appendix E – Coefficients of Resistance	97
E.1. Introduction	97
E.2. Coefficients of Resistance	97
E.3. Test Setup	98
E.4. Procedure.....	98
E.5. Experimental Uncertainty	99
E.6. Results.....	99
Appendix F – Labyrinth seal leakage area.....	102
Appendix G – Mesh independence study	103
Mesh independence of Calibration setup simulations	104
Numerical method Mesh independence	105
Appendix H – Labyrinth Seal Results.....	106
Appendix I – Brush seal Results	108
Appendix J – Calibration Exercise Results.....	110
Appendix K - Sample Conversions.....	112

List of figures

Figure 2.1 Locations where Labyrinth seals are typically used in gas turbine engines (Hiester, 2013)	4
Figure 2.2 Typical brush seal locations in industrial stream turbines (Cofer et al. 1996) – arrows indicating seal locations	5
Figure 2.3 View of downstream (left) and inside view of teeth (right) of a three-tooth labyrinth seal (Ashton, 2009).....	6
Figure 2.4 Schematic showing the honeycomb labyrinth seal with honeycomb cells (Rohan et al. 2002)	6
Figure 2.5 Axial and cross-sectional views of conventional brush seal (Chupp et al. 1991)	7
Figure 2.6 Upstream (a) and Downstream (b) view of a hybrid seal with brushes on the upstream and the cantilever pads on the downstream side. (c) Schematic side view (Ashton, 2009).....	8
Figure 2.7 Section of a leaf seal pack (Rohan et al. 2002)	8
Figure 3.1 Schematic of Calibration experimental setup 1 with nozzle plate	14
Figure 3.2 Schematic of Experimental setup 2 used to simulate the effect of shaft rotation.....	15
Figure 3.3 ASME Orifice, with diameter 19.4mm used in experimental setup	17
Figure 3.4 Nozzle plate attached to downstream flange on the experimental setup 1	18
Figure 4.1 Labyrinth seal geometry, units in [mm]	22
Figure 4.2 Location of the brush porous medium, units in [mm]	23
Figure 4.3 Boundary conditions of the Labyrinth quarter model.....	25
Figure 4.4 Refined 2D mesh of the labyrinth seal	25
Figure 4.5. Refined 3D mesh of the labyrinth seal	26
Figure 4.6 Graph of Mass flow rate vs number mesh cells	27
Figure 4.7 Resistance curve for the brush seal bristles	29
Figure 4.8 Result of Validation simulation of the porous medium	30
Figure 5.1 Nozzle plate with 1mm-diameter nozzle	33
Figure 5.2 CFD Calibration exercise mesh for 8mm nozzle section on half model (approximate 2 million cells)..	34
Figure 5.3 Front view of Mesh inlet boundary condition	34
Figure 5.4 Calibration exercise: Mass flow rate for 1mm-diameter nozzle versus upstream pressure	35
Figure 5.5 Calibration exercise, Mass flow rate for 8mm-diameter nozzle versus upstream pressure	36
Figure 5.6 Calibration exercise, Mass flow rate for 12mm diameter nozzle versus upstream pressure	37
Figure 5.7 Trendline gradients for various Nozzle diameters	39
Figure 5.8 Calibration exercise, CFD of 1mm, 8mm and 12mm nozzle at 4 bar upstream	40
Figure 5.9 Calibration exercise CFD temperature change in system.....	41
Figure 5.10 Calibration exercise CFD Mach number contours	42

<i>Figure 6.1 Labyrinth and Brush seal leakage rate for 0 and 10 000 rpm shaft speed at different upstream pressures.....</i>	<i>44</i>
<i>Figure 6.2 Mass flow vs Pressure gradient</i>	<i>45</i>
<i>Figure 6.3 Trendline gradients for Labyrinth and Brush seals with various shaft speeds</i>	<i>47</i>
<i>Figure 6.4 Average percentage difference between the Experimental and CFD for all shaft speeds</i>	<i>48</i>
<i>Figure 6.5 Labyrinth seal CFD Pressure distribution with enlarged section</i>	<i>49</i>
<i>Figure 6.6 Brush seal CFD Pressure distribution with enlarged section</i>	<i>50</i>
<i>Figure 6.7 Labyrinth seal enlarged section with Mach numbers</i>	<i>50</i>
<i>Figure 6.8 Brush seal enlarged section with Mach numbers</i>	<i>51</i>
<i>Figure 6.9 Seal comparison with flow behaviour on the shaft – side view and top view of section midway through gap</i>	<i>52</i>
<i>Figure 6.10 Labyrinth seal side view of velocity vectors</i>	<i>53</i>
<i>Figure 6.11. Labyrinth seal plane comparisons</i>	<i>53</i>
<i>Figure 6.12. Brush seal side view of velocity vectors</i>	<i>54</i>
<i>Figure 6.13. Brush seal plane comparisons.....</i>	<i>54</i>
<i>Figure 6.14. Velocity components for the Labyrinth seal on the mid-plane</i>	<i>55</i>
<i>Figure 6.15. Velocity components for the Brush seal on the mid-plane</i>	<i>56</i>
<i>Figure 6.16. Vorticity of the Labyrinth seal on the mid-plane.....</i>	<i>56</i>
<i>Figure 6.17. Vorticity of the Brush seal on the mid-plane.....</i>	<i>57</i>
<i>Figure 6.18 Schematic of the Velocity triangle on the shaft</i>	<i>58</i>
<i>Figure 6.19 Schematic of flow velocity components.....</i>	<i>59</i>
<i>Figure 6.20 Velocity triangles of the labyrinth and brush seal</i>	<i>60</i>
<i>Figure C.1 Pressure gauge – SA Gauge DPG – 502 Calibration Certificate</i>	<i>83</i>
<i>Figure C.2 Pressure gauge – SA Gauge DPG – 502 Data Sheet.....</i>	<i>84</i>
<i>Figure C.3 Temperature gauge – Ero Electronic Monocal 2000 Calibration Certificate</i>	<i>85</i>
<i>Figure C.4 Temperature gauge calibration data page 2.....</i>	<i>86</i>
<i>Figure C.5 Temperature gauge calibration data page 3.....</i>	<i>87</i>
<i>Figure C.6 Temperature gauge calibration data page 4.....</i>	<i>88</i>
<i>Figure C.7 Temperature gauge calibration data page 5.....</i>	<i>89</i>
<i>Figure C.8 Temperature gauge calibration data page 6.....</i>	<i>90</i>
<i>Figure C.9 Temperature gauge calibration data page 7.....</i>	<i>91</i>
<i>Figure D. 1 Uncertainty vs Number of Iterations</i>	<i>95</i>
<i>Figure G.1 Calibration exercise mesh independence result</i>	<i>104</i>
<i>Figure G.2 Numerical method mesh independence result</i>	<i>105</i>
<i>Figure K.1 Graph of residuals after 10 000 iterations.....</i>	<i>112</i>

List of tables

<i>Table 3.1 Components of Experimental setups</i>	16
<i>Table 3.2 Test Matrix of mass flow rates for upstream pressure vs shaft speed</i>	19
<i>Table 4.1 Mesh independence study results</i>	27
<i>Table 5.1 Data of calibration exercise for 1mm-diameter nozzle</i>	35
<i>Table 5.2 Data of calibration exercise for 8mm-diameter nozzle</i>	36
<i>Table 5.3 Data of calibration exercise for 12mm-diameter nozzle</i>	37
<i>Table 5.4 CFD trendline gradients for various nozzle-diameters</i>	38
<i>Table 6.1 Labyrinth seal stationary shaft and 10 000 rpm shaft speed: Leakage rates for different upstream pressures</i>	43
<i>Table 6.2 Brush seal stationary shaft and 10 000 rpm shaft speed: Leakage rates for different upstream pressures</i>	44
<i>Table 6.3 Labyrinth seal Trendlines gradients</i>	46
<i>Table 6.4 Brush seal Trendlines gradients</i>	46
<i>Table 6.5 Average percentage difference of leakage rate between Experimental and CFD</i>	48
<i>Table 6.6 Labyrinth seal leakage flow velocity components</i>	59
<i>Table 6.7 Brush seal leakage flow velocity triangle components</i>	59
<i>Table G.1 Calibration exercise Mesh independence data</i>	104
<i>Table G.2 Numerical method Mesh independence data</i>	105
<i>Table H.1 Labyrinth seal Experimental Results – Mass flow rate</i>	106
<i>Table H.2 Labyrinth Numerical Results – Mass flow rate</i>	106
<i>Table H.3 Labyrinth seal Percentage difference between Experimental and Numerical methods</i>	107
<i>Table H. 4 Labyrinth CFD Velocity components</i>	107
<i>Table I.1 Brush seal Experimental Results – Mass flow rate</i>	108
<i>Table I.2 Brush seal Numerical Results – Mass flow rate</i>	108
<i>Table I.3 Brush seal Percentage difference between Experimental and Numerical methods</i>	109
<i>Table I.4 Brush seal CFD - Velocity components</i>	109
<i>Table J.1 Experimental Results – Mass flow rate</i>	110
<i>Table J.2 Numerical Results – Mass flow rate</i>	110
<i>Table J.3 Percentage difference between Experimental and Numerical methods</i>	111
<i>Table J.4 Upstream Velocity of Numerical Method</i>	111

List of symbols

Symbol		Description	Unit
A	-	Area of pipe/hole	[m ²]
A _{seal}	-	Area of the gap between the seal and the shaft	[m ²]
c	-	Speed of Sound at a specific temperature	[m/s]
C _d	-	Discharge Coefficient of orifice	-
C _S	-	Sutherland constant	[]
d	-	Orifice hole diameter	[mm]
d _{nozzle}	-	Nozzle diameter	[mm]
D	-	Inside pipe diameter	[mm]
e	-	Orifice edge thickness	[mm]
E _{max}	-	Maximum Orifice plate thickness	[mm]
E _{min}	-	Minimum Orifice plate thickness	[mm]
f	-	Performance parameter	[unit]
F	-	Angle of bevel	[degrees]
F _S	-	Factor of safety	[]
G _i	-	Ideal specific gravity	-
k	-	Gradient	-
L	-	Length	[m]
l ₁	-	Upstream spacing length	[mm]
l ₂	-	Downstream spacing length	[mm]
\dot{m}	-	Leakage rate	[kg/s]
M	-	Mach number	-
M _{mass}	-	Molecular mass of the fluid	[kg/kmol]
P	-	Pressure	[Pa]
P ₀	-	Reference Pressure	[Pa]
Q _m	-	Mass flow rate	[kg/s]
r	-	Refinement ratio	[]
R	-	Gas constant	[J/kg.K]
R _u	-	Universal Gas constant	[J/kmol.K]
R _D	-	Reynolds number referring to pipe diameter	-
t	-	Stagnation temperature	[K]
T	-	Temperature	[K]
T ₀	-	Reference temperature	[K]
U	-	Uncertainty error	-
\dot{V}	-	Velocity	[m/s]
z	-	Order of convergence	[]
Z	-	Gas compressibility factor	-

Greek Symbol		Description	Unit
α	-	Inertial resistance coefficient	-
β	-	Diameter ratio	-
δ	-	Partial derivative	-
ΔP	-	Difference in Pressure	[Pa]
ϵ	-	Expansion factor of orifice	-
μ	-	Fluid viscosity	[Pa.s]
μ_0	-	Reference fluid viscosity	[Pa.s]
v	-	Fluid velocity	[m/s]
ρ	-	Fluid density	[kg/m ³]
ρ_0	-	Reference density	[kg/m ³]
τ	-	Viscous resistance coefficient	-
φ	-	Resistance curve constant	-
ϵ	-	Relative error	-
γ	-	Isentropic gas constant	-

List of abbreviations

Abbreviation		Meaning
2D	-	Two dimensional
3D	-	Three dimensional
AMG	-	Adaptive Multi Grid
ASME	-	American Society of Mechanical Engineers
BC	-	Boundary Conditions
CFD	-	Computational Fluid Dynamics
CO ₂	-	Carbon dioxide
EDM	-	Electrical Discharge Machine
Exp	-	Experiment
GCI	-	Grid Converge Index
GE	-	General Electric
HP	-	High Pressure
HBS	-	Hybrid Brush Seal
J	-	Joule
K	-	Kelvin
kg	-	Kilogram
kPa	-	Kilopascal
LP	-	Low Pressure
m	-	Meter
RANS	-	Reynolds-averaged Navier-Stokes
STAR	-	STAR CCM+
SWorks	-	Solid Works
VSD	-	Variable Speed Drive

Chapter 1 – Introduction

This chapter discusses the background of this study. The problem statement with its research objectives are stated. The layout of this dissertation is also shown.

1.1. Background and motivation

This project was initiated by ESKOM power generation. ESKOM loses up to 22% of their steam energy in the HP turbines due to leakage at the turbine labyrinth seals. Therefore it expressed their need to implement improved sealing configurations. In the modern era the world has also become aware of the carbon footprint left behind from the aeronautical-, industrial- and energy industries as well as the depletion of fossil fuel resources. This has led to research into the improvement of the efficiency of thermal power plants which would reduce CO₂ emissions and conserve energy resources. The aim of this study is to investigate the effect that shaft rotation has on the leakage rate of labyrinth and brush seals. This is done by means of experimental and numerical methods.

For many decades it was assumed the shaft rotation has no or little effect on seal performance and therefore it was neglected in seal design. It was decided to investigate this subject, in order to assist and improve in future seal design and operation.

Turbine machines are at the heart of a thermal power plant and also many other turbine applications, like the aircraft industry. For this reason it is critical for these machines to achieve and maintain an optimum efficiency. A slight increase in the turbine machine efficiency could greatly enhance the environmental impact of the process. Internal leakage flow within these machines is a major source of energy loss and should therefore be closely controlled and kept to a minimum. Traditionally labyrinth seals have been used within turbo machines to prevent and control some of these leakage flows.

Turbine machines are the heart of a thermal power plant and also the heart of an aeroplane, thus for this reason it is critical for these machines to achieve and maintain an optimum efficiency. A slight increase in the turbine machine efficiency could greatly enhance the environmental impact of the process. Internal leakage flow within these machines is a major source of energy loss and should therefore be closely controlled and kept to a minimum. Traditionally labyrinth seals have been used within turbo machines to prevent and control some of these leakage flows.

Brush- and leaf-types seals are a much newer technology used to prevent leakage. Brush seals have better wear performance and provide better sealing than labyrinth seals. The leaf seal is an alternative flexible seal that shares characteristics with brush seals, but will not be considered in this study.

The analysis of brush seals is complex because of the brush geometry. For this reason labyrinth seals are considered first to gain knowledge in the analysis methods. A comparison is then made between the sealing characteristics of labyrinth and brush-type seals.

There are many different types of these seals that have been developed for various configurations. Companies that manufacture these seals test and evaluate them for different parameters. The parameters include pressure ratios over the seal, gap clearances, rotational effects, etc. In general these companies don't make these results available to public. As a result the information on how these seals work and their behaviour relative to different parameters are scarce in the open literature.

The motivation for this study is to develop methods with which the performance behaviour of these type of seals can be determined and evaluated for various parameters. These methods should be able to analyse these seals in detail. This will help to better understand how these seals work, which will help with future seal design.

1.2. Problem statement

There is very limited information available about the behaviour of labyrinth and brush seals relative to different parameters in the open literature. This dissertation will develop methods which can be used to explore the effect of shaft rotation on the leakage rate. These methods can be used to expand open literature and be used in future work to improve and optimise seal designs.

1.2.1. Research Objectives

The main and sub-objectives are presented.

Main objective:

The aim of this work is to understand the effect of shaft rotation on fluid flow leakage through labyrinth and brush seals.

Sub-objectives:

1. Obtain background theory and literature survey.
2. Experimental objective – construct setup to test for various parameters.
3. Numerical objective – develop model, validate and use to understand and improve seal designs.
4. Compare and evaluate experimental and numerical results.
5. Compare performance of different seal types.

6. Make recommendations and provide guidelines for developing new seal designs with improved leakage performance.

1.3. Layout of Dissertation

Chapter 1 is the introduction. It gives a background, describes the problem and the objectives.

Chapter 2 presents the available literature on the types of non-contacting seals. The elements of labyrinth and brush seals and the work that had already been done in these fields, are discussed.

Chapter 3 describes the experimental method, set-up and design. The methods and procedures to obtain the leakage rate through the labyrinth and brush seals at various shaft speeds are discussed in detail.

Chapter 4 describes the numerical method that is developed, which states the software and hardware that were used. The method is presented in detail with the mesh independent study performed on the various cases. The 2D and quarter 3D models of the leakage rate through the seals are also laid out in detail.

Chapter 5 presents the calibration exercise, which highlights the comparison of the numerical model with the experimental data. This discussion acts as a preliminary result to the final simulations and tests of the next chapter.

Chapter 6 presents a discussion of results, where the results obtained by the experimental and numerical methods are discussed for both labyrinth and brush seal types.

Chapter 7 presents a conclusion and recommendations for future work and improvements. These are the topics of the final chapter, where the findings and trends found are detailed and summarised.

2.1 Introduction

This chapter discusses the research, research methodologies and techniques with their findings of labyrinth and brush seals. Turbine engines and power stations have been around for more than 100 years while turbo-jet planes have been around for more than 70 years. Both the aviation and energy sectors are heavily dependent on turbine machines. The basic principle behind turbine machines is to convert the high energy of a fluid into continuous power in the form of shaft rotation. The first law of thermodynamics state that there will be energy losses in the conversion proses between thermal energy and mechanical machines. It is important to minimize leakages of the high-energy fluid, since it would decrease the overall efficiency of the system. The high pressure steam pushes against the rotor-blades which translate to shaft rotation and power generation. Some of the high pressure stream slips over the rotor-blade tip and this is known as secondary loses. According to the paper of Cofer et al. (1996), the secondary flow losses of an HP turbine can contribute up to 22% of the total loss of the stage efficiency. Therefore it is important that well-designed seals are used in turbines to eliminate leakage and increase the stage as well as overall efficiencies of the system. Figure 2.1 shows the locations where labyrinth seals are typically used in gas turbine engines to illustrate how important the seal performance is to the efficient operation. Brush seals and labyrinth seals can be found in similar locations in steam turbines to separate high and low-pressure zones (see Figure 2.2).

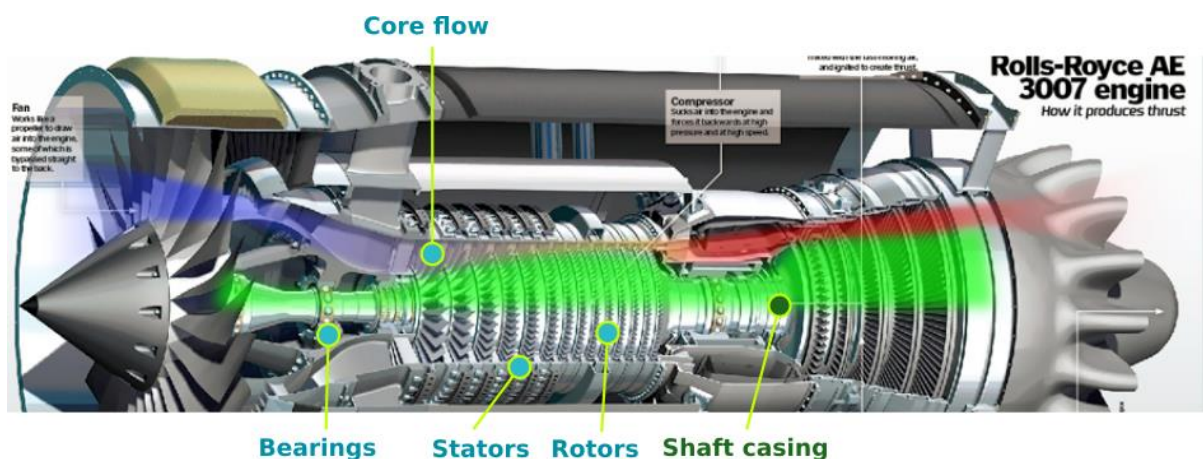


Figure 2.1 Locations where Labyrinth seals are typically used in gas turbine engines (Aviation.stackexchange, 2018)

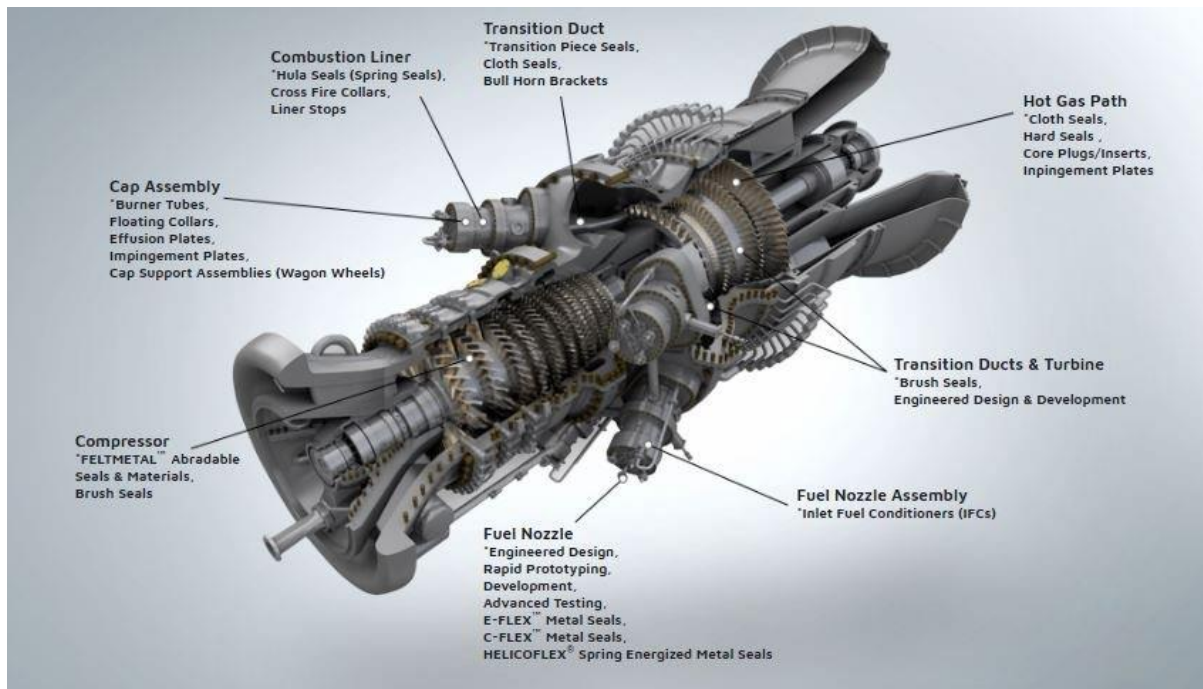


Figure 2.2 Typical brush seal locations in industrial stream turbines (Energy.Siemens.2018)

The traditional seals used to reduce leakage within the system are labyrinth seals. These seals are used because of their simple arrangement, low cost, and easy replacement (Chupp et al. 2006). Labyrinth seals do have limitations, mainly due to the gap clearance between the housing and rotor shaft. Labyrinth seals do make contact with the shaft from time to time. This causes the seal to wear, leading to increased seal gap. This friction also causes heat in the shaft leading to more complex dynamic problems. The reason for the shaft contact can be due to surges and imbalances in the system. Brush seals have larger leakage gaps to start with and this problem of the shaft contact gets minimized.

Brush seals have proven to be a great alternative and more effective than labyrinth seals. Apart from brush and labyrinth seals, other types in use include leaf and hybrid seals. Since the stricter carbon footprint laws and strive for cleaner energy, research has led to the drive to increase efficiencies. Brush seals have attracted a lot of research interest due to the previous reasons and their superior leakage performance compared to labyrinth seals.

This survey focuses on literature that is available through open academic access to databases like ScienceDirect and Scopus. Paid subscription industry-linked journal, and proprietary industry internal reports were not considered.

2.2. Types of seals

This section lists the different type of seals that are used with a description of how they work.

2.2.1. Labyrinth seals

A labyrinth seal is a non-contacting, high-pressure seal that seals the gap between a rotating shaft or rotor and the housing of the turbine. It is a type of mechanical seal that provides a tortuous path for the fluid to pass through, choking and restricting the flow to minimise leakage. These seals normally contain a straight blade with a tapered tip, but there are also curved blade types. Labyrinth seals also have cavities surrounding them which come in a variety of shapes. The flow field through the seal changes based on the cavity shape. The sealing effectiveness of a labyrinth seal is mainly dependent on the gap clearance between the seal tip and the opposing surface (see Figure 2.3).

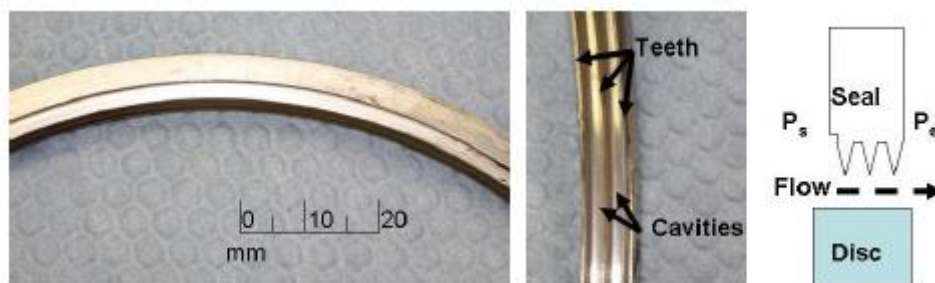


Figure 2.3 View of downstream (left) and inside view of teeth (right) of a three-tooth labyrinth seal (Ashton, 2009)

A variation of the labyrinth seal is the honeycomb labyrinth seal. Instead of the traditional array of labyrinth seals, the seals are connected to create cells which look like honeycomb. These cells create pressure differences and swirls within each cavity which makes the path of the flow even more tortuous. Figure 2.4 shows a schematic of a honeycomb labyrinth seal with the honeycomb cells.

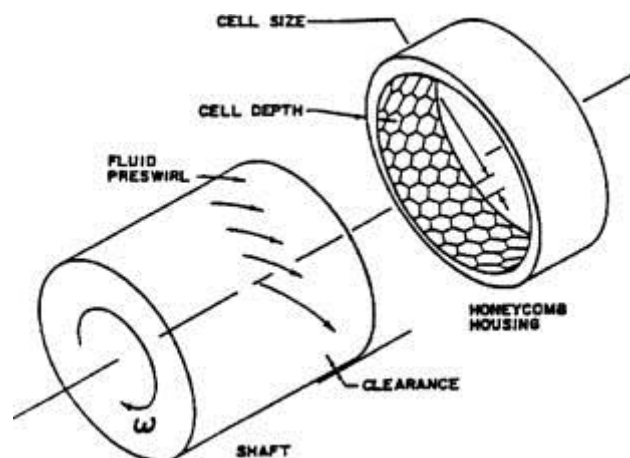


Figure 2.4 Schematic showing the honeycomb labyrinth seal with honeycomb cells (Rohan et al. 2002)

2.2.2. Brush seals

Brush seals are also known as labyrinth brush seals. Brush seals make use of a flexible bristle pack which is clamped between the front and the backing plate. The bristle pack makes contact with the opposing surface when installed, but during operation the bristles make only slight contact with the opposing surface due to the lift of the bristles because of the fluid dynamic pressure distribution. In principle, the leakage flow can only go through the seal via the exposed bristle region when the brush seal is in contact with the surface. Due to this principle brush seals can significantly reduce the leakage rate compared with other seals. The bristles are oriented at a typical lay angle between 30° to 60° to the radial line of the rotor or shaft, and tilted in the direction of shaft rotation. Figure 2.5 shows axial and cross-sectional views of a conventional brush seal.

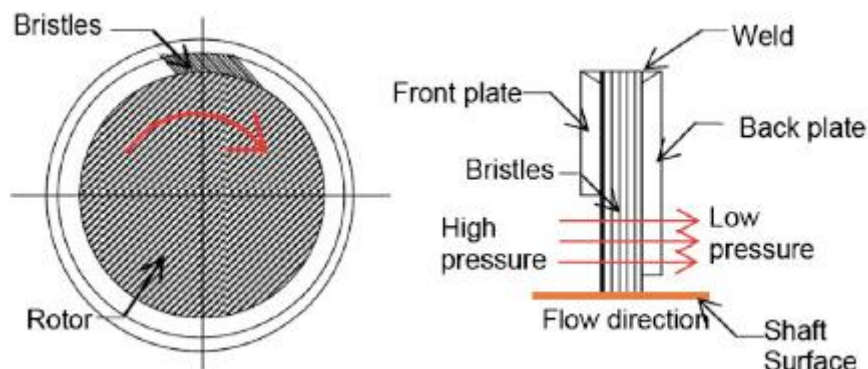


Figure 2.5 Axial and cross-sectional views of conventional brush seal (Chupp et al. 1991)

2.2.3. Hybrid seal

Hybrid seals are a much more recent development than brush and labyrinth seals. The aim of these hybrid seals is to reduce primary leakage and further limit the secondary leakage. Hybrid seals incorporate cantilevered pad elements in addition to the bristle pack of a brush seal. There are small spring elements that connect the bristle pack to the outer ring and the bristle tips barely make contact with the opposing surface. Figure 2.6 shows the seal with the bristle pack on the front side and the cantilevered pad elements on the back side.

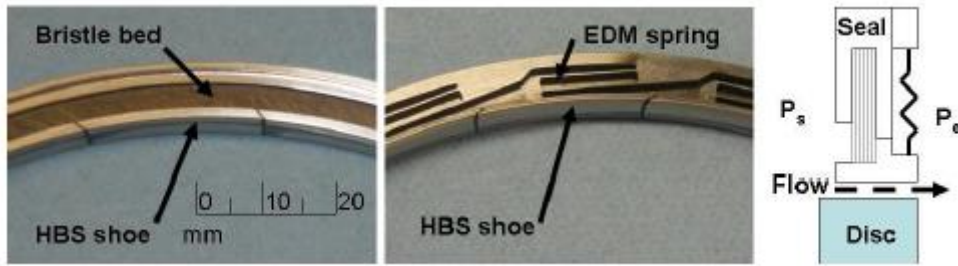


Figure 2.6 Upstream (a) and Downstream (b) view of a hybrid seal with brushes on the upstream and the cantilever pads on the downstream side. (c) Schematic side view (Ashton, 2009)

During operation, the cantilever pad elements create the formation of a hydrodynamic film. The low radial stiffness of the cantilever pad elements and bristle pack allows the pads to lift. The generation of a boundary layer allows for a relatively low level of leakage while preventing contact between the seal and shaft or rotor.

2.2.4. Leaf seal

Leaf seals are the latest technology developed. They work on the same principle as brush seals, but instead of a bristle pack there is a leaf pack. A leaf pack consist of thin flexible strips packed together to form a tortuous path for the fluid to pass through. Figure 2.7 shows a section of a leaf seal pack.

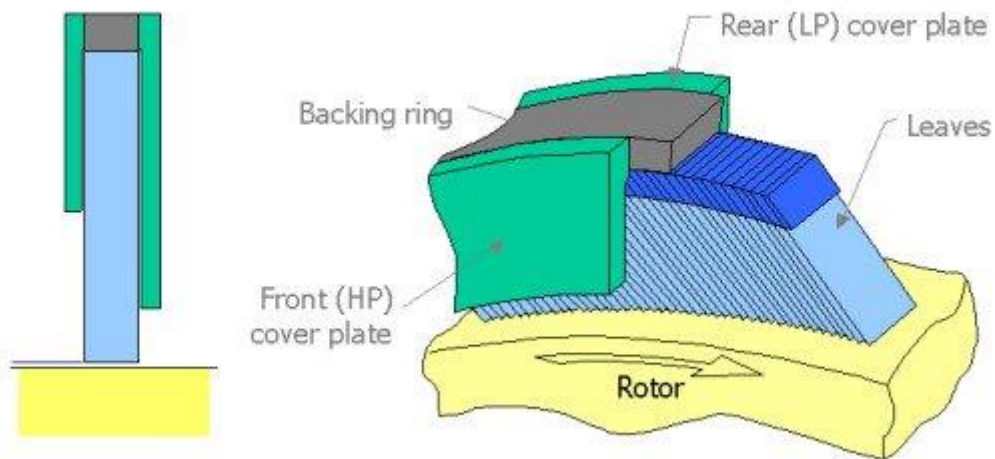


Figure 2.7 Section of a leaf seal pack (Rohan et al. 2002)

2.3. Research into Labyrinth seal performance

2.3.1. History of Labyrinth seal

The first commonly cited publication on the calculation of the leakage of labyrinth seals was by Martin (1908). His publication presented equations that could be used to estimate leakage through labyrinth seals. Martin's work was expanded upon by Egli (1935) with his widely referenced paper, "Leakage of Steam through Labyrinth Seals," (Egli, 1935) which is still used today to estimate labyrinth seal leakage.

Years later Vermes (1961) further expanded upon Martin's work by presenting leakage equations for straight, stepped and combination seals. At the time of the above referenced work, the impact of seal leakage on overall machine efficiency was considered trivial. It was not until the mid to late 1960s that the impact of labyrinth seal leakage on turbine and compressor efficiency started to become a concern. Also around this time, it became clear that labyrinth seals could influence the rotor dynamics behaviour of a turbomachine (Whalen and Alvarez, 2004).

After the 1960s, labyrinth seals were investigated in a lot of detail. The research done on labyrinth seal span several diverse fields ranging from leakage rate, gap clearances, seal array layout to seal tip geometry. The research has mainly been driven by the aviation sector and the power generation sector. The main differences between the seals used in the two sectors are the size of seals and the operating temperature.

2.3.2. Recent work on Labyrinth seals

Recent research has been performed both experimentally and numerically. Most of the research concentrated on determining the impact of the geometrical parameters on the leakage and pressure distribution (Massini et al. 2014).

In the experimental research surveyed, most researchers focused on stationary configurations, where the shaft or rotor rotation was neglected or ignored. The general assumption made by most researchers are that shaft rotation has a negligible effect on the leakage rate. In experimental work of Schramm et al. (2002) and Li et al. (2010) they show that such a simplification may be assumed if the flow velocity over the labyrinth seal tip is much higher than the tangential velocity of the shaft or rotor. In these cases the stationary test rigs simulate the flow behaviour correctly. In other cases where the flow velocity over the labyrinth seal tip is lower than or equal to the tangential velocity of the shaft or rotor, the shaft rotation effect becomes a major factor with substantial differences between the stationary model and rotating models.

Researchers often compare the behaviour of labyrinth seals test rigs that make use of rotation to those without rotation by focusing on static pressure uniformity in the circumferential direction. They concluded that the mass flow rate through the seal depends not only on the static upstream pressure, but also on many other parameters, such as the upstream temperature, Reynolds number, angle of inflow onto the seal (initial pre-swirl), pressure ratio, seal relative motion, the architecture of the seal itself and the clearance gap between the seal tip and shaft. In experiments carried out on stationary test rigs (Biester et al. 2011), the observed parameters are dimensionless mass flow rate and the pressure and temperature distribution along the seal structure.

In recent years, computational fluid dynamics (CFD) has become the choice of many researchers to investigate various seals numerically. With CFD complex geometries and innovative design can be investigated in detail with sophisticated numerical models.

Until recently researchers were limited by the computational power that was available, but great advances have been made in computational power. In that period many researchers, like Takenaga et al. (1998) and Denecke et al. (2005) were concerned with the labyrinth discharge coefficients and if they were accurately represented in CFD. The work in CFD was also limited to simplified cases where important features or flow conditions were not simulated. An example of this is Vakili et al. (2005) where they presented a CFD computation on a simplified 2D fine mesh on a labyrinth configuration without the complex geometry structure, and Choi and Rode (2003) used circumferential grooves to represent their honeycomb cells in a 3D model.

Lately Yan et al. (2009) investigated leakage, total temperature, and flow characteristics of laboratory seals using 3D CFD. They calibrated a 3D periodic CFD model of a stepped labyrinth seal to the experimental results from Denecke et al. (2005) and also compared CFD swirl velocity distribution results to Denecke's data, reporting an improved match relative to Denecke's 2D axisymmetric CFD simulation. Also in subsequent research Yan et al. (2010) showed how swirl velocities upstream of the lab seal affect seal characteristics. Yan et al. (2010) also studied the effects of honeycomb cell size on seal characteristics.

Li et al. (2007) presented an approach to include different effects of honeycomb cells. The effects of the pressure ratios and the seal clearance on the leakage flow were also investigated. It was concluded that the effect of the pressure ratio on the leakage flow behaviour could not be omitted and that a similar leakage flow was obtained for cases with rotating and non-rotating walls. A complete geometrical representation of a labyrinth seal was considered by Soemarwoto et al. (2007). After simulations of the leakage flow through three selected configurations, the main features of the flow were identified. Fine meshes were used which took into account the structure and sufficiently captured the important flow features with high gradients around the tip-edge with swirl regions. For the simulations a 2D mesh with 20000 cells and a 3D mesh with over 10 million cells were used.

2.4. Brush seal Research

2.4.1. History of Brush seal

Around about the early 1940s the first brush seals were tested in an attempt to reduce the leakage through the seal section and increase the efficiency of the overall system. The aviation sector was the drive behind the advancement of turbine technologies and also in brush seal technologies.

In the aviation sector the first attempt at replacing labyrinth seals with brush seals was done in 1955 in the General Electric (GE) J-47 engine (Cieślewicz, 2004). This turbojet engine was developed by GE from the earlier J35 engine and was first flight-tested in May 1948. It replaced J35 engines in the North American XF-86 "Sabre" (Cieślewicz, 2004). Unfortunately, the application of brush seals at that time turned out to be unsuccessful. Rolls Royce managed to apply brush seals in the early 1980s in demonstration engines. Afterwards, in 1987 the RB-199 engine was produced with installed brush seals (Cieślewicz, 2004). The IAE V2500 is an engine certified in 1987 (Cieślewicz, 2004). It was, for several years, the only production engine with brush seals. Allison has conducted many tests with usage of brush seals (Cieślewicz, 2004). Allison has come up with conclusions that brush seals reduced leakage flow up to an order of magnitude over labyrinth seals, and are tolerant to transient clearance changes.

It was only after the success of the aviation sector that brush seals were used in power stations. The brush seal has become a serious competitor for the replacement of its predecessor, the labyrinth seal. Brush seals allow axial or radial excursions of the spool shafts without suffering damage or affecting the sealing integrity. Ferguson (1988) reported that over thousands of hours of testing, brush seal leakage rates were, on the average, 5 - 10% of those experienced by equivalently-sized labyrinth seals. In 1991, Chupp et al. (2006) demonstrated brush seal leakage reductions of 4.5 times that of labyrinth seals.

2.4.2. Recent work on Brush seals

In the last two decades brush seals have become a promising alternative to conventional labyrinth seals because of their superior leakage performance (Ferguson, 1988). A lot of research has been done experimentally and numerically on the leakage flow and mechanical characteristics of brush seals in order to improve their efficiency.

Experimentally Bayley and Long (1993) measured the leakage of an interference brush seal by using a non-rotating experimental test rig. The work they have done was about the axial and radial pressure distribution under the bristle tips and that along the backing plate of the brush seal. Carlile et al. (1993) measured the leakage flow of the brush seals using different fluids, which were helium, carbon dioxide and gaseous air. The test was for sealing interferences at static and low rotor speed. Their findings were that the rotating condition for

the air and carbon dioxide leakage of the brush seals showed a slight decrease compared to the static test. Turner et al. (1998) measured the radial pressure distributions along the backing plate, the axial pressure distributions along the rotor and the leakage of the clearance brush seal at different pressure ratios. There was also an attempt to investigate the mechanics of clearance brush seals using a bending calculation. Chen et al. (2000) investigated experimentally the flow fields and pressure distributions of a large-scale brush seal. The observation made in these tests was that the bristle pack was compacted under pressure load and bent in the axial direction several times the bristle diameter.

Braun and Kudriavstev (1995) and Kudriavstev and Braun (1996) simulated the flow through staggered cylinders and compared the results with experimental results to investigate the flow field of brush seals. They solved the two-dimensional (2D) Navier-Stokes equations using the finite-difference method.

Commonly the bristle pack is treated as a porous medium with a defined resistance of flow to simulate the leakage flow of brush seals. This was first introduced by Bayley and Long (1993), where they used the Darcian porous medium model to predict the leakage flow in their experimental interference brush seal. The model used only considered the viscous flow resistance of the bristle pack. Chew et al. (1995) and Chew and Hogg (1997) introduced a non-Darcian porous medium approach to simulate the leakage flow in the brush seals. The viscous and inertial flow resistances were considered for the bristle pack in the model. Chen et al. (1999) developed an iterative CFD and mechanical brush seal model to predict the pressure capabilities, mass flows and bristle displacements of interference and clearance brush seals.

Dogu (2005) did a detailed numerical investigation of the leakage flow behaviour of the experimental interference brush seal (Bayley and Long, 1993) using a modified bulk porous medium approach. Dogu and Aksit (2006a, 2006b) later employed a similar modified bulk porous medium approach to investigate the effects of the front and backing plate configurations on the flow fields of brush seals. Dogu et al. (2008) then established a CFD model of brush seals using the bulk porous medium approach to predict the flow fields and pressure distributions of the brush seals (Turner et al. 1998) under partial blow-down and no blow-down operation modes.

Pugachev and Helm (2009) presented a calibration method of the porous medium model for brush seals by varying the bristle pack thickness to match the experimental data. Li et al. (2009) used the Reynolds-averaged Navier-Stokes (RANS) equations and non-Darcian porous medium model to investigate the effect of clearance sizes on the leakage flow characteristics of the labyrinth brush seal for turbomachinery.

2.5. Summary

In recent times experimental and numerical investigations were undertaken to analyse the effects of rotational speeds and pressure ratios on the leakage performance of labyrinth and brush seals for turbine applications. Different methods were used to evaluate the leakage in these seals. The leakage rate through the labyrinth and brush seals was measured using a rotating test rig. The leakage rate was also predicted using the Reynolds-averaged Navier-Stokes (RANS) solutions for the brush seal. The resistance coefficients of the porous bristle pack were estimated and calibrated with experimental leakage. The general conclusion was that shaft rotation had little effect on the leakage flow through these seals.

The current study will focus on the effect that shaft rotation has on the leakage performance of both labyrinth and brush seals. Both experimental and numerical methods will be used to investigate these phenomena as were done by previous researchers. Different pressure ratios will be considered as by Li et al. (2012) at various shaft speeds.

Chapter 3 – Experimental Method

The experimental method is discussed in this chapter. An overview is given of the experimental setup design, experimental procedure and uncertainty in experimental data measurement.

3.1. Setups

There are two main setups that are used during this dissertation. Both setups make use of an orifice system, which is discussed in section 3.2. An orifice design is performed, to measure the leakage rate through the seals and nozzles. The first setup, named the Calibration setup, shown in Figure 3.1, focuses on the measurement system and is used to gain confidence in the measuring system. The Calibration setup uses a plate with a nozzle, varying in sizes, to test the accuracy of the measuring system. The second setup, named Experimental setup, shown in Figure 3.2, is used to simulate the effect of shaft rotation on the leakage rate through both the labyrinth and brush seal configurations. The geometric dimensions of the labyrinth and brush seals used in the experimental setup are illustrated in detail in Chapter 4 in Figure 4.1 and 4.2.

The upstream section of both setups is the same. This part comprises on air inlet, control valve, two pressure gauges, a temperature gauge and an orifice. The working fluid used in the experimental setups is high-pressure air, which is supplied by a laboratory compressed-air line.

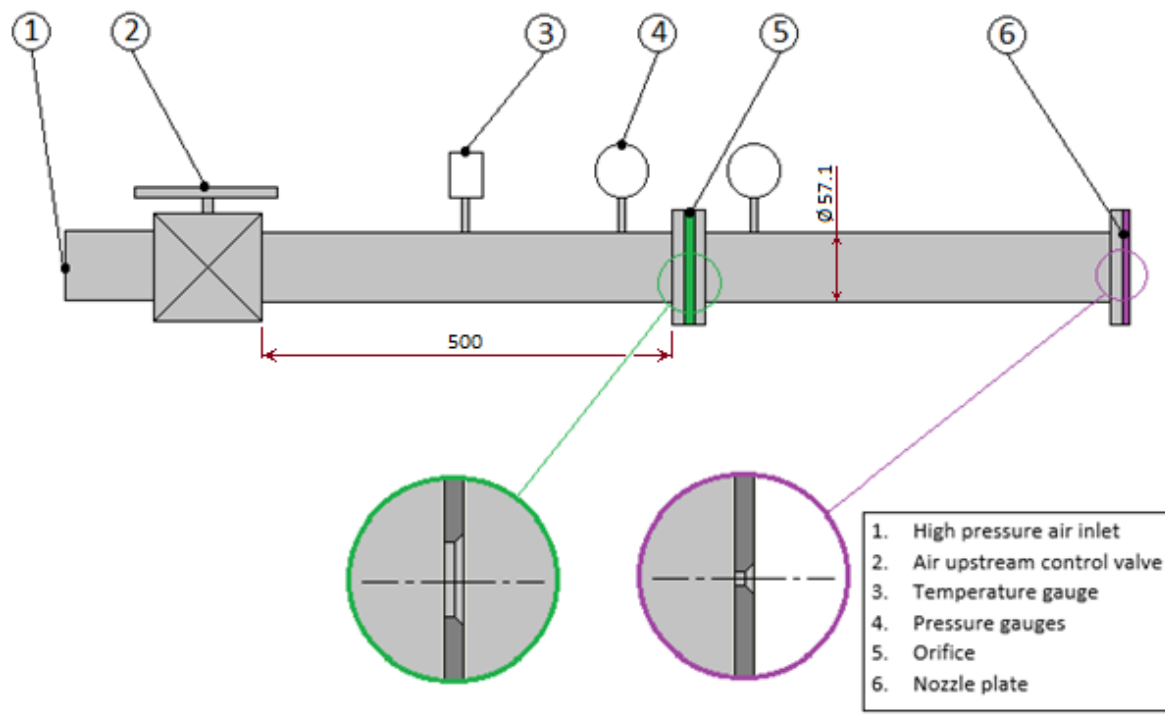


Figure 3.1 Schematic of Calibration experimental setup 1 with nozzle plate

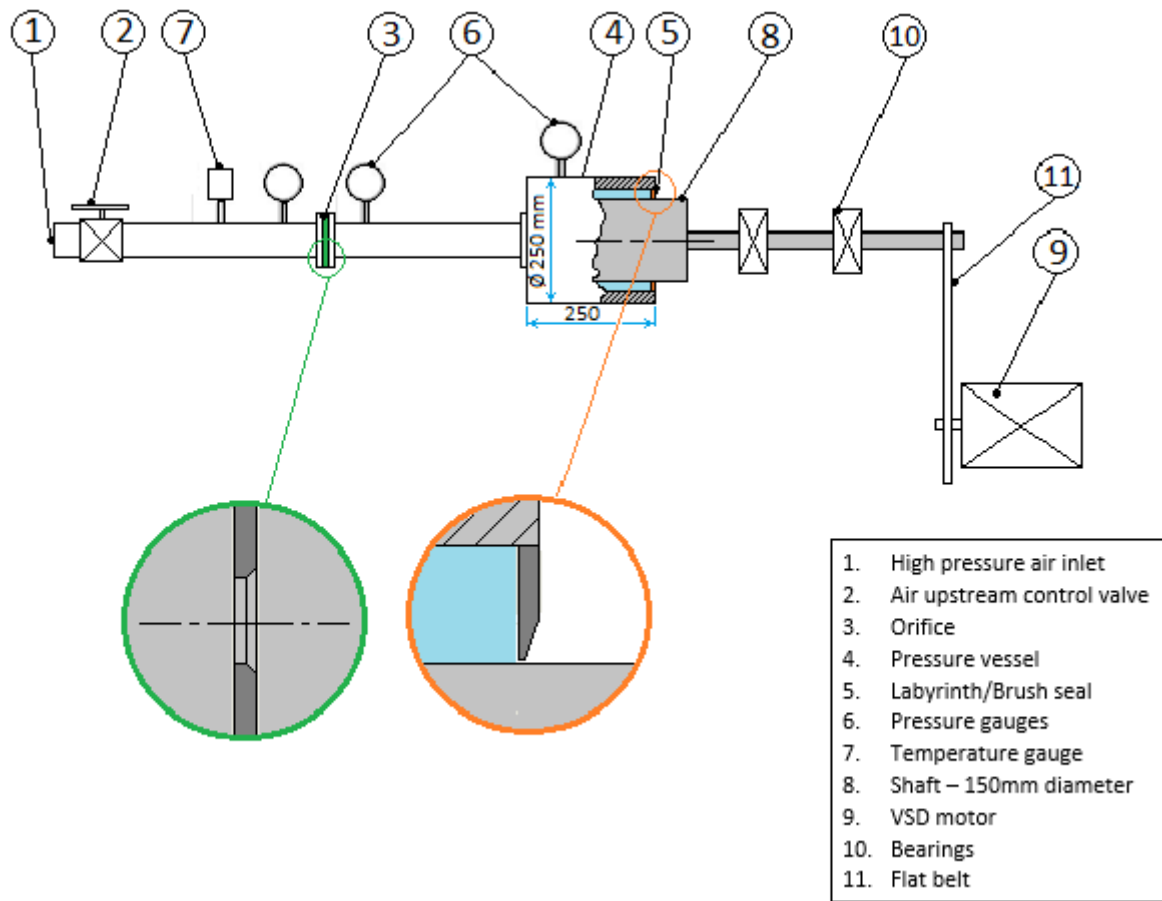


Figure 3.2 Schematic of Experimental setup 2 used to simulate the effect of shaft rotation

The key concept behind the experimental setup is to simulate the conditions which the non-contacting seals would experience when in operation. This would help one to determine the behaviour of the leakage flow through the seal experimentally. The pressurised air is used to simulate the high-pressure working fluid under which the seals operate. The rotating shaft simulates the surface movement relative to the seal or housing as well as the centrifugal forces on the working fluid. The seal geometry used is an exact replica of the seals found in industry. By controlling the upstream pressure with the control valve and controlling the shaft speed with the VSD motor, a vast variety of conditions can be simulated on the seals.

The shaft was milled to a smooth surface roughness of 0.05 mm/rev and then polished with superfine grit 5000 ($R_a = 2.5$ nm) sandpaper. The labyrinth seal is manufactured from aluminium with geometry as the seals found in industry. The brush seal is manufactured from aluminium and the bristles pack is constructed from stiff nylon wires with same diameter as the seals found industry.

The seals are bolted to the pressure vessel. There are 3 bolts which allow the seal position to be adjusted. This allows the seal to be concentric to the shaft. A feeler gauge is used to measure gap clearance between the seals and shaft to ensure it is concentric.

3.1.1. Experimental setup components

As mentioned there are several components that are used in both experimental setups. This section lists all the components that are used in the experimental setups with their descriptions and accuracy (see Table 3.1). The compressed air supply has a pressure range of 0 to 8 bar and is controlled by a valve.

Table 3.1 Components of Experimental setups

Component	Description	Range	Accuracy
Pressure gauge	SA Gauge Model DPG 502 (SA Gauge)	0 – 1000 kPa	± 0.25%
Temperature gauge	Ero Electronic Model Memocal 2000 (Eurotherm)	-50 – 400°C	± 0.5%
Orifice	ASME specification, Diameter 19.4 mm	0 – 0.75 kg/s	± 0.1%
VSD Motor	Brook Crompton 3kW DC motor, with U&S Power Electronic Drives system.	0 – 10 000 rpm	-
Aluminium Tube	Non-Ferrous metal works manufacturing	-	± 0.2%

The calibration certificates for each of the gauges are contained in **Appendix C**.

3.1.2. Uncertainty in Experimental Data

In experimentation there will always be some degree of uncertainty in the data. In this section the degree of uncertainty in the data collected by the experimental setup is calculated. As shown in section 3.1.1, each measuring instrument has a percentage error. These percentages are used to determine the overall uncertainty percentage using the method of GCI (ASME V&V, 2009).

The overall uncertainty of the mass flow rate equation is shown in equation 3.2. For the uncertainties of the other applicable equations and ratios refer to **Appendix D**.

Mass flow rate, \dot{q} :

$$\dot{q} = \frac{c_d}{\sqrt{1-\beta^4}} \left(\frac{\pi}{4} d^2 \right) e(\sqrt{2\rho\Delta P}) \quad [\text{eq 3.1}]$$

The error of uncertainty for mass flow rate, \dot{q}

$$U_q = \frac{\delta \dot{q}}{\dot{q}} = \left[\left(4 \frac{\delta \beta}{\beta} \right)^2 + \left(2 \frac{\delta d}{d} \right)^2 + \left(\frac{\delta e}{e} \right)^2 + \left(\frac{1}{2} \frac{\delta \Delta P}{\Delta P} \right)^2 + \left(\frac{1}{2} \frac{\delta \rho}{\rho} \right)^2 \right]^{\frac{1}{2}} \quad [\text{eq 3.2}]$$

$$U_q = 3.0 \%$$

The uncertainty for the final mass flow rate is $\pm 4.7\%$. Thus the error in the experimental data is 3% as the mass flow rate error is the largest (refer **Appendix D**).

3.2. Orifice design

For measuring the leakage rate or mass flow rate through the seals, an orifice system is used. The orifice system used in the setup makes use of an orifice, two pressure gauges and a temperature gauge to obtain data points. This system was designed with Section 7 in the ASME code (*Measurement of Fluid Flow in Pipes using Orifice, Nozzle and Venturi* 1990) to ensure the system is according to standard. The orifice size was calculated to be 19.4 mm in diameter (as calculated is in **Appendix A**). Figure 3.3 shows the orifice that is used in the experimental setup.

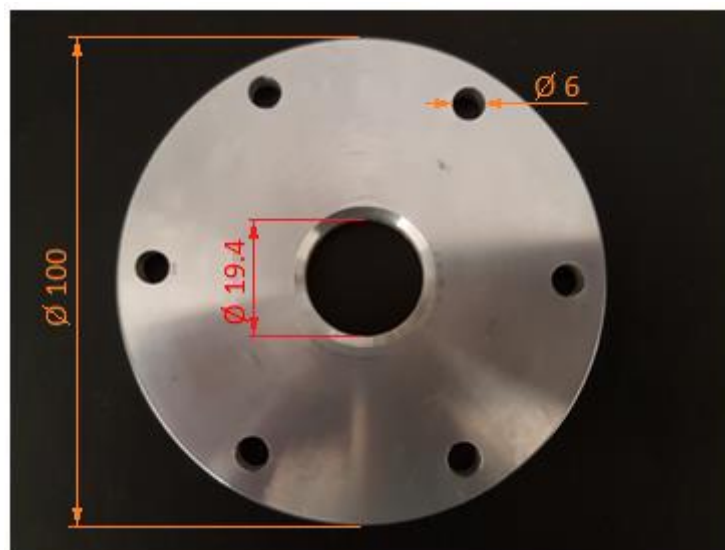


Figure 3.3 ASME Orifice, with diameter 19.4mm used in experimental setup

The data points collected were used to calculate the mass flow rate and the Reynolds numbers of the fluid passing through the orifice. A Matlab script was written to perform the calculations (see **Appendix B**).

3.3. Experimental Procedure

The experimental procedures used to collect data for both setups are given in this section.

3.3.1. Calibration setup

The nozzle plate is fitted to a flange on the downstream side of the orifice. Figure 3.4 shows the nozzle plate attached to the flange. The upstream pressure from the laboratory compressed air is applied to the nozzle plate. The upstream pressure is varied in the following sequence: 100 kPa, 200 kPa, 300 kPa, 400 kPa, 500 kPa, 600 kPa and 700 kPa. The upstream and downstream pressures of the orifice as well as the temperature of the air for each of the upstream pressures are recorded. The pressure and temperature readings are recorded directly from the gauge after 15 seconds of running when steady state is achieved. A table of mass flow rate vs upstream pressure is then compiled. This procedure repeated for the following nozzle diameters 1 mm to 12 mm in 1 mm increments. The matrix is repeated several times and the average will be used in analysis of the results.

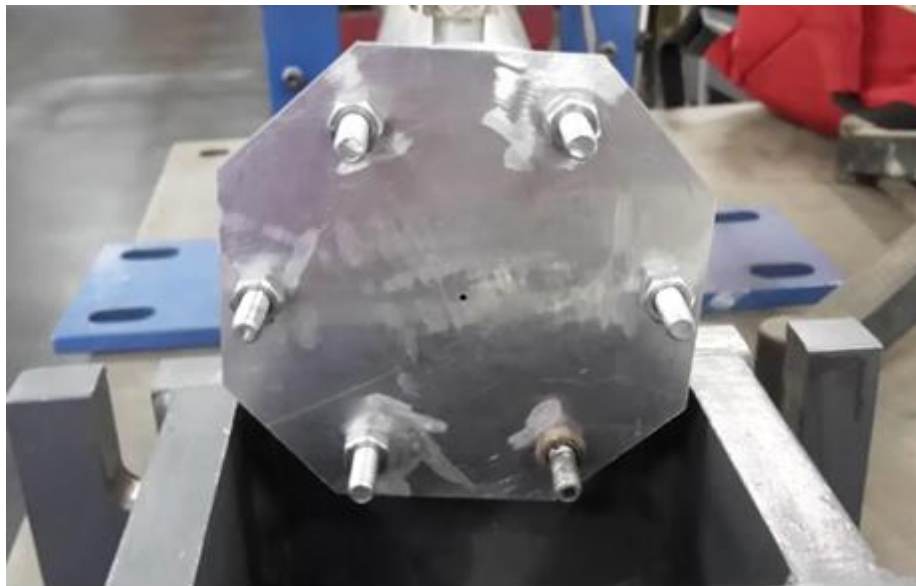


Figure 3.4 Nozzle plate attached to downstream flange on the experimental setup 1

3.3.2. Experimental setup

The seal is installed in the pressure-vessel section of the setup. The gap between the seal and shaft is measured with a feeler gauge, to ensure that the seal is concentric with in the shaft. The upstream pressure from the laboratory compressed air is applied to the seal. The upstream pressure is varied in the following sequence: 100 kPa, 200 kPa, 300 kPa, 400 kPa, 500 kPa and 600 kPa. After the upstream pressure sequence is completed, the upstream pressure is set back to zero. The shaft is then rotated with the VSD motor. The shaft speed is set, and the upstream pressure sequence is then repeated. The shaft speed is varied in the following sequence: 1000 rpm, 2000 rpm, 3000 rpm, 4000 rpm, 5000 rpm, 6000 rpm, 7000 rpm, 8000 rpm, 9000 rpm and 10 000 rpm. For each of the shaft speeds, the pressure sequence will be performed and the upstream and downstream pressures recorded together with the air temperature. The combination of upstream pressure sequence and shaft speed sequence fills the test matrix of mass flow rates for upstream pressure and shaft speed combinations (see Table 3.2). The above process is repeated for both the labyrinth and the brush seal.

Table 3.2 Test Matrix of mass flow rates for upstream pressure vs shaft speed

		Shaft speed [rpm]											
		0	1000	2000	3000	4000	5000	6000	7000	8000	9000	10 000	
Upstream Pressure [kPa]	100												
	200												
	300												
	400												
	500												
	600												
	600												

3.4. Summary

In this section the chapter is summarized.

- Two experimental setups are used in this dissertation (calibration and experimental setup) to collect the relevant data.
- The setup makes use of high pressurised air with a range of 0 to 7 bar upstream and a rotating shaft with a range of 0 to 10 000 rpm to simulate the various conditions.
- The leakage flow is measured with an orifice designed with the ASME (1990) code.
- The uncertainty in the experimental data was calculated to be 4.7%.
- The experimental procedure makes use of running the entire range of shafts speeds for each of the selected upstream pressures.

4.1. Introduction

The numerical method is discussed in this chapter. It gives an overview of the geometry, mesh, boundary conditions, solvers and the porous medium model used for the brush bristles. The numerical method is the simulation of the non-contact seals using computational fluid dynamics (CFD). STAR CCM+ 10.06 (STAR, 2014) is the program that is used in this dissertation for the CFD simulations and SolidWorks Premium 2014 (SWorks) is used to draw the geometries. The setup of the CFD models is divided into two sections, the labyrinth seal and the brush seal. The labyrinth seal will be simulated as a 3D quarter model. The brush seal will be simulated as a 3D quarter model with a porous medium.

4.2. Geometry

This section gives an overview of the geometries and the reasons why these geometries were selected for each of the sections.

4.2.1. Labyrinth Seal Geometry

The labyrinth seal is simulated in a 3D quarter model. A quarter model is used due to the axially symmetric nature of the geometry. This allows for better use of the available computational resources. The quarter can be simulated in much more detail than a full 3D model.

The labyrinth seal is simulated firstly as a 2D plane with the labyrinth seal geometry. The reason for using 2D simulation is that the 2D simulations are much cheaper than 3D in terms of computer resources and computational time. The 2D simulation is therefore used to find the critical focus points and allow the mesh to be refined accordingly. Figure 4.1 shows the full 3D domain of the labyrinth seal with the 3D quarter section and the 2D plane with the seal location.

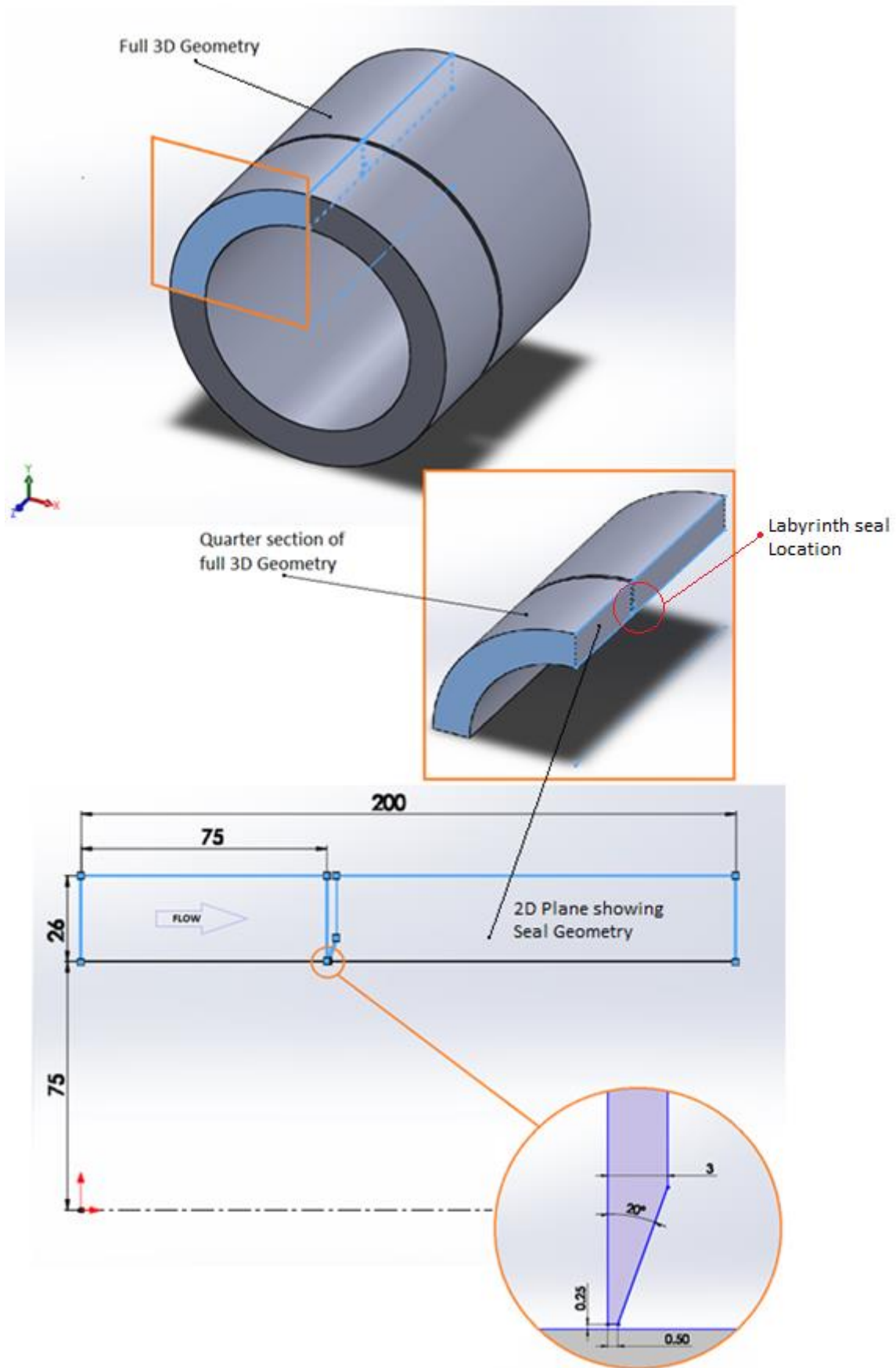


Figure 4.1 Labyrinth seal geometry, units in [mm]

4.2.2. Brush Seal Geometry

The brush seal is simulated as a 3D quarter model, due to the same reasons as for the labyrinth seal. The layout and dimensions are the same as the labyrinth seal's 3D geometry, except for the porous region. It was assumed that the bristle pack stay in contact with the shaft. In practice the bristles lift slightly due to the fluid dynamic pressure distribution. Since the amount of lift is unknown and limited computer resources were available, this phenomenon cannot be simulated accurately. A porous medium is used to simulate the brush bristles of the seal due to the complexity and number of entities required to accurately simulate brush bristles. Figure 4.2 shows the location of the porous medium in the geometry.

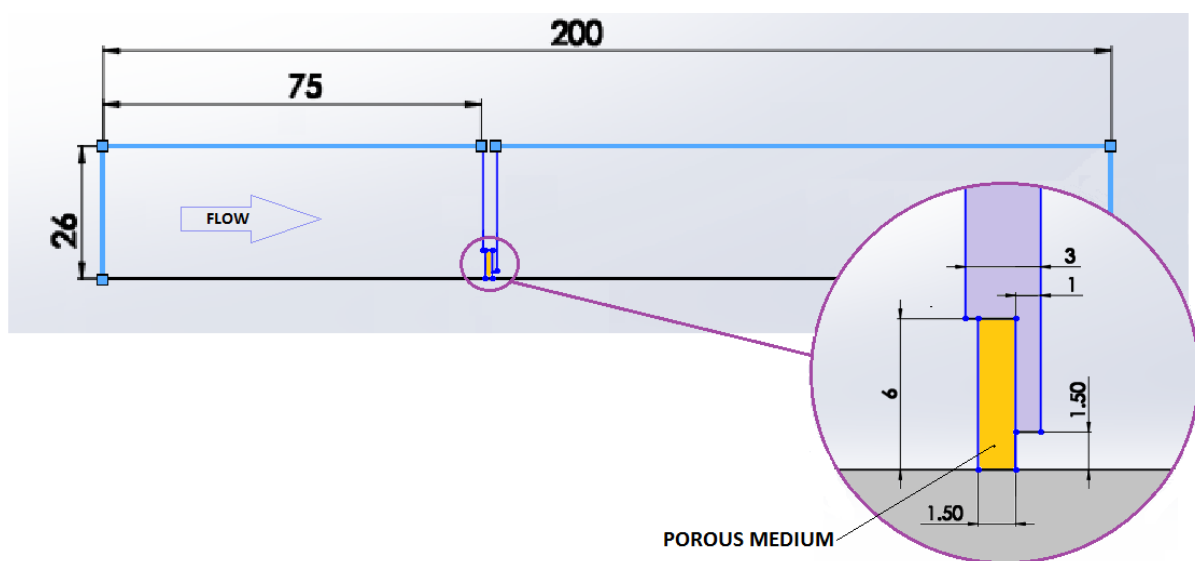


Figure 4.2 Location of the brush porous medium, units in [mm]

4.3. Boundary Conditions

The boundary conditions (BC) are what define the problem or investigation in CFD. Each of the surfaces of the geometry therefor needs to be defined. In STAR the boundary conditions are defined before the mesh is applied, because STAR takes into account the boundary type when generating the mesh.

The upstream inlet BC for all the cases is a stagnation inlet. The stagnation inlet sets a pressure at the inlet. Relative pressures are used at the inlet boundary condition, starting with a pressure of 100 kPa and is increased in increments of 100 kPa up to 600 kPa to simulate the same pressures upstream as the experimental procedure. The downstream outlet BC is a pressure outlet which is set to the laboratory reference pressure of 87 kPa. The laboratory pressure is 87 kPa due to the altitude of the location which is at approximate by 1300 m above sea level. The shaft BC is a wall with no-slip condition and has a rotational rate around the x-axis in the coordinate system. The shaft rotation starts at 0 rpm and is increased in increments of 1000 rpm up to 10 000 rpm to simulate the same shaft speeds used in the experimental procedure. The inlet, outlet and shaft BC are the same for the labyrinth 2D and 3D as for the brush seal 3D models. With the 3D models, the section planes are defined as periodic interfaces. A periodic interface allows the fluid to exit one interface and then enter another interface with the same conditions at the exit, making fluid flow in an infinite loop as for a full 3D geometry. Housing and seals are treated as no-slip walls. The porous medium will be discussed in section 4.6 in detail. Figure 4.3 shows some of the boundary conditions on the labyrinth quarter model.

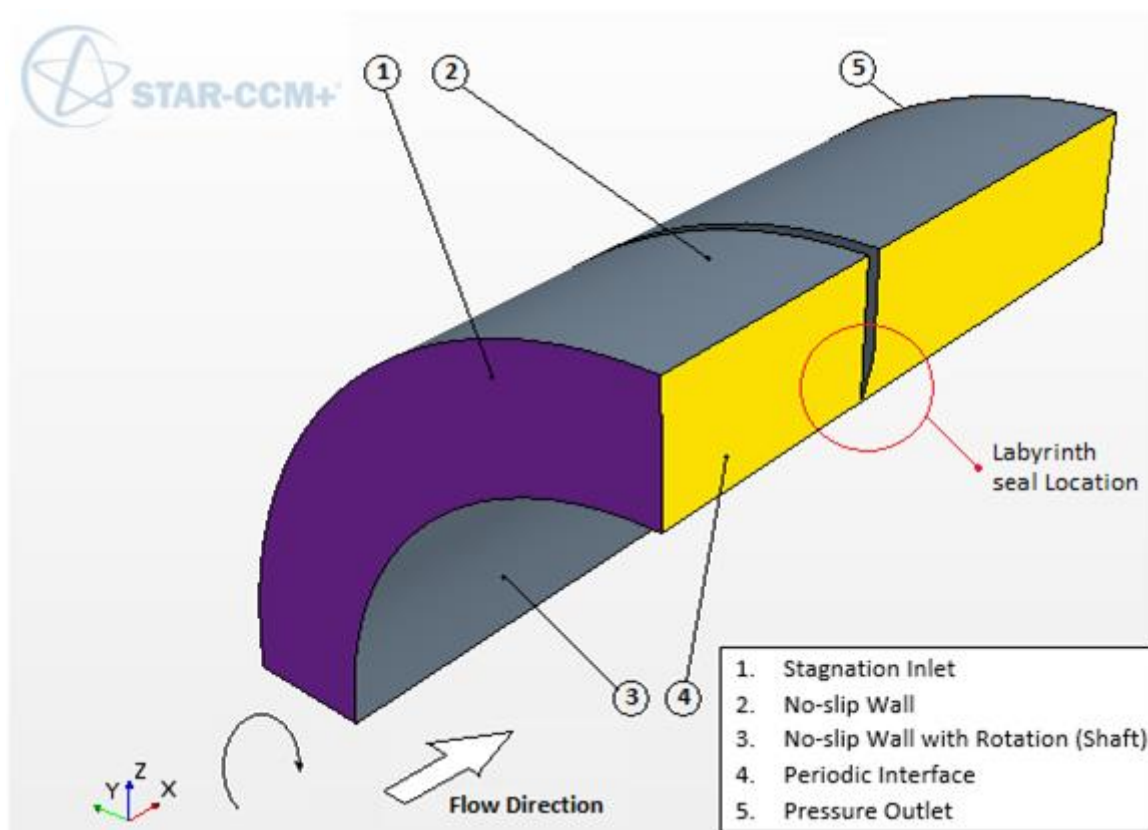


Figure 4.3 Boundary conditions of the Labyrinth quarter model

4.4. Mesh

STAR has many types of mesh models to select from. According to User guide (STAR, 2014) and Mendonca et al. (2005) the best type of cells for 3D simulation are Polyhedral cells. Polyhedral cells have the highest accuracy of any STAR mesh types, and therefore less cells are required than for other cells types. Polyhedral cells faces are orthogonal to the flow regardless of the flow direction. All the meshes in this dissertation make use of polyhedral cells.

4.4.1. Mesh with refinements

There are three mesh models, the 2D and 3D labyrinth as well as the 3D brush seal. All of these models use polyhedral cells and prism layers to create the surface and volume mesh. Volume metric controls are used to refine key areas.

Firstly the 2D labyrinth model is meshed, because it has similar geometry as the 3D model. This allows for a more efficient way to generate a good mesh. Two volumetric control zones are used. One around the seal gap and another downstream of the seal adjacent to the shaft surface. Figure 4.4 shows the refined mesh of the labyrinth 2D mesh.

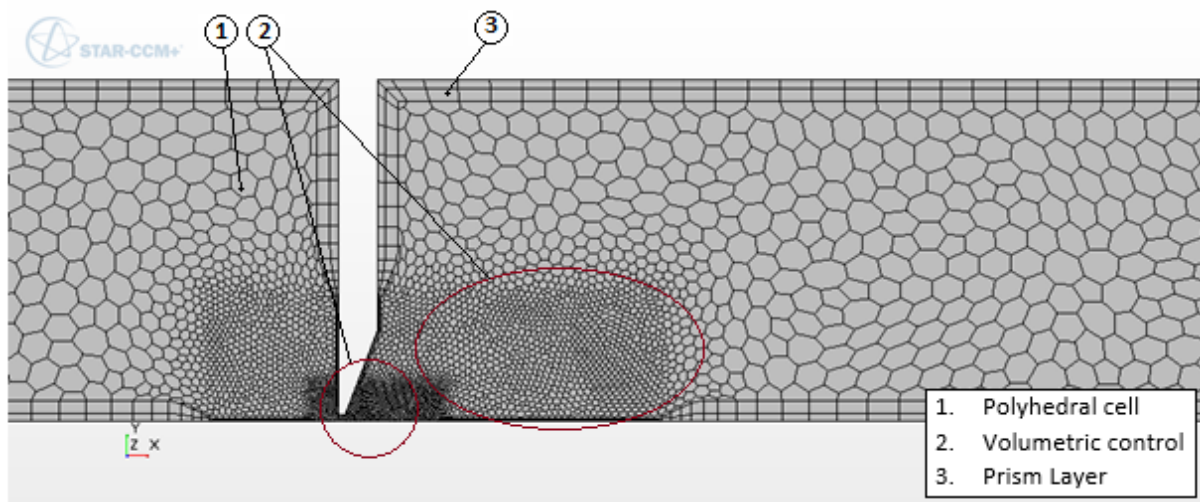


Figure 4.4 Refined 2D mesh of the labyrinth seal

Figure 4.5 shows the refined mesh of the labyrinth 3D mesh. The 3D mesh has the same size polyhedral cells and volumetric controls as the refined 2D mesh.

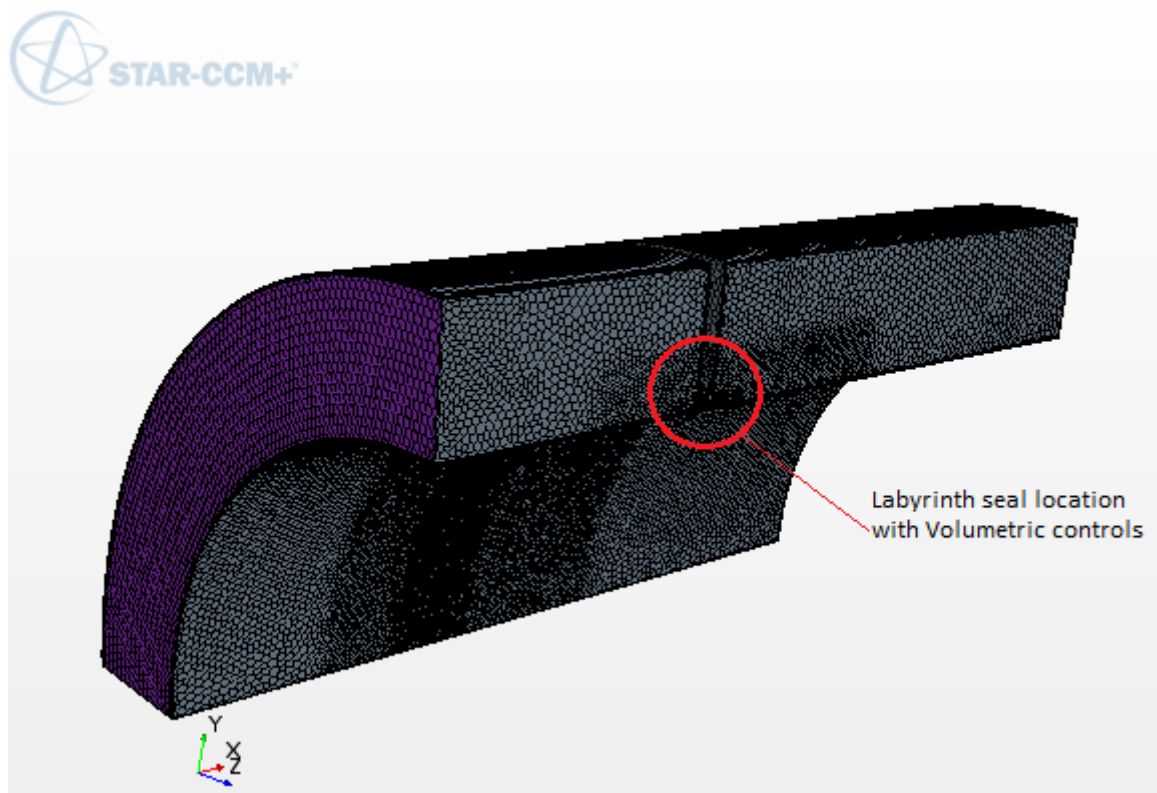


Figure 4.5. Refined 3D mesh of the labyrinth seal

4.4.2. Mesh independence

For each CFD study, a mesh independence study must be done. Mesh independence occurs when the results are independent from the mesh. This means that the mesh has to be refined to such a level where the results do not change within a certain percentage. The independence study for this dissertation makes use of the Grid Convergence Index (GCI) method of Roach (1998) and was done on the labyrinth 3D quarter model. The study consisted of running simulations for one set of conditions with different meshes. The conditions were 3 bar upstream pressure with 2000 rpm shaft speed and the meshes that were used consisted of 1 million, 2 million, 4 million, 8 million and 16 million cells each. The GCI method and the full mesh independent results are given in more detail in **Appendix G**.

The result of the mesh independence study is shown in Table 4.1.

Table 4.1 Mesh independence study results.

Numerical method (case 3bar at 2000 rpm)					
Mesh size	Performance parameter, f (Mass flow rate)	Order of Convergence, z	GCI 12	GCI 23	Asymptotic range
1 000 416	0.004307	-	-	-	-
2 000 560	0.004204	-	-0.0680	-	-
4 001 256	0.004146	-0.837	-0.0214	-0.0390	1.025
8 002 212	0.004134	-2.322	-0.0045	-0.0043	1.014
16 004 026	0.004132	-2.107	-	-0.0011	1.003

The graph in Figure 4.5 shows the mass flow rate versus the number of cells.

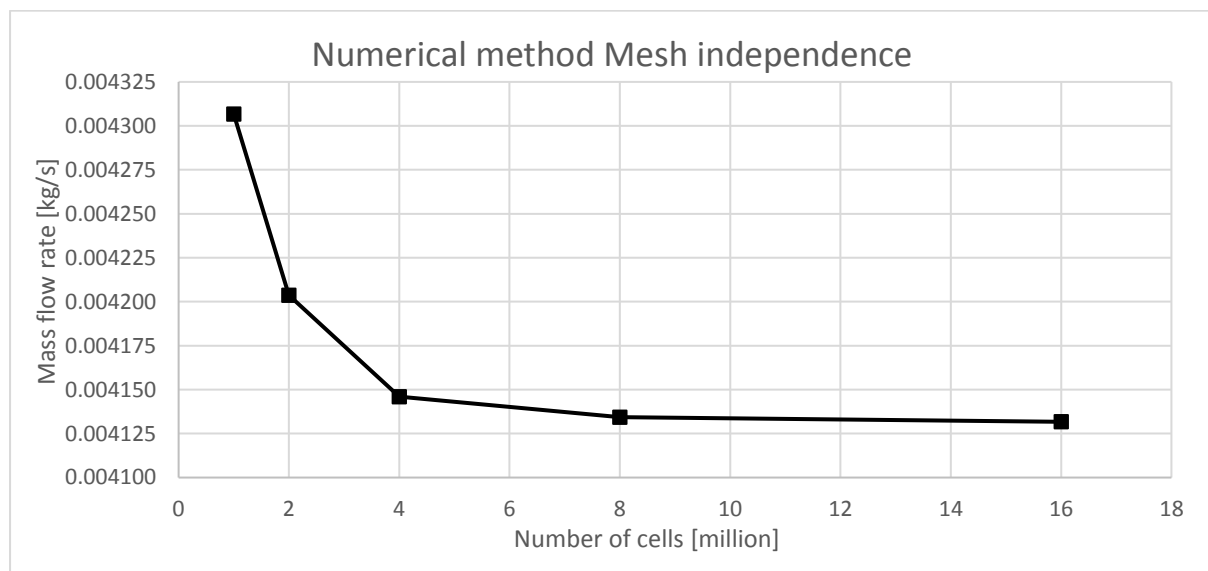


Figure 4.6 Graph of Mass flow rate vs number mesh cells

The study shows that with a 4 times finer mesh from 4 million cells there is less than 0.35% difference in the solution results. The first three performance parameters have an asymptotic range of approximately one. Therefore the solution is independent of the mesh for a mesh of 4 million cells and finer.

4.5. Material properties and solver settings

After the mesh has been generated, STAR allows one to setup the physics and solver for the simulation. A steady-state simulation is performed on a 3D domain.

The material properties describe the working fluid and continuum in which the simulation takes place. The material properties selected are gas as air and gas as an ideal gas for the working fluid. The air has a reference pressure of 87 kPa. The laboratory pressure is 87 kPa due to the altitude of the location which is at approximately 1300 m above sea level.

The standard Reynolds-averaged Navier-Stokes (RANS) equations are used for the steady-state simulation with turbulent solvers active. The active solvers are listed below:

- RANS
- Coupled Energy
- k - ω Turbulence, with SST(Menter) active
- All y^+ Wall Treatment
- Adjoint Flow
- Gradients
- Transition Boundary Distance

Menter's SST k - ω turbulence model was selected because it can deal with strong freestream sensitivity and the good prediction of adverse pressure gradients. Since all the CFD simulations in this study make use of a freestream inlet as the inlet boundary condition and have large pressure drops over the seals, this makes the SST k - ω turbulence solver ideal for this dissertation. A sample of the convergence history of the solvers is given in **Appendix K**, which shows that the solution of all the equations converges to the 5th order and higher.

4.6. Porous Medium

The brush seal is simulated as a porous medium since it is extremely difficult to simulate each bristle and its movement in CFD. The brush seal also contains a lot of entities and complexity, which require a lot of computation resources.

A porous medium is a section which represents a specified resistance. STAR allows one to set a resistance curve indirectly. Firstly a resistance curve is obtained with an experiment or supplied by the manufacturers. For this dissertation an experiment was done to find the resistance curve for the brush seal bristles, the experimental setup and procedure are listed in **Appendix E**. The resistance curve is shown in Figure 4.7.

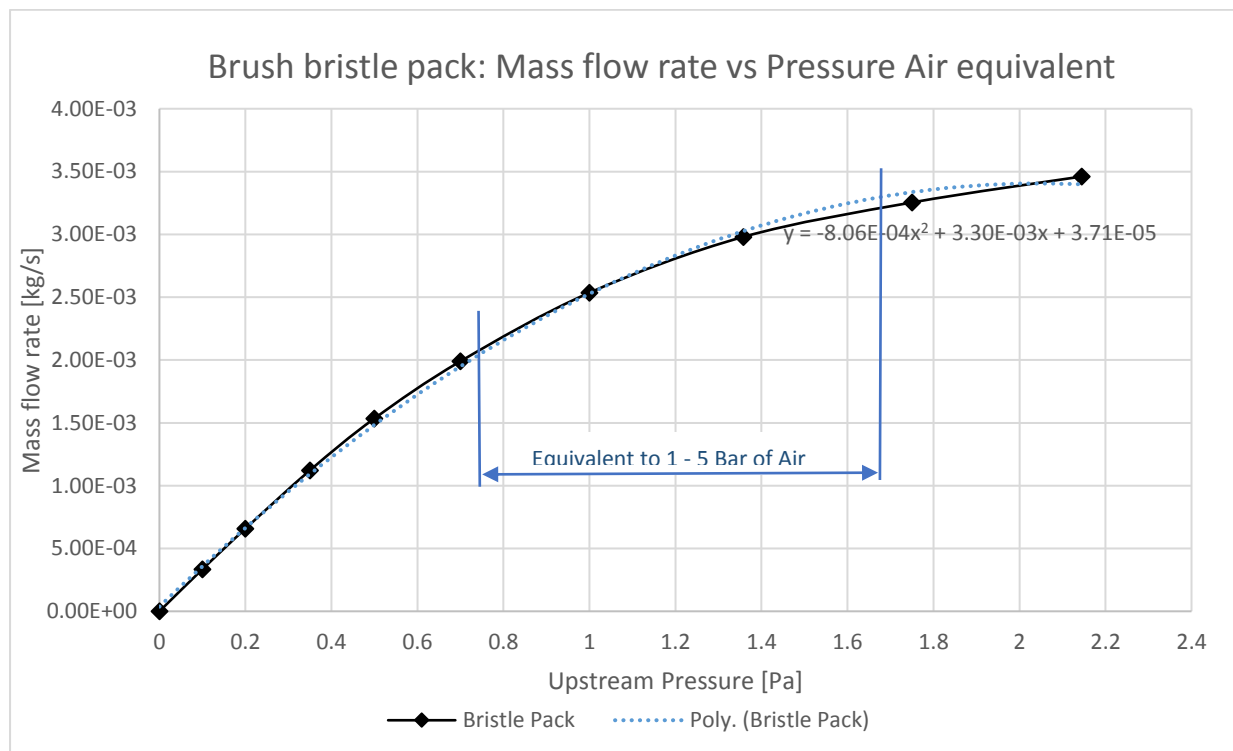


Figure 4.7 Resistance curve for the brush seal bristles

In STAR one cannot directly insert the coefficients of the resistance curve. The coefficients need to be rewritten in the following format:

$$P = \varphi + \rho\tau V + \frac{1}{2}\rho\alpha V^2 \quad [\text{eq 4.1}]$$

The coefficients α and τ in equation 4.1 are written in the following units:

$$\frac{\rho\alpha}{L} \left[\frac{\text{kg}}{\text{m}^4} \right] \quad [\text{eq 4.2}]$$

$$\frac{\rho\tau}{L} \left[\frac{kg}{m^3s} \right]$$

[eq 4.3]

Where the L is the length of the porous medium. The entire equations 4.2 and 4.3 are the coefficients that is used in STAR for the resistance. Equation 4.2 is the inertial resistance and equation 4.3 is the viscous resistance.

The porous medium makes use of the same mesh setup as the labyrinth seals and the air section of the brush seal. A validation simulation is done to check if the coefficients give the correct resistance. The validation used a rectangular domain with the porous medium located in the centre with the inlet and outlet set to a known condition. Figure 4.8 shows the result of the validation simulation.

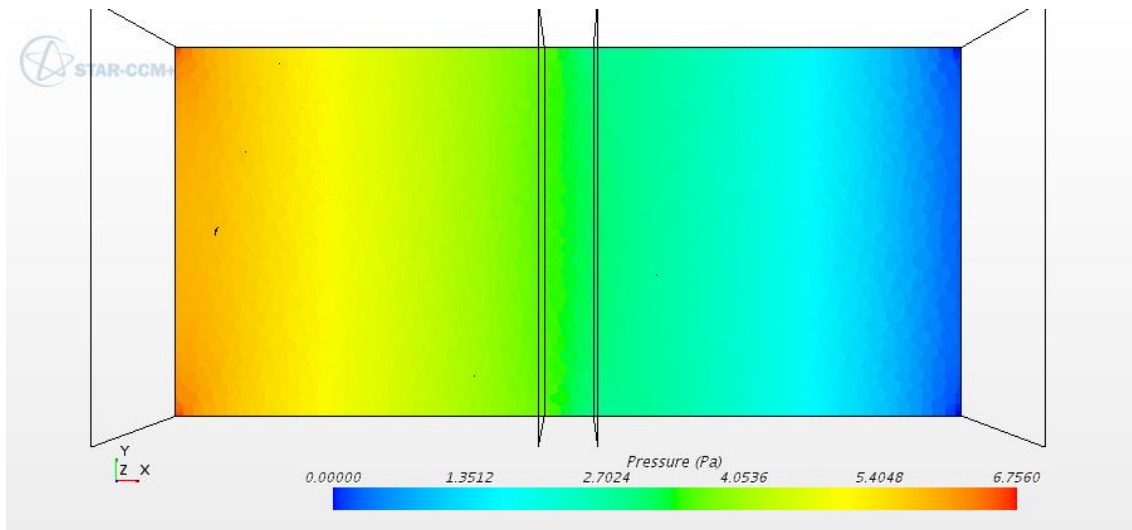


Figure 4.8 Result of Validation simulation of the porous medium

The results of the validation domain correlates with the results obtained for the coefficient of resistance test.

4.7. Summary

The numerical method makes use of commercial software to simulate the leakage flow through the non-contacting seals. The labyrinth seal is simulated as a 3D quarter model due to the axially-symmetric nature of the geometry and because it allows for a reduction in computational cost. The brush seal also used a 3D quarter model (for the same reasons as the labyrinth) with the brush bristles of the seal simulated as a porous medium.

A porous medium is used due to the complexity of the brush bristle's behaviour and sheer number of entities required to simulate an actual brush's geometry accurately. The coefficients of resistance are obtained experimentally.

The mesh independence study used the presented GCI method and showed that the refined mesh used in all the simulations are independent of the solutions. The GCI method showed that all the mesh refinements have an asymptotic range of one.

The solvers used are based on the steady-state RANS equations with the $k-\omega$ turbulence model active. The material properties were defined as ideal air with a reference pressure of 87 kPa. The residuals show that the energy equation's convergence was to 5 orders after about 10 000 iterations.

5.1. Introduction

In this chapter a calibration exercise is described that compares the experimental and numerical methods of Chapter 3 and Chapter 4. The calibration exercise is done on the orifice section of the experimental setup, to compare the difference between the flow rates measured with the experimental method and the flow rates obtained with the numerical method. The results of the exercise are a correlation between the methods, as well as an indication of the usable range of the experimental setup due to limitations in the system, mainly due to the capacity of the compressed air supply.

5.2 Calibration exercise

Since mass flow rate through a nozzle can easily be calculated with ASME flow equations (ASME, 1990) the calibration exercise is done on the orifice section of the experimental setup with a nozzle plate. A Matlab script performs the flow rate calculations, see **Appendix B**. The same orifice section with the nozzle plate is simulated in CFD and a flow rate is obtained. The diameter of the nozzle in each of the nozzle plates used in the calibration exercise was measured with an eyepiece graticule microscope to find the exact size of the nozzle diameter. These diameters are used in the Matlab script and the CFD simulation. This ensures that the simulated nozzle-hole size is the same as that tested in the experiment.

Different diameter nozzles were manufactured in order to allow for a range of nozzle areas to both enable investigation of the sensitivity of the measurement system as well as allow for different leakage areas to be considered. The nozzle diameters varied between 1 mm and 12 mm, the latter having a flow area that is approximately the same as the area of the full labyrinth seal leakage gap that will be investigated later, see **Appendix F**. Therefore the system must be able to accommodate at least a 12 mm nozzle accurately.

5.2.1. Experimental Setup

The experimental calibration setup is used with its experimental procedure explained in Section 3.1 and 3.4. The setup makes use of nozzle plates with nozzle diameters ranging from 1mm and increased to 12 mm in 1 mm increments. Figure 5.1 shows the 1 mm-diameter nozzle plate as representative.

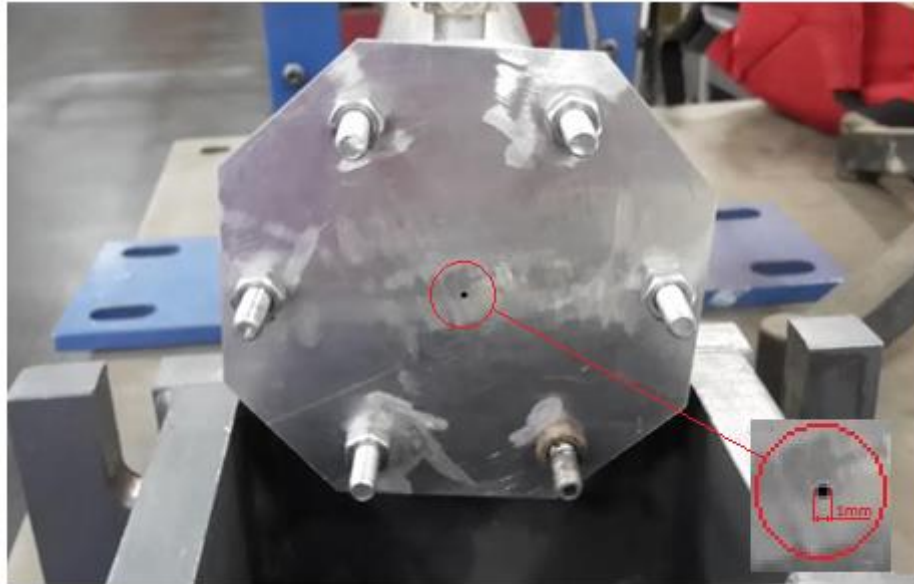


Figure 5.1 Nozzle plate with 1mm-diameter nozzle

5.2.2. Numerical setup

The geometry of the experimental calibration setup is used in the CFD simulations but in a half 3D symmetric model. The same mesh type (Polyhedral cells) is used for the calibration simulations as the seals described in the Numerical method (Chapter 4) and 2 million cells are used for each simulation of these 3D simulations. The mesh independent study results are listed in **Appendix G**. The inlet boundary condition (BC) is the upstream pressure and the outlet BC uses an atmospheric pressure (87 kPa). The same upstream pressures and nozzle diameters are simulated and compared in Section 5.3. Figure 5.2 shows the calibration exercise mesh for an 8 mm diameter nozzle with its boundary conditions.

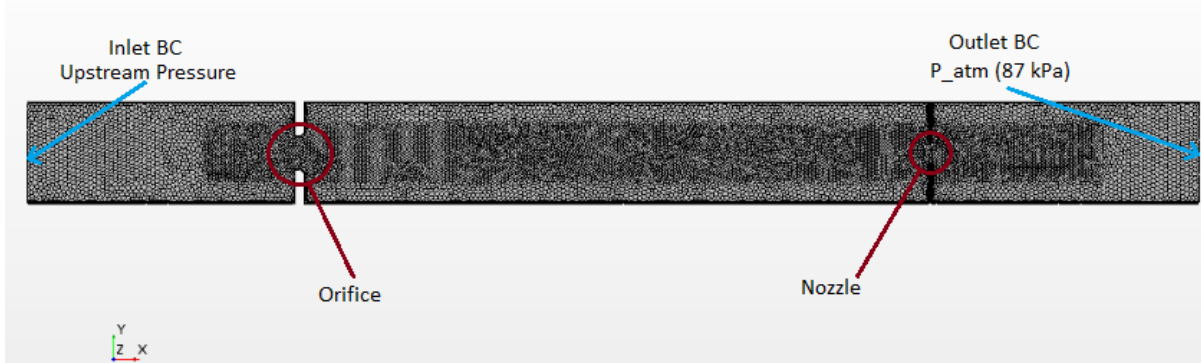


Figure 5.2 CFD Calibration exercise mesh for 8 mm-nozzle section on half model (approximate 2 million cells)

The mesh is located on an axial-symmetric plane for the half 3D CFD model for the Calibration exercise. Figure 5.3 show the front view of the inlet boundary condition of the Calibration exercise mesh.

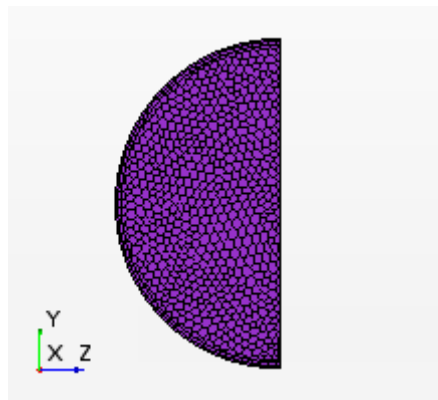


Figure 5.3 Front view of Mesh inlet boundary condition

5.3. Results

A large range of experiments and simulations were performed, ranging from small flow rates to a maximum flow rate. Each nozzle was tested with seven upstream pressures in order to vary the flow rate. The results are divided into three parts in this section and discussed. The first part investigates small changes in flow using the 1 mm-diameter nozzle. The second part describes the 12 mm-diameter nozzle that represents the maximum flow scenario and lastly the 8 mm-diameter nozzle results are presented to illustrate intermediate behaviour. The 8 mm nozzle was selected because its leakage area is midway between those of the 1mm and 12 mm nozzle. The full results can be seen in **Appendix G**.

The experimental and CFD comparison for the 1 mm-diameter nozzle is shown in Table 5.1 and Figure 5.4. The pressure used in the results is the gauge pressure as measured.

Table 5.1 Data of calibration exercise for 1mm-diameter nozzle

Pressure Upstream [kPa]	Experimental		CFD	
	Mass flowrate [10E-2 kg/s]	Upstream Velocity [m/s]	Mass flowrate [10E-2 kg/s]	Upstream Velocity [m/s]
100	0.70	2.26	0.71	2.50
200	1.59	2.56	1.61	2.60
300	2.48	2.66	2.51	2.70
400	3.36	2.71	3.41	2.75
500	4.25	2.75	4.31	2.78
600	5.15	2.77	5.21	2.80
700	6.04	2.78	6.11	2.82

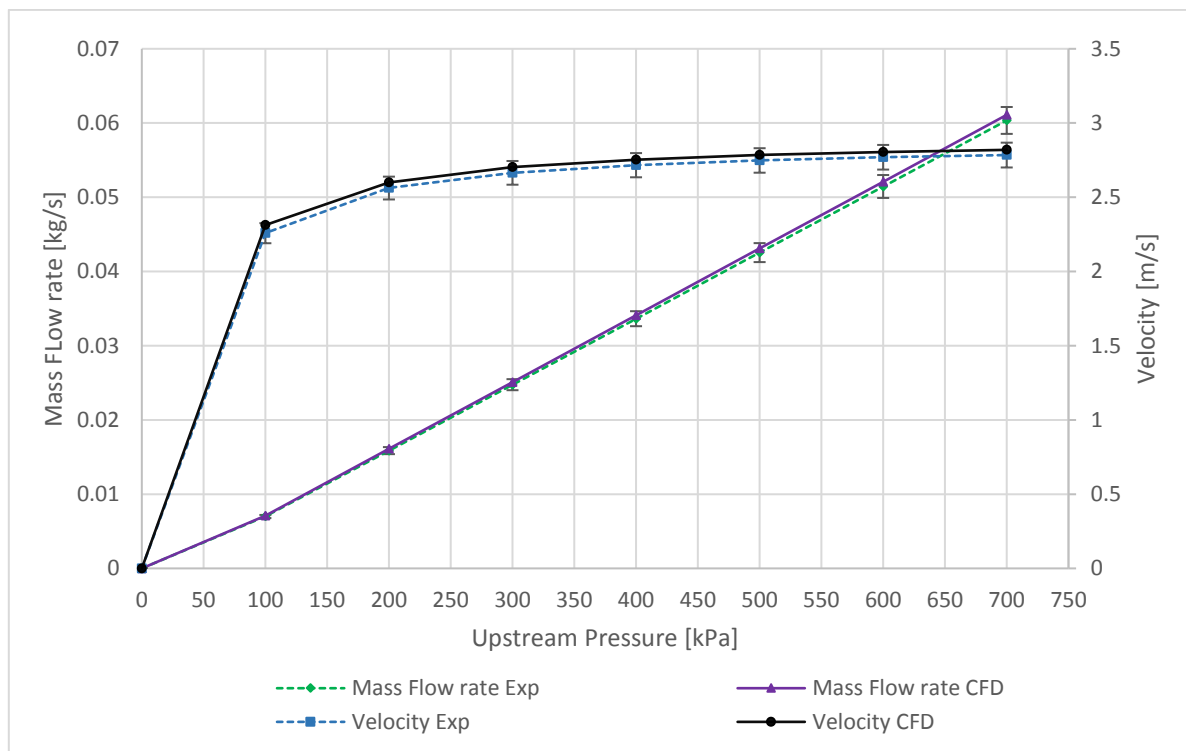


Figure 5.4 Calibration exercise: Mass flow rate for 1mm-diameter nozzle versus upstream pressure

The results in Table 5.1 and Figure 5.4 show that the mass flow has a linear trend, as the upstream pressure increases linearly as the mass flow increases. The results also show good correlation between the CFD and the experimental method throughout the pressure range that was tested, the largest difference between the methods being less than 1.5%. All the simulation results fall within the experimental uncertainty of 4.7% (9.4% error bar). The 1 mm-diameter nozzle indicates that the experimental setup will pick up small disturbances in flow.

The experimental and CFD comparison for the 8 mm diameter nozzle is shown in Table 5.2 and Figure 5.5.

Table 5.2 Data of calibration exercise for 8mm-diameter nozzle

Pressure Upstream [kPa]	Experimental		CFD	
	Mass flowrate [10E-1 kg/s]	Upstream Velocity [m/s]	Mass flowrate [10E-1 kg/s]	Upstream Velocity [m/s]
100	0.56	18.06	0.57	18.66
200	1.34	21.50	1.35	21.82
300	2.12	22.65	2.13	22.97
400	2.89	23.23	2.92	23.55
500	3.66	23.60	3.70	23.90
600	4.41	23.83	4.48	24.13
700	5.16	23.99	5.27	24.29

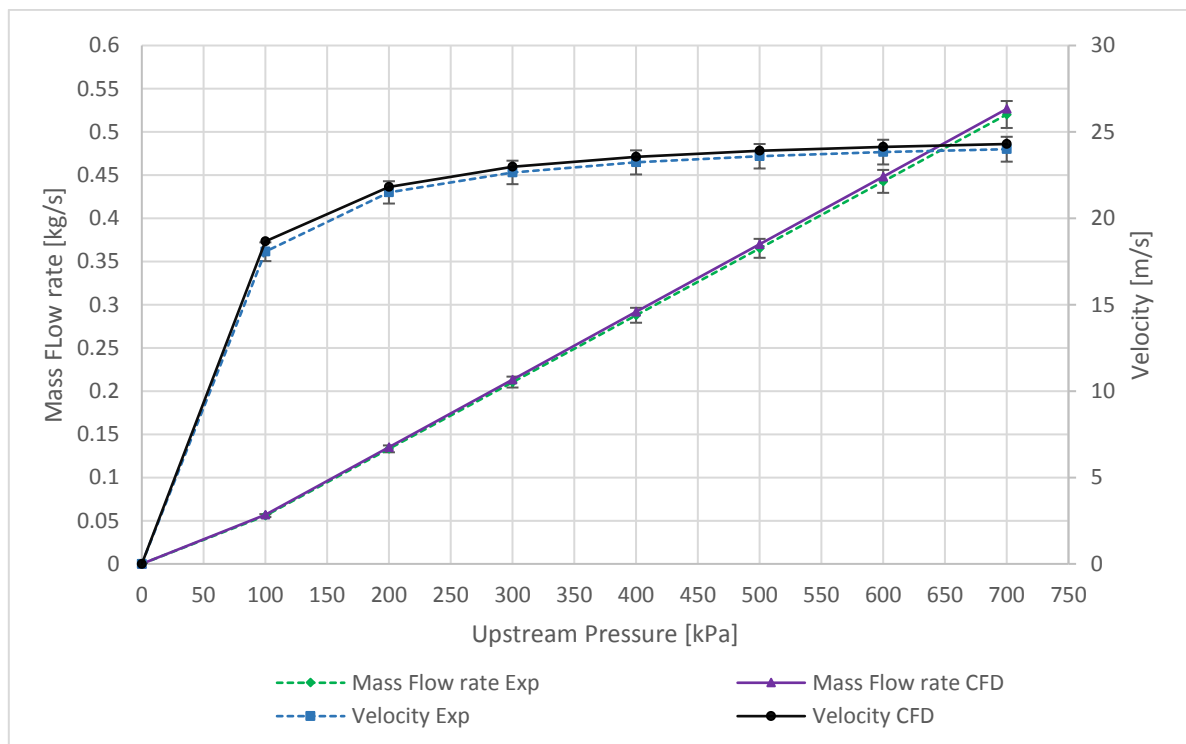


Figure 5.5 Calibration exercise, Mass flow rate for 8mm-diameter nozzle versus upstream pressure

The results in Table 5.2 and Figure 5.5 exhibit a linear trend and behaviour in fluid flow. The 8mm-diameter nozzle flow exhibits an even better correlation between the methods for upstream pressures less than 5 bar, with all the differences being less than 1%. Above 5 bar upstream the correlation weakens to about 2%, but all the pressure deviations are still within the experimental uncertainty. This shows that the experimental setup will pick up and simulate intermediate upstream pressures and mass flowrate accurately.

The experimental and CFD comparison for the 12 mm-diameter nozzle is shown in Table 5.3 and Figure 5.6.

Table 5.3 Data of calibration exercise for 12mm-diameter nozzle

Pressure Upstream [kPa]	Experimental		CFD	
	Mass flowrate [10E-1 kg/s]	Upstream Velocity [m/s]	Mass flowrate [10E-1 kg/s]	Upstream Velocity [m/s]
100	0.84	27.17	0.85	28.42
200	1.77	28.51	1.79	28.87
300	2.69	28.92	2.72	29.33
400	3.60	29.03	3.66	29.55
500	4.46	28.79	4.60	29.69
600	5.22	28.10	5.53	29.78
700	5.37	24.78	6.47	29.84

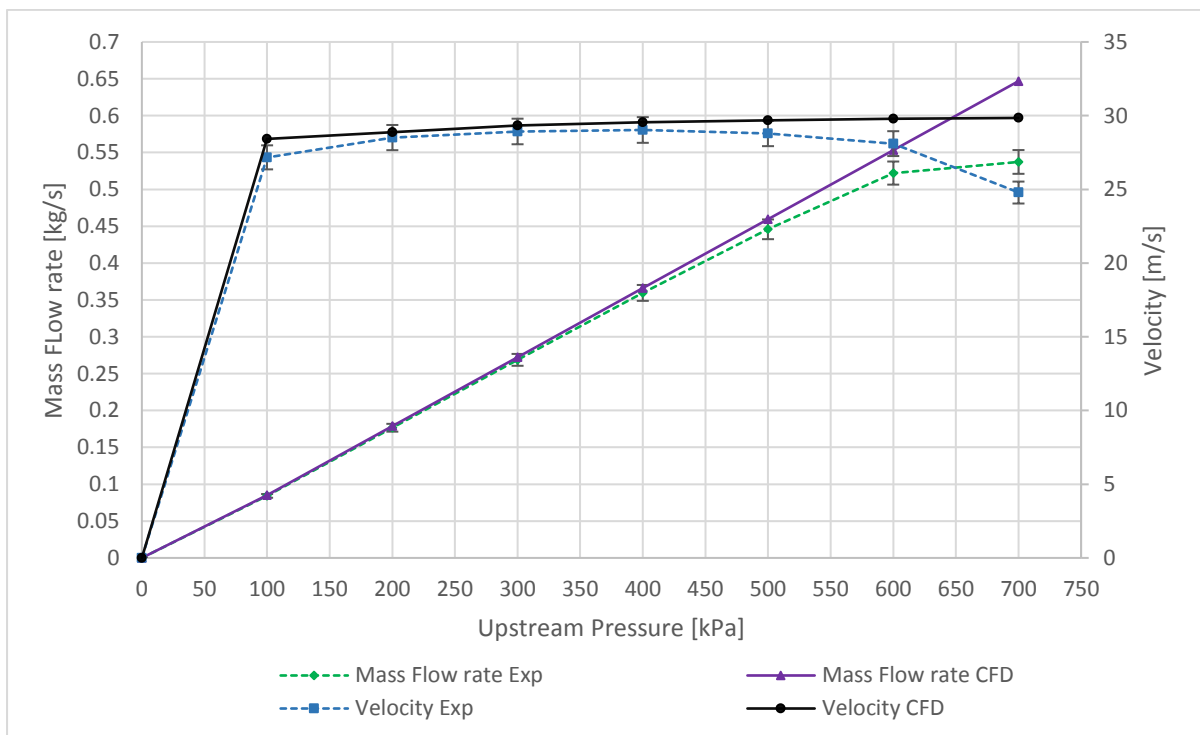


Figure 5.6 Calibration exercise, Mass flow rate for 12mm diameter nozzle versus upstream pressure

The results for 12mm-diameter nozzle in Table 5.3 and Figure 5.6 show more complex behaviour. The results show the same linear trend with good correlation between the methods for an upstream pressure of less than 4bar (400 kPa), with a maximum difference of less than 1.8%. Above 5 bar upstream the good correlation weakens and falls away. The experimental flow line no longer has a linear trend, but the CFD keeps its linear trend. For the 6 bar to 7 bar interval, correlations fall outside the experimental uncertainty of 4.7%. The difference above 6 bar upstream is calculated to be more than 15%. The experimental results start deviate from the numerical results at pressures high than 5 bar to the larger nozzle sizes (10 mm to 12 mm-diameter) due to the limitations of the compressed air supply. The system

can supply the desired pressure of 700 kPa, but cannot the supply and sustain the desired mass flow at 700 kPa. The compressed air supply storage is not sufficient for high flow rate and pressures required at a steady state condition. The CFD simulations do not have any limitation like the experimental setup and therefor continue with the upstream linear trend without deviating.

Since the relations between the mass flow and upstream pressures for the various nozzle sizes are linear up to the supply limit, the gradients of each of the linear trends for the different nozzles were calculated to determine the trend of how the mass flow rate increases against pressure.

Equation 5.1 describes a linear relationship between change in mass flow rate and change in upstream pressure:

$$\dot{m} = k\Delta p \quad [\text{Eq 5.1}]$$

To approximate k , the average slope was determined by using the mass flow rate difference at pressures 100 kPa and 700 kPa.

$$k = \frac{\dot{m}_{700\text{kPa}} - \dot{m}_{100\text{kPa}}}{600 \text{ kPa}} \quad [\text{Eq 5.2}]$$

Table 5.4 and Figure 5.7 show the gradient k , plotted against the various nozzle diameters for the numerical method's data.

Table 5.4 CFD trendline gradients for various nozzle-diameters

Nozzle diameter [mm]	CFD Trendline Gradient, k [x10E-3]
1	0.90
2	1.94
3	2.97
4	4.01
5	5.04
6	6.03
7	7.02
8	7.83
9	8.46
10	8.95
11	9.20
12	9.36

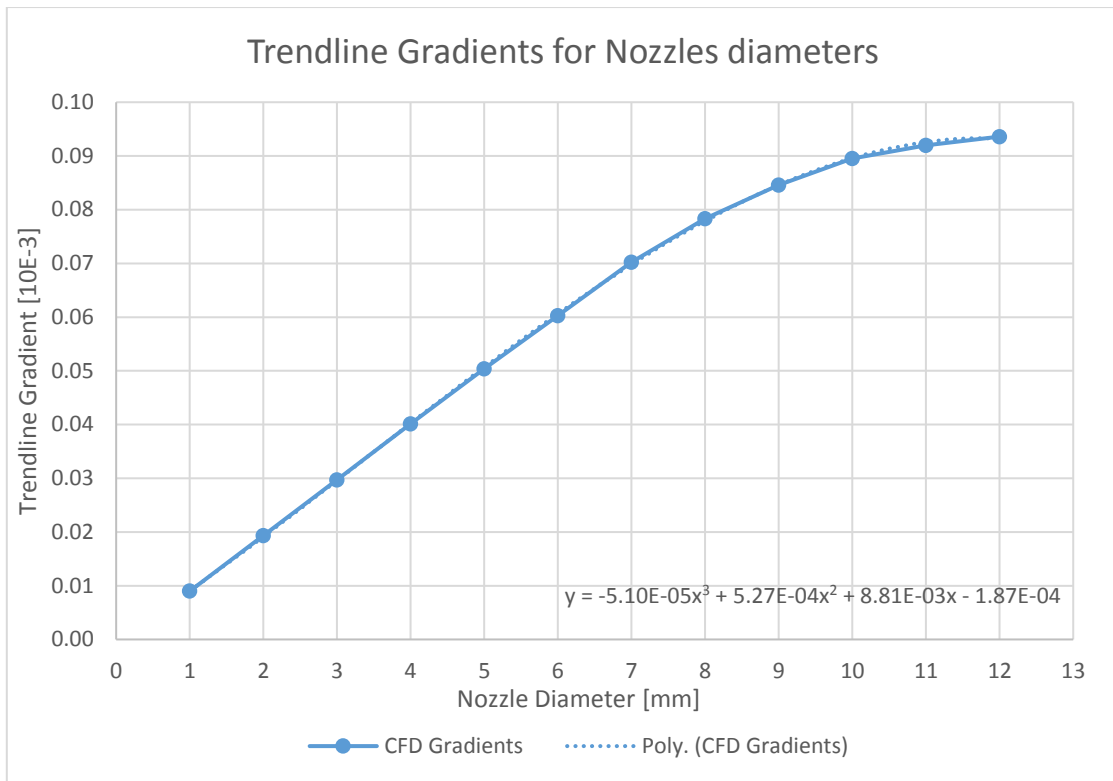


Figure 5.7 Trendline gradients for various Nozzle diameters

Figure 5.7 shows that at the smaller diameters choking of the flow occurs, since the increase is linear. At the larger diameters there is less of a choking effect, since the trend no longer increases linearly with nozzle-diameters, but tends to a constant gradient value. When designing a seal, the choking of flow is good for the restriction of leakage flow. The gradient trendline correlates to a polynomial of third order. The polynomial can be used to predict the gradient of the trend line for larger nozzle-diameters taking care when extrapolating.

The CFD results are used to investigate the behaviour of the flow in more detail. Figure 5.8 shows the simulation of 1 mm, 8 mm and 12 mm nozzles on the same scale with a 4 bar upstream pressure.

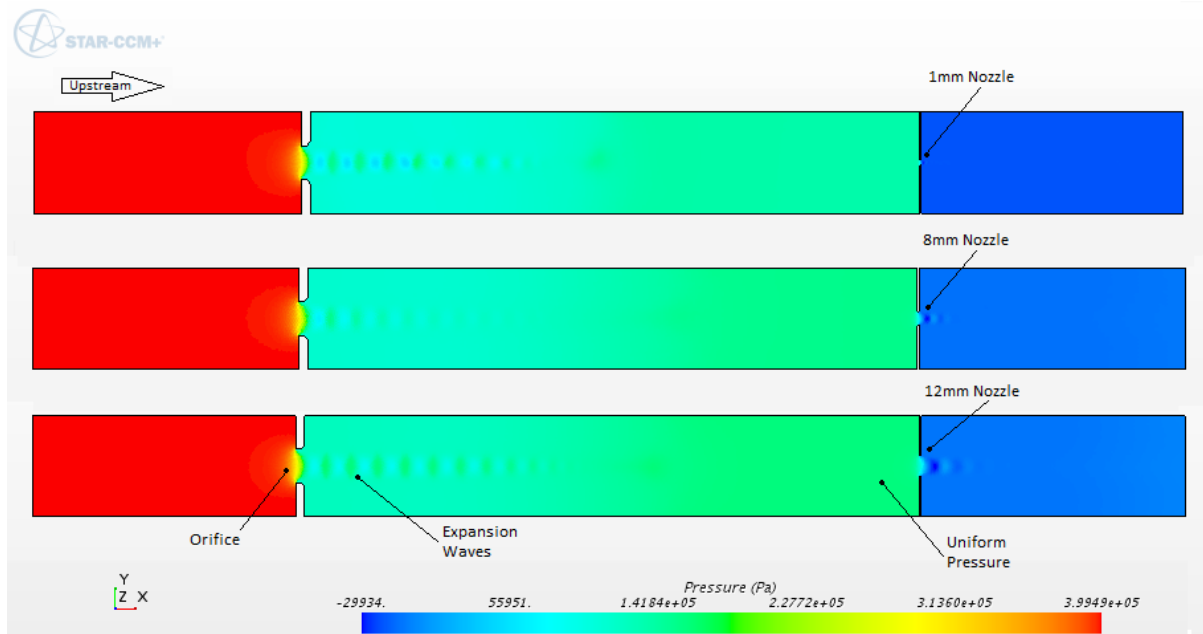


Figure 5.8 Calibration exercise, CFD of 1mm, 8mm and 12mm nozzle at 4 bar upstream

The colours clearly show the difference in pressure over the orifice. There are also expansion waves visible. The pressure is uniform before the nozzle which shows that the downstream distance from the orifice to the nozzle is far enough and will not influence the flow behaviour of the nozzle or seal that is tested. There is very little difference visible in pressure drop over the orifice for the various nozzle sizes. The expansion waves are more visible for the larger size nozzles, this is due to the increase in flow area in the nozzle throat.

Figure 5.9 shows the temperature changes in the system for 1mm, 8mm and 12mm-diameter nozzle on the same scale with a 4 bar upstream pressure.

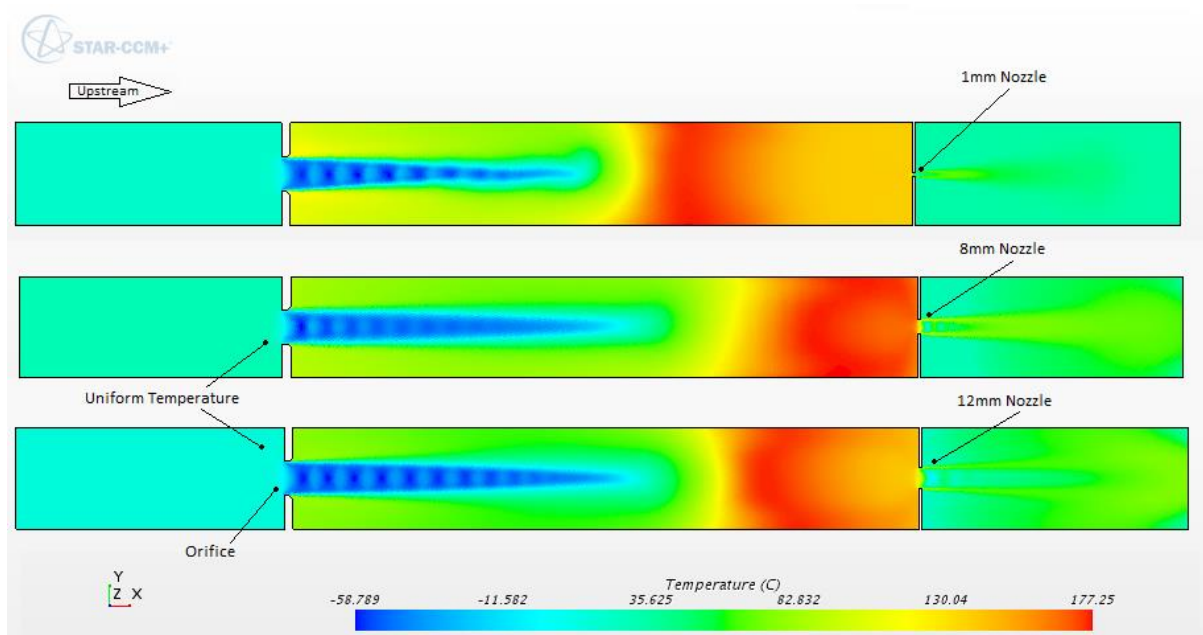


Figure 5.9 Calibration exercise CFD temperature change in system

The temperature stays uniform for the entire upstream section before the orifice for all cases. This shows that the placement of the temperature gauge upstream of the orifice is not critical to the reading. The temperature drops rapidly downstream of the orifice to a temperature below freezing due to the sudden pressure drop in the fluid. The temperature rises above 170°C upstream of the nozzle, and this correlates to the gas laws of compressed fluids. The temperature drops to just above room temperature downstream of the nozzle. The larger nozzle sizes have a longer and thicker jet-tail after the orifice, this is due to the higher mass flow rate through the nozzle. It is also clear that the fluid compresses earlier upstream to the nozzle for the smaller nozzle sizes. The maximum temperature of 177.25 °C is achieved with the 12 mm nozzle. The 1 mm nozzle shows non-symmetric behaviour downstream of the orifice. This does influence the mass flow rate through the nozzle but shows that there are some turbulent movements at the end of the expansion waves.

Figure 5.10 shows the Mach number contours of the fluid flow in the 1 mm, 8 mm and 12 mm-diameter nozzles.

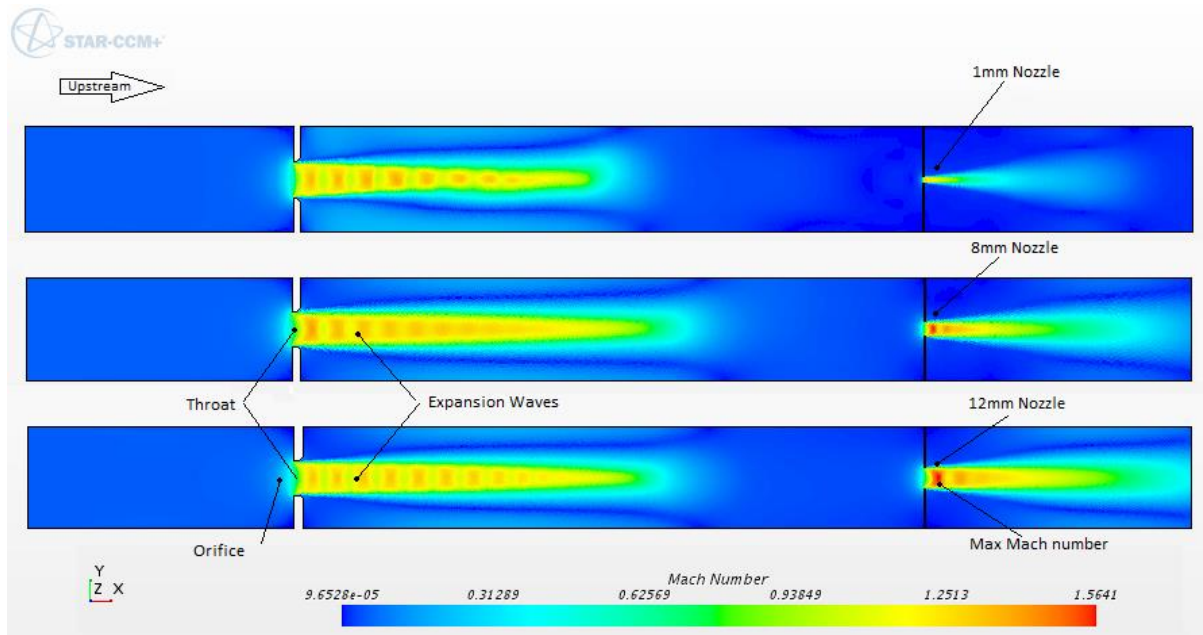


Figure 5.10 Calibration exercise CFD Mach number contours

Figure 5.10 shows that the flow goes supersonic downstream of the orifice and nozzle. The flow at throat of the orifice is at Mach 1. Expansion waves form downstream of the orifice due to the rapid expansion of the compressed fluid. The waves are small and deplete slowly downstream with multiple ripples. The downstream nozzle has similar characteristics as the upstream orifice, with slight differences: the downstream expansion is more rapid and the flow achieves a higher Mach number. The expansion waves are visible and deplete fast with only a few ripples downstream. The maximum Mach number of over 1.5 is achieved with the 12mm nozzle.

5.4 Conclusion

The experimental method and the numerical method correlate well. The percentage differences between the experimental and CFD simulations are fully within the experimental uncertainty for all cases where the setup could supply sufficient air. It was found that experimental data started to deviate from the simulated CFD data above 5 bar upstream pressure for the largest tested nozzle-diameter due to air supply limitations. This calibration exercise has confirmed that the usable range of the setup is between 0 and 5 bar upstream pressure, regardless of flow rate. This range is used for all the tests of the seals to be described in the next chapter. The best correlation was found for intermediate flow rates for the pressure range of 2 to 4 bar upstream. The knowledge gained in the calibration exercise will be used extensively in the analysis of the seals.

Chapter 6 – Labyrinth and Brush seals Performance Analysis

6.1. Introduction

This chapter illustrates and discusses the results obtained for seal geometries using both the experimental method (described in Chapter 3) and the numerical method (described and validated in Chapter 4 and 5, respectively). These methods are applied to both labyrinth and brush seals and compared as discussed in this chapter. For the two seals, emphasis is placed on their flow behaviour and what influence shaft rotation has on the leakage rate. Finally, seal design guidelines are suggested based on the results.

6.2. Labyrinth and Brush seal results

The labyrinth and brush seals that were tested and simulated were discussed in Chapter 3 (experimental setup and method) and 4 (numerical method). The full set of experimental data with CFD counterparts is given in **Appendix H** and **I**. For discussion purposes in this chapter, only three of the shaft speeds are presented here as well as a stationary shaft. The speeds are 1 000 rpm, 6 000 rpm and 10 000 rpm. The 1 000 rpm results exhibited small variations in leakage rate while 10 000 rpm results represent the maximum shaft speed that was tested.

Tables 6.1 and 6.2 list the results of the stationary shaft and the maximum shaft speed of 10 000 rpm for the labyrinth and brush seal. Figures 6.1 and 6.2 plot the comparison between the experimental and CFD results for the stationary shaft and shaft speed of 10 000 rpm for both seals.

Table 6.1 Labyrinth seal stationary shaft and 10 000 rpm shaft speed: Leakage rates for different upstream pressures.

Pressure Upstream [kPa]	Stationary (0 rpm)		10 000 rpm	
	Experimental Mass flowrate [10E-4 kg/s]	CFD Mass flowrate [10E-4 kg/s]	Experimental Mass flowrate [10E-4 kg/s]	CFD Mass flowrate [10E-4 kg/s]
100	2.00	2.03	2.04	2.06
200	3.09	3.14	3.14	3.19
300	4.15	4.23	4.22	4.30
400	5.22	5.32	5.30	5.41
500	6.29	6.41	6.39	6.52

Table 6.2 Brush seal stationary shaft and 10 000 rpm shaft speed: Leakage rates for different upstream pressures

Pressure Upstream [kPa]	Stationary (0 rpm)		10 000 rpm	
	Experimental Mass flowrate [10^{-4} kg/s]	CFD Mass flowrate [10^{-4} kg/s]	Experimental Mass flowrate [10^{-4} kg/s]	CFD Mass flowrate [10^{-4} kg/s]
100	1.88	1.93	1.91	1.96
200	2.89	2.97	2.94	3.02
300	3.88	3.99	3.94	4.05
400	4.85	4.99	4.92	5.07
500	5.82	6.00	5.90	6.10

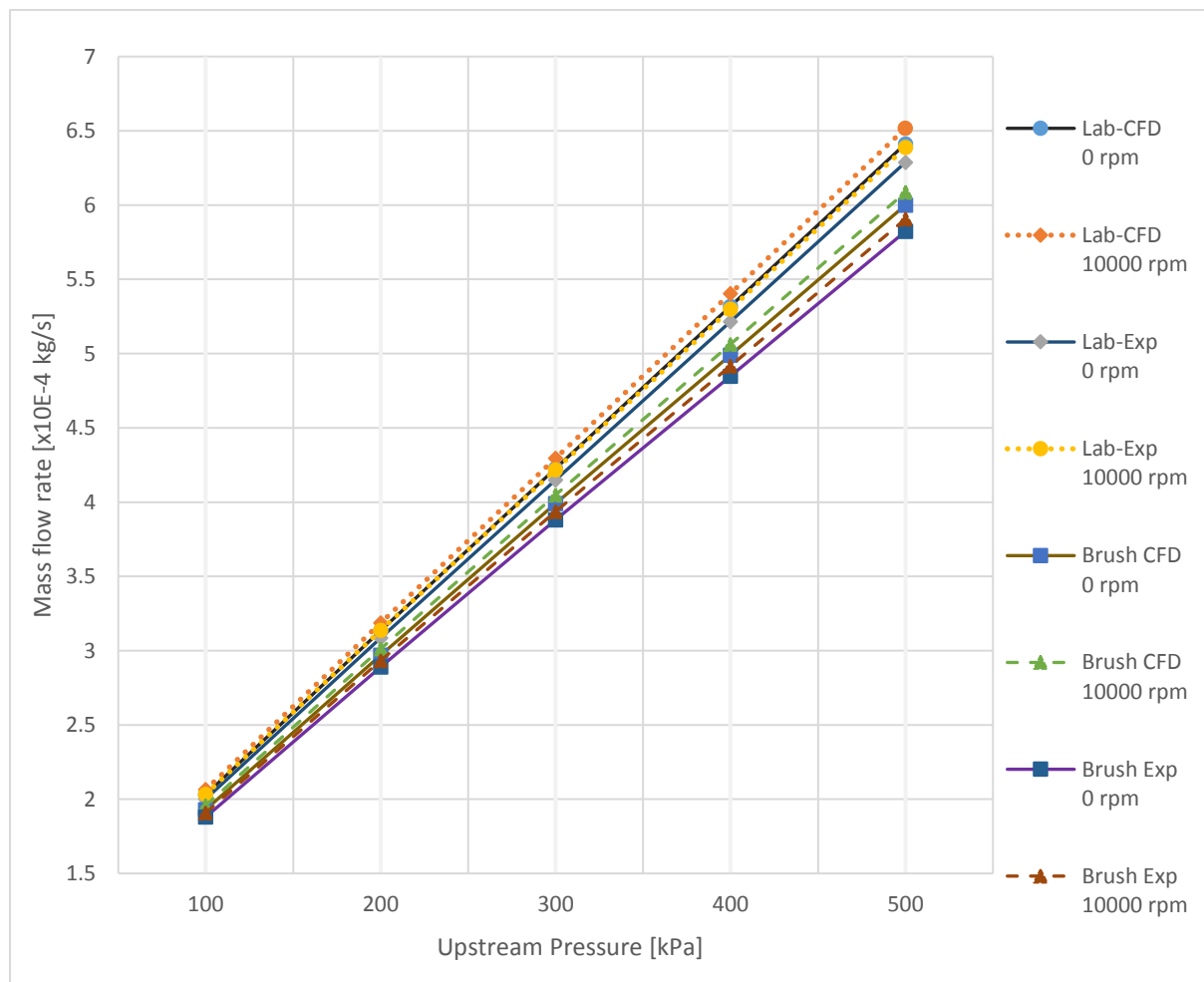


Figure 6.1 Labyrinth and Brush seal leakage rate for 0 and 10 000 rpm shaft speed at different upstream pressures

The leakage rate increases linearly as the upstream pressure increases. The leakage rate also increases as the shaft speed increases, with a 0.002% increase for 1000rpm over the stationary shaft. The difference is only visible at the fifth decimal. The experimental and numerical results show good correlation throughout the entire pressure range that was tested with a slight difference in slope. The flow also increases significantly more between 6000 rpm and 10 000 rpm than between 0 and 1000 rpm, with about a 1.3% increase.

The difference in the slopes for the different shaft speeds is evident in both the CFD and experiment. The results for the brush seal show the same overall behaviour as for the labyrinth seal.

Since all the relations between leakage rates and upstream pressures for the various shafts speed are linear with slight slope changes, the gradients of each of the linear trends for the different shafts speed are calculated to determine the trend of how the leakage rate increases with shaft speed. Figure 6.3 defines the gradient and eq 6.2 illustrates how the gradient, k is calculated.

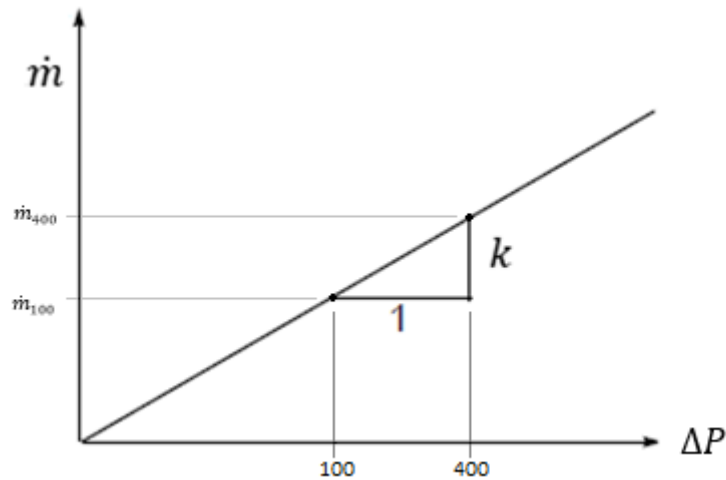


Figure 6.2 Mass flow vs Pressure gradient

Equation 6.1 describes a linear relationship between change in leakage rate and change in upstream pressure;

$$\dot{m} = k\Delta p \quad [\text{Eq 6.1}]$$

To approximate k , the average slope was determined by using the difference in mass flow rates at 100 kPa and 400 kPa.

$$k = \frac{\dot{m}_{400\text{kPa}} - \dot{m}_{100\text{kPa}}}{300\text{ kPa}} \quad [\text{Eq 6.2}]$$

Tables 6.3 and 6.4 list the gradients for the labyrinth and brush seals and Figure 6.4 shows k plotted against the various shafts speeds for both the experimental and the numerical data as well as for both seals.

Table 6.3 Labyrinth seal Trendlines gradients

Trendline Gradients, <i>k</i>		
Shaft speed [rpm]	Experimental [10^{-6}]	Numerical [10^{-6}]
0	1.072	1.096
1000	1.072	1.096
2000	1.072	1.096
3000	1.072	1.096
4000	1.073	1.097
5000	1.074	1.098
6000	1.075	1.100
7000	1.077	1.102
8000	1.080	1.105
9000	1.084	1.109
10 000	1.089	1.113

Table 6.4 Brush seal Trendlines gradients

Trendline Gradients, <i>k</i>		
Shaft speed [rpm]	Experimental [10^{-6}]	Numerical [10^{-6}]
0	0.989	1.020
1000	0.989	1.020
2000	0.989	1.021
3000	0.990	1.021
4000	0.991	1.022
5000	0.992	1.023
6000	0.994	1.025
7000	0.996	1.027
8000	0.998	1.030
9000	1.000	1.032
10 000	1.003	1.035

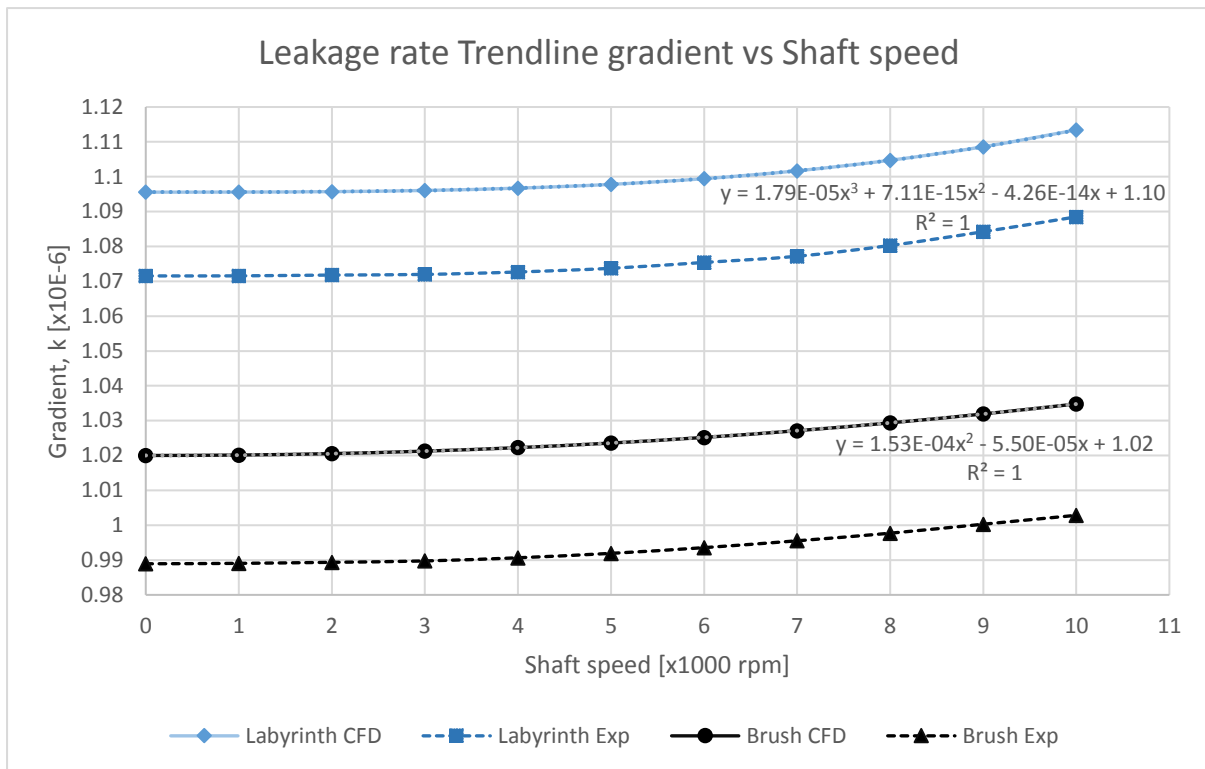


Figure 6.3 Trendline gradients for Labyrinth and Brush seals with various shaft speeds

The labyrinth seal leakage rate increases in the 3rd order for a linear increase shaft speed, for both the experimental and numerical method. The experimental values are lower than the numerical values for the entire range of shaft speeds that were tested. This can be due to the reference pressure selected for the CFD simulations. The reference pressure used is an approximation of the altitude as which the experimental tests were conducted, which is approximately above 1300m sea level with no exact value measured. It was found that the maximum increase in leakage rate relative to the stationary shaft was at the maximum tested speed of 10 000 rpm, where the leakage rate increased by 1.63%.

The brush seal leakage rate increases in the 2nd order for a linear increase in shaft speed, for both the experimental and numerical method. It was found that the maximum increase in leakage rate relative to the stationary shaft was at the maximum tested speed of 10 000 rpm, where the leakage rate increased by 1.45%. This means that the brush seal is less affected by shaft rotation than the labyrinth seal.

The results show that the brush seal leaks 5% less than the labyrinth at the labyrinth's best case of a stationary shaft and 1 bar upstream pressure. The brush seal leaks about 6.5% less than the labyrinth at the worst case which is the 10 000 rpm shaft speed and a 5 bar upstream pressure. Shaft rotation therefore has less of an effect on the brush seal than the labyrinth seal.

6.2.1. Error Analysis

Through the entire range of variables tested there is little deviation in error difference between experimental and numerical methods with change in shaft speed, but there is significant more deviation with the change in upstream pressure. The error difference fluctuates less than 0.1% through the shaft speed range of 1000 – 10 000 rpm for each upstream pressure. Table 6.4 and Figure 6.4 show the average percentage difference between the experimental and numerical methods for all the shaft speeds.

Table 6.5 Average percentage difference of leakage rate between Experimental and CFD

Upstream Pressures [kPa]	Labyrinth seal percentage difference [%]	Brush seal percentage difference [%]
100	1.47	2.58
200	1.61	2.67
300	1.81	2.75
400	1.92	2.87
500	1.94	2.96

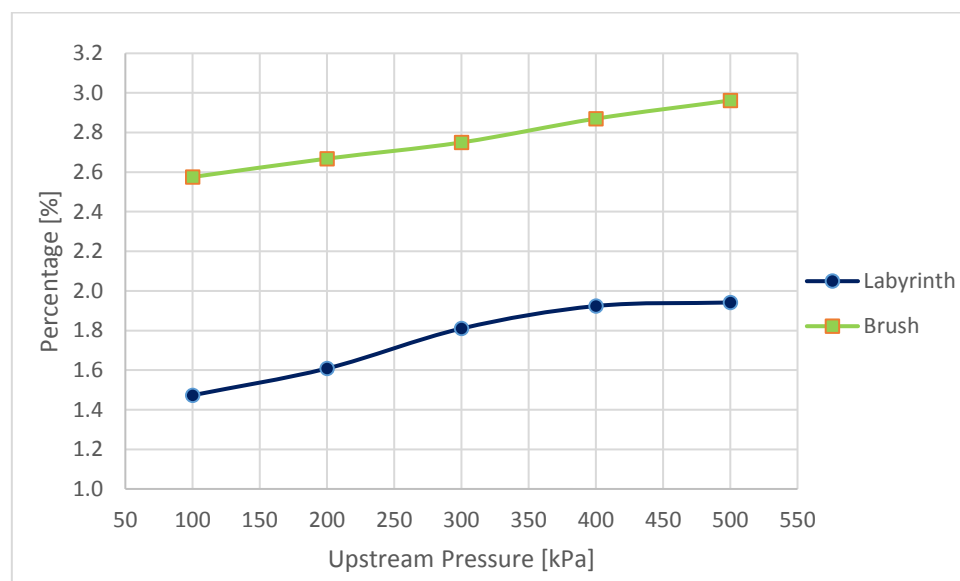


Figure 6.4 Average percentage difference between the Experimental and CFD for all shaft speeds

All the simulation results of the labyrinth seal fall within the experimental uncertainty of 3%, thus 6% error interval, with the largest difference being 2.0% for the highest pressure difference across the seal. Similar to the labyrinth seal, all the simulation results of the brush fall within the experimental uncertainty of 4.7%, thus 9.4% error interval. The brush seal has on average a 1% larger percentage difference than the labyrinth seal, with the largest difference between the two methods being 2.96%. The full results can be seen in **Appendix H** and **I**.

6.2.2. Detailed CFD results

The CFD method provides a lot more detailed information about the problem as discussed in this section. The integrated quantities like leakage flow rate correlated well to the experimental data but of interest are the detailed flow patterns and phenomena that accompany these to help explain the differences noted above.

Figure 6.5 shows the CFD Pressure distribution of the labyrinth seal with 3 bar pressure upstream with an enlarged section of the labyrinth seal tip.

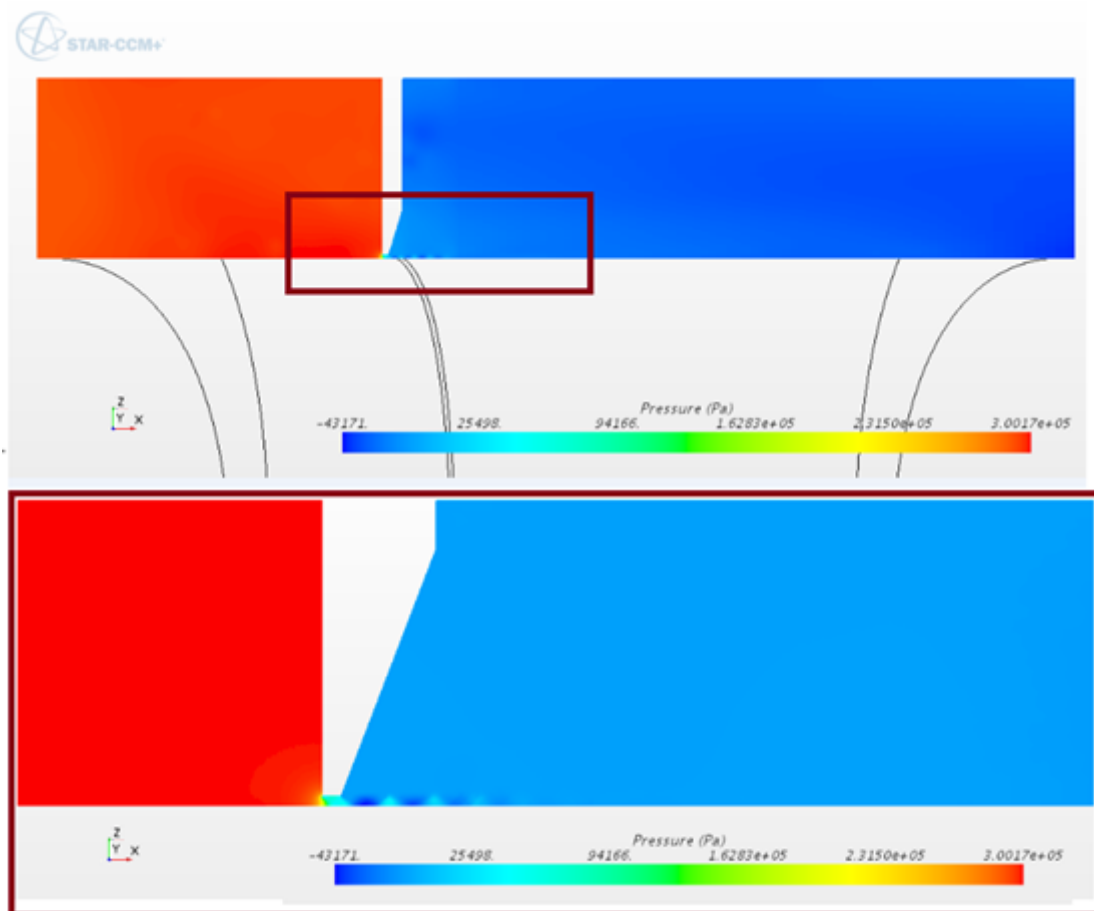


Figure 6.5 Labyrinth seal CFD Pressure distribution with enlarged section of 3D model

There is a clear difference between the pressure upstream and downstream. There are almost no changes at the inlet and outlet boundaries, this shows that the boundaries are far enough not to have an influence on the leakage of the seal. There are expansion waves visible at the downstream side of the seal as for the orifice in Chapter 5. Due to a limitation in mesh count for the 3D problem, they are not resolved to the same extent as in the previous 2D simulations in Chapter 5.

Figure 6.6 shows an enlarged CFD of the pressure distribution of the brush seal with 3 bar pressure upstream.

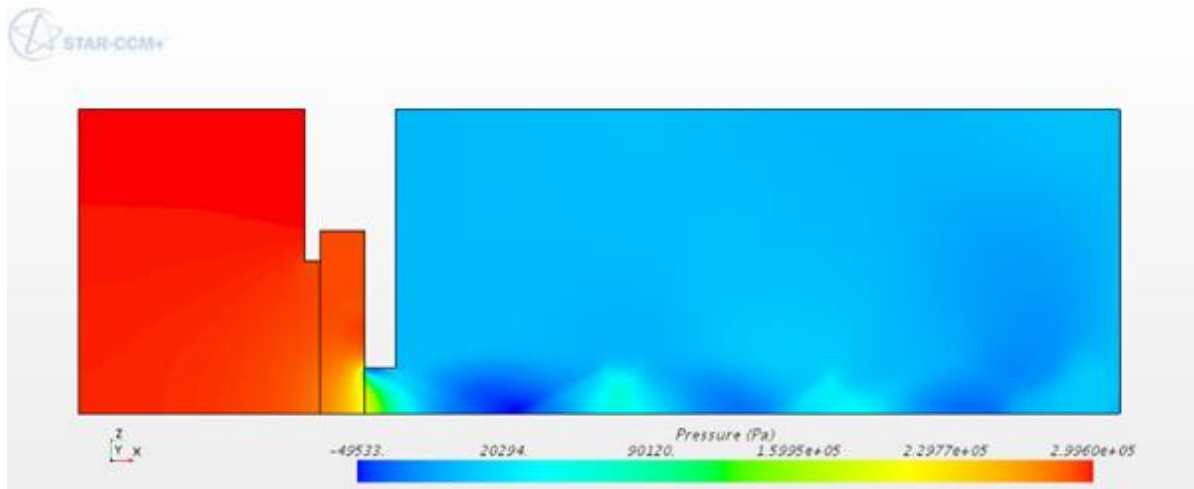


Figure 6.6 Brush seal CFD Pressure distribution with enlarged section

The pressure difference over the seal has the same behaviour as the labyrinth seal. The expansion waves have similar behaviour and are visible at the downstream side of the seal.

Figure 6.7 shows Mach number contours on the enlarged section of the labyrinth seal for the 3 bar upstream pressure. The seal gap has sonic flow ($M = 1$) as expected with the flow accelerating and decelerating in the expansion waves downstream of the gap.

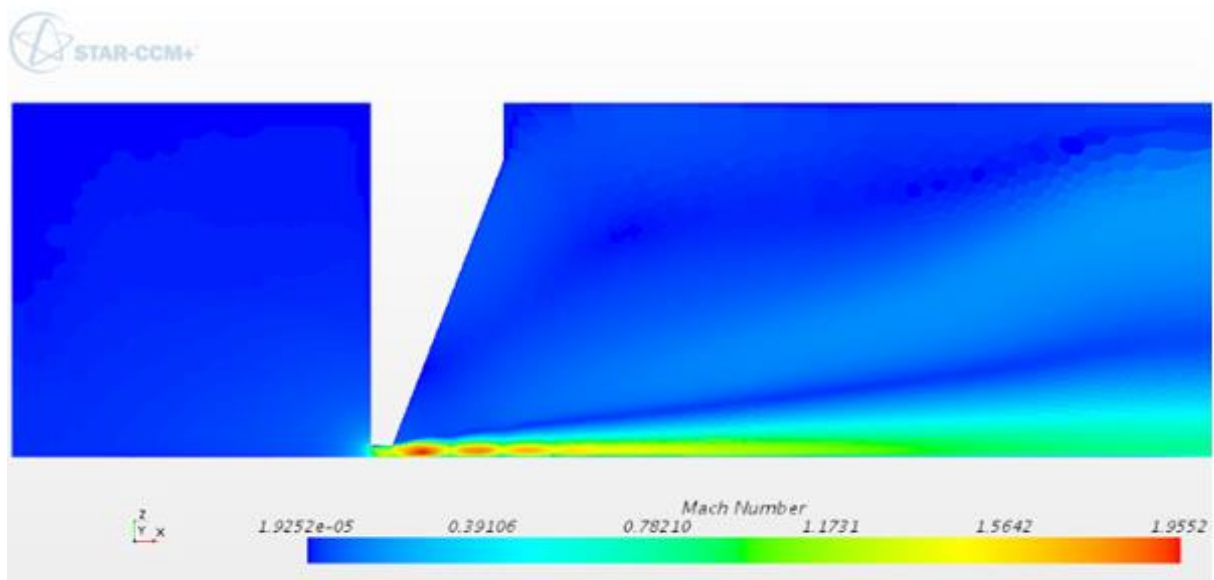


Figure 6.7 Labyrinth seal enlarged section with Mach numbers

By examining the flow through the seal it is clear that there is an increase in Mach number. The Mach number exceeds 1, which means the flow is supersonic in those areas. The flow and Mach numbers suggest that the labyrinth seal acts like a convergent-divergent nozzle, where the flow enters sub-sonic and exits super-sonic. It shows the same characteristics as a nozzle with choked flow.

Figure 6.8 show an enlarge section of the brush seal for 3 bar upstream pressure, with Mach numbers and the expansion waves over the porous medium.

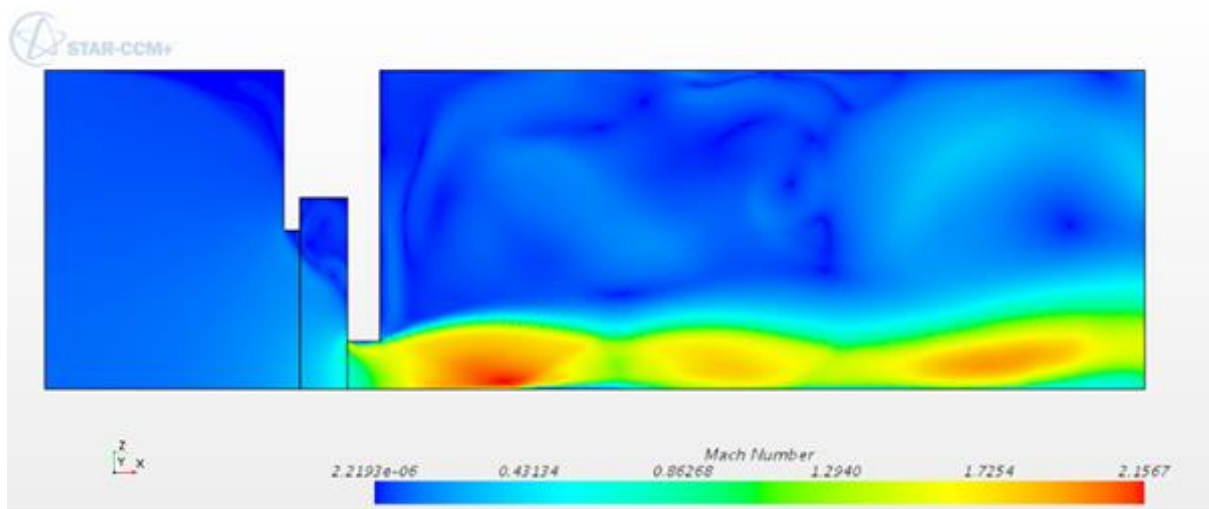


Figure 6.8 Brush seal enlarged section with Mach numbers

As for the labyrinth seal, the flow and Mach numbers suggest that the brush seal acts like a convergent-divergent nozzle, where the flow enters sub-sonic and exits super-sonic.

The brush seal has the same behaviour as the labyrinth seal, but with larger expansion waves that deplete over a longer distance. The larger waves is due to the larger leakage gap between the seal and the shaft. Figure 6.9 shows a comparison between the labyrinth and brush seal with the flow behaviour downstream of the seals on the shaft.

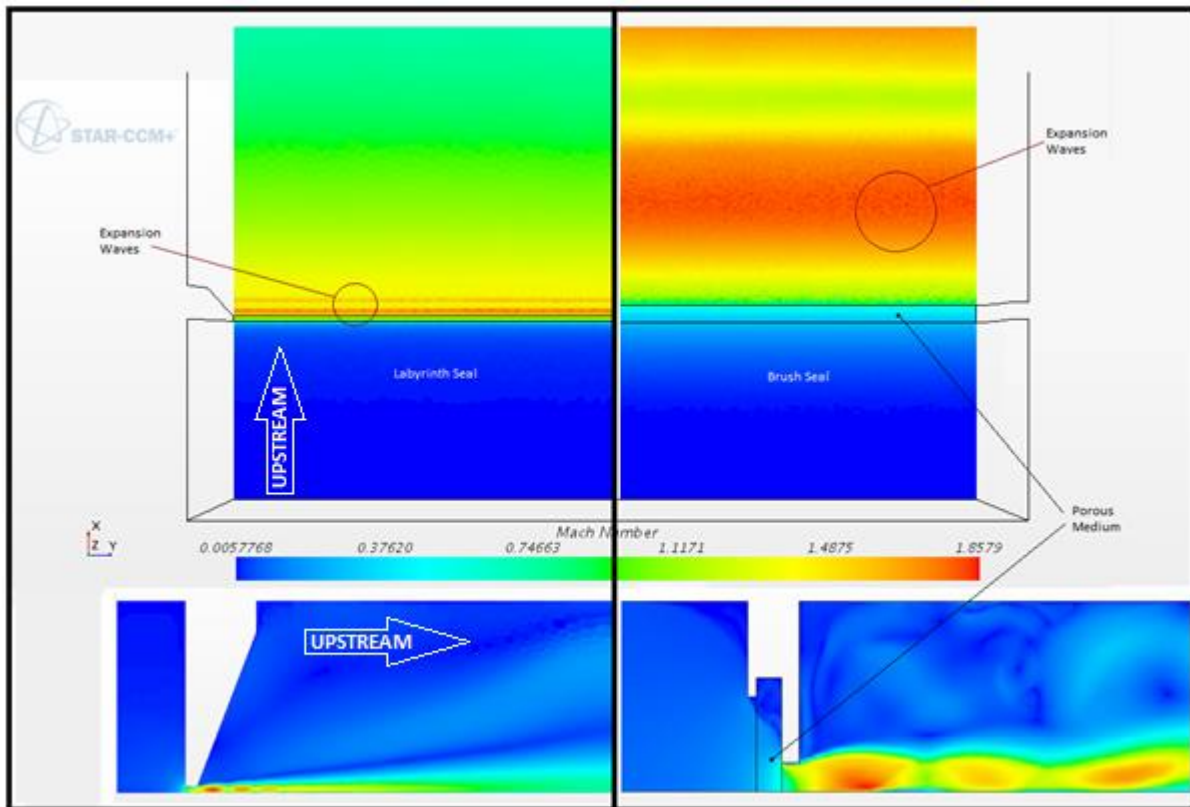


Figure 6.9 Seal comparison with flow behaviour on the shaft – side view and top view of section midway through gap

The labyrinth seal act like a nozzle-jet with the fluid being forced through the leakage gap with sharp expansion waves which deplete over short distance downstream of the seal. These waves do not move with the rotation of the shaft. The pressure drop over the shaft is the dominant force of leakage flow. The brush seal acts more like an orifice with large expansion waves which take a longer distance to deplete. Again the expansion waves do not rotate with the rotating shaft.

In STAR a velocity vector can be applied to each of the cells, which will indicate the direction with an arrow head and the magnitude on a colour scale. Figure 6.10 shows the velocity vectors for the worst leakage case of 5 bar upstream, with the maximum shaft speed of 10 000 rpm.

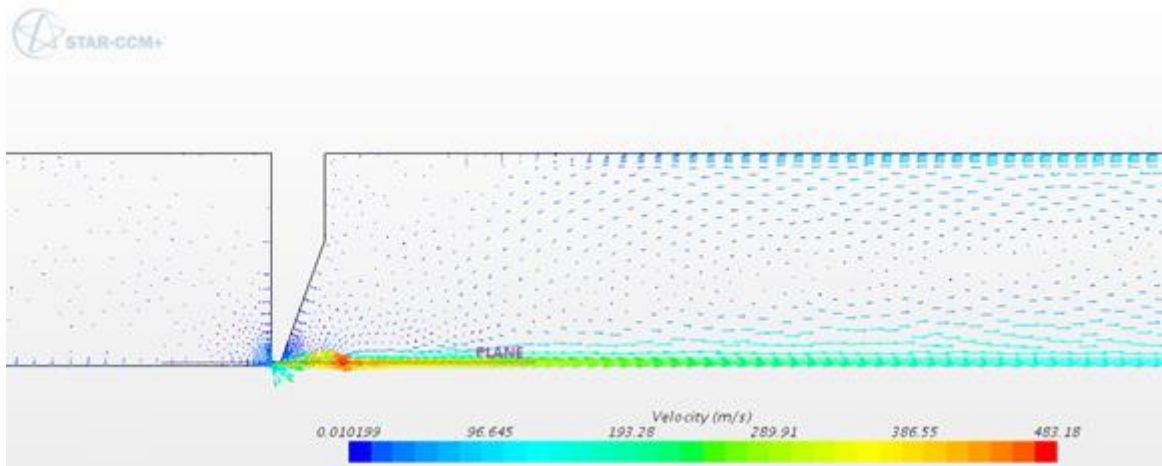


Figure 6.10 Labyrinth seal side view of velocity vectors

The throat of the seal is divided into three sections or cylinders around the axis. The first cylindrical section is located at quarter distance from the shaft in the leakage gap. The second is midway and the third is at a three-quarter distance from the shaft. Figure 6.11 shows the comparison between vectors on these different cylindrical planes on the same scale.

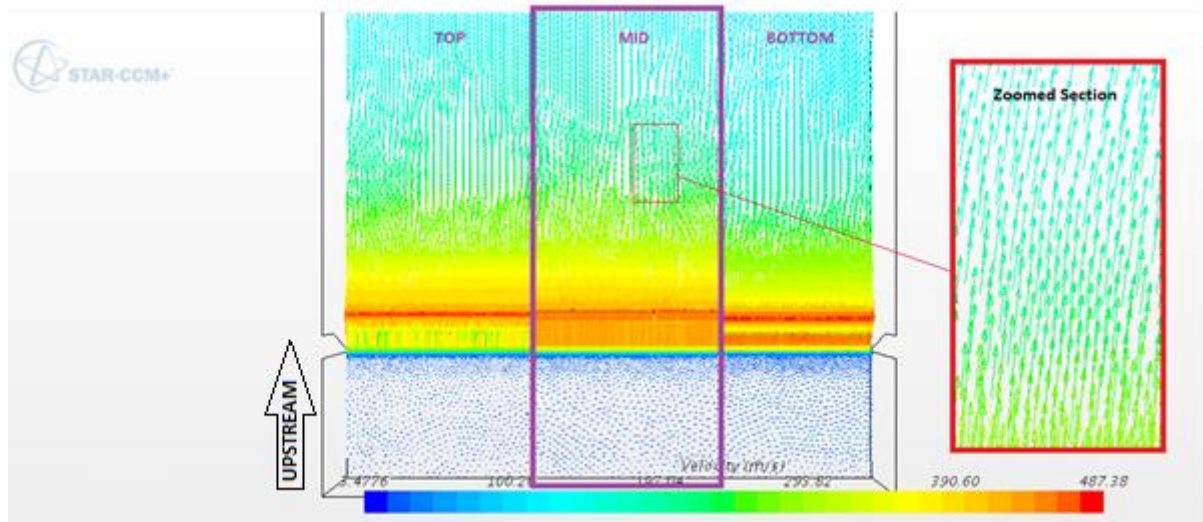


Figure 6.11. Labyrinth seal plane comparisons

The zoomed section shows how the fluid moves with the shaft rotation. It is clear that the shaft rotation has an influence on the fluid particles closer to it (bottom and mid) and less on those further away from the shaft. The flow rotates with the shaft as it moves away from the leakage gap.

Similar figures are now shown for the brush seal. Figure 6.12 shows the velocity vectors for the worst leakage case of 5 bar upstream, with the maximum shaft speed of 10 000 rpm.

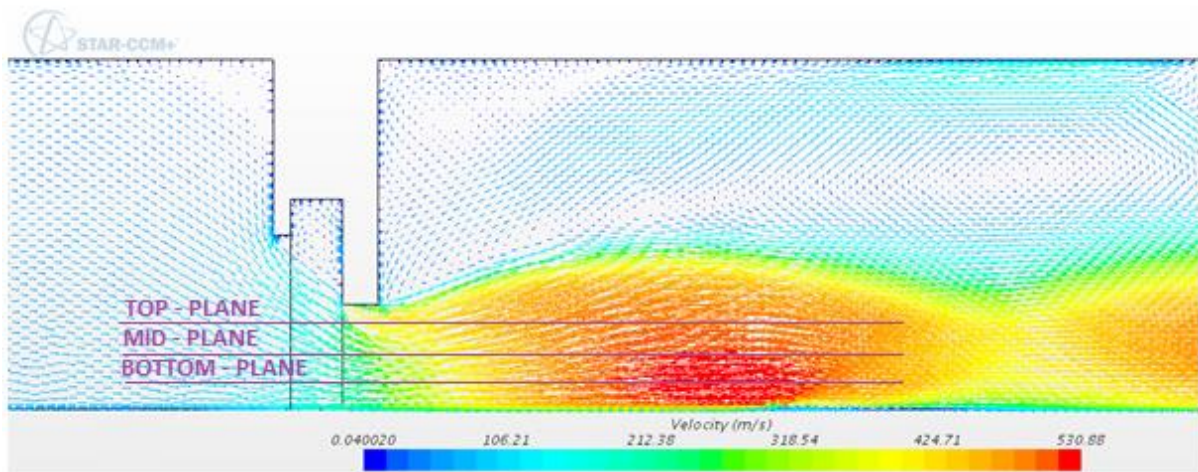


Figure 6.12. Brush seal side view of velocity vectors

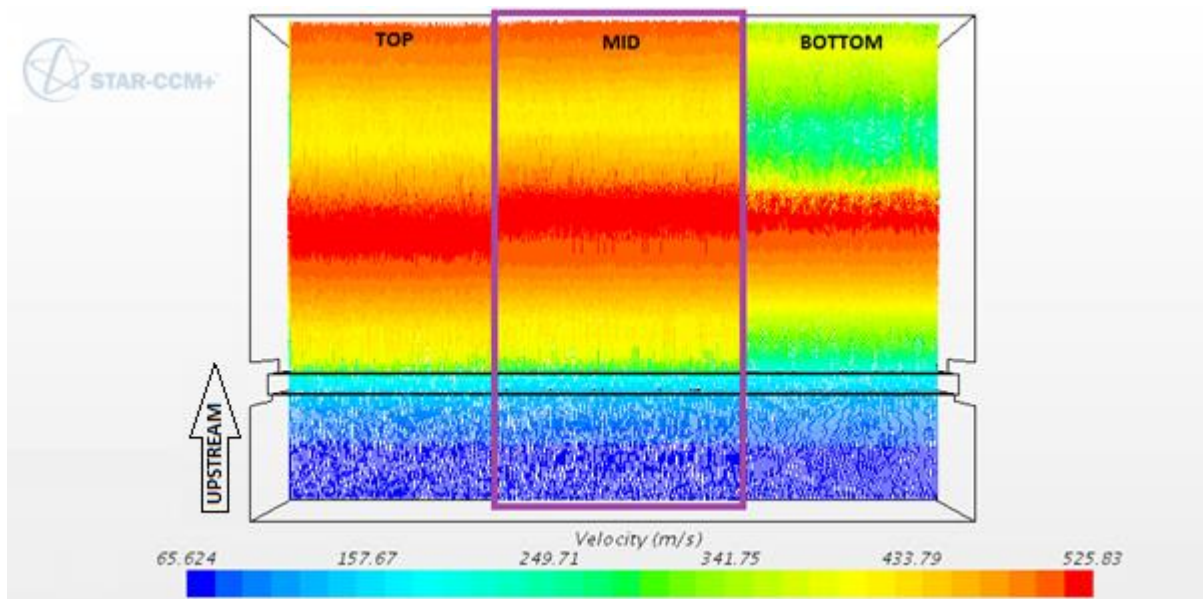


Figure 6.13. Brush seal plane comparisons

The comparison of the brush seal planes has the same trend as the labyrinth seal with the shaft rotation influencing the flow behaviour closer to the shaft. Brush has an effective gap larger than the labyrinth seal, the fluid in the gap is less affected by the shaft rotation. The porous medium account for most of the leakage restriction.

Figure 6.14 and 6.15 shows the various velocity components for the labyrinth and brush seals plotted on their respective mid-plane at 5 bar upstream and 10 000 rpm.

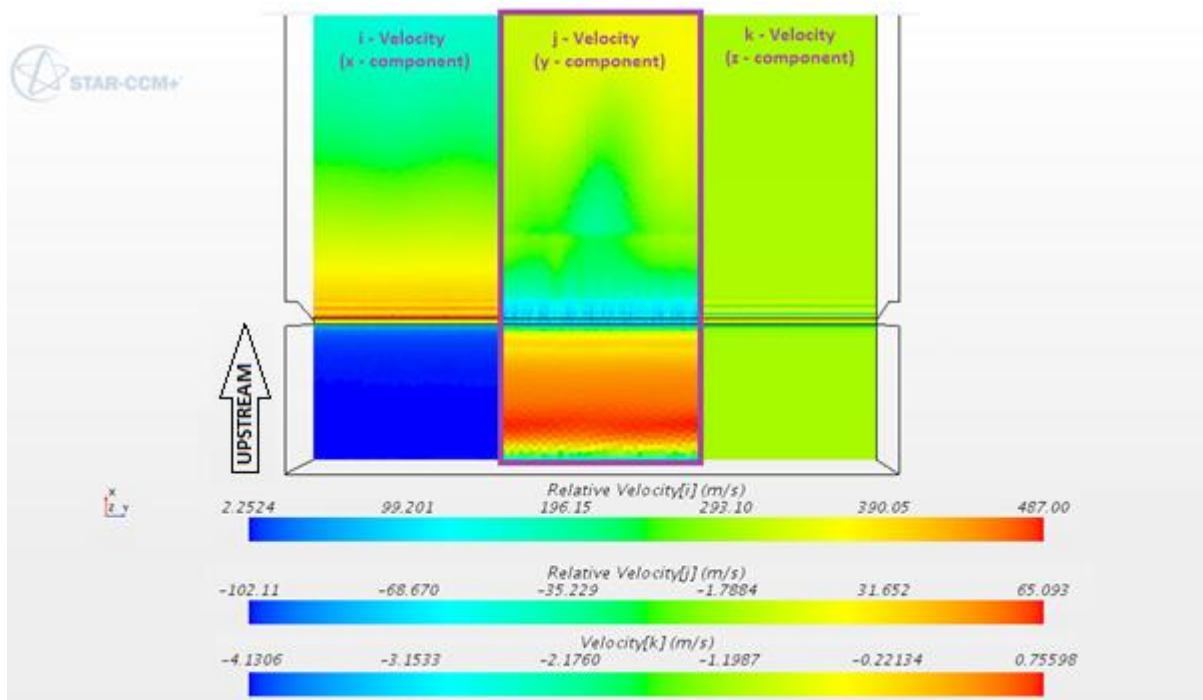


Figure 6.14. Velocity components for the Labyrinth seal on the mid-plane

It is clear in the magnitude of the various velocity components for the labyrinth seal that they do not contribute equally to the overall velocity magnitude. The z-component is very little affected throughout most of the plane. The x-component changes rapidly downstream of the leakage gap and this due to the choking upstream and rapid expansion downstream. The y-component show that upstream of the seal it is more affected by the shaft rotation since it has very similar velocity as the shaft rotation's linear velocity.

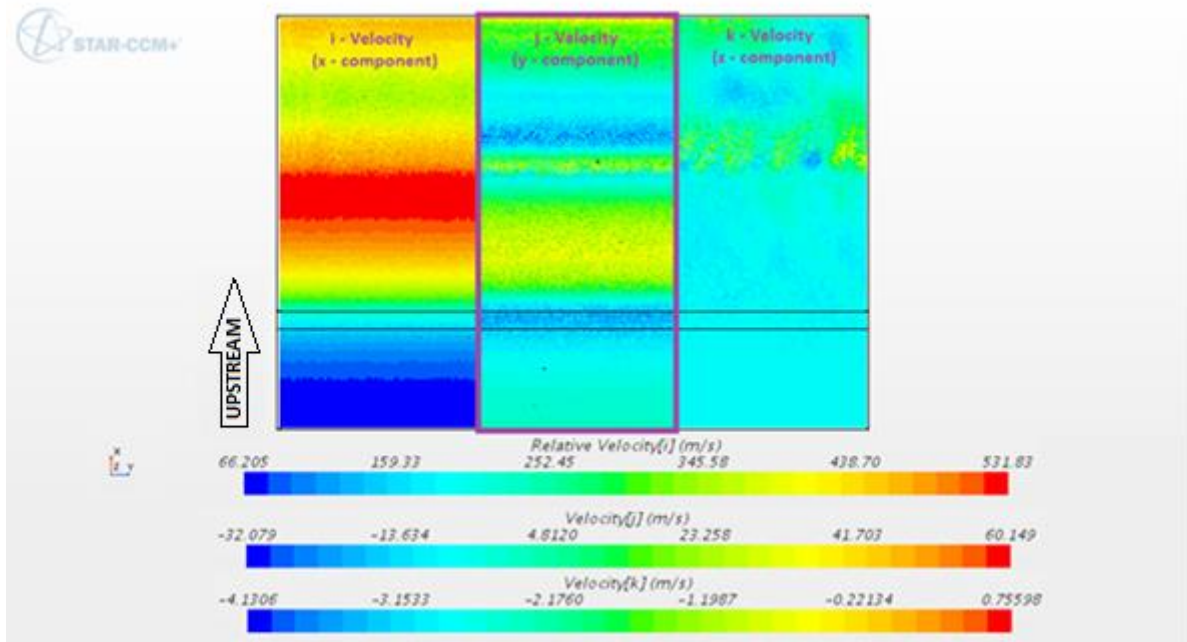


Figure 6.15. Velocity components for the Brush seal on the mid-plane

The brush seal pattern differs from the labyrinth seal. This is due to the position of the brush seals expansion wave on the mid-plane. The brush seal shows similar behaviour as the labyrinth seal. The z-component is mostly negative, which means it is moving toward the shaft surface. The x-component is again the largest and dominate component in the velocity magnitude.

Vorticity is known as the curl of a velocity field and is measure at the local rotation of the fluid. Therefore vorticity will indicate the circulation of a velocity field. Figures 6.16 and 6.17 shows the vorticity of the labyrinth and brush on their respective the mid-planes.

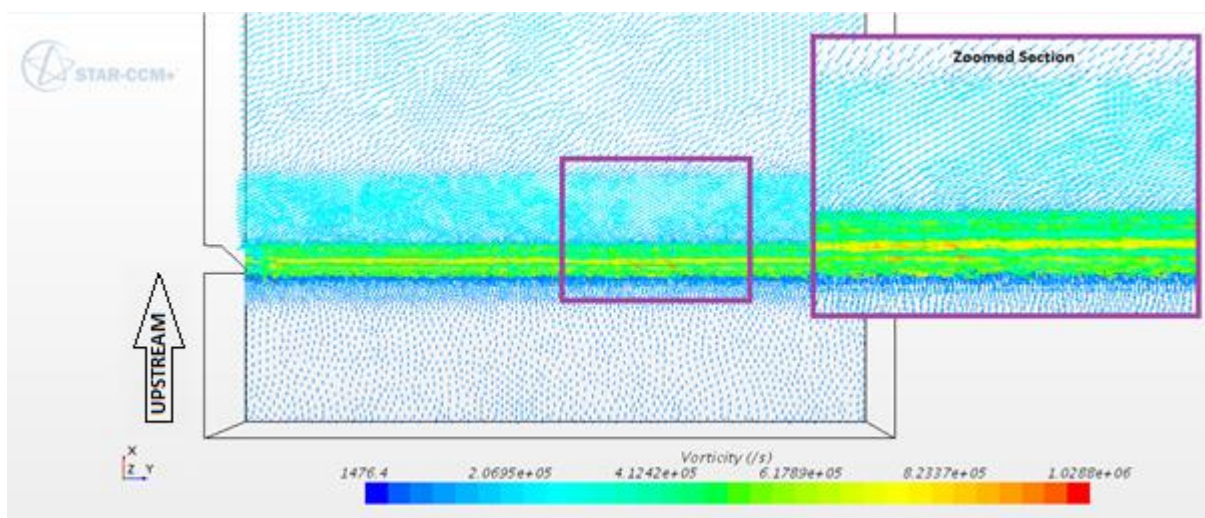


Figure 6.16. Vorticity vectors of the Labyrinth seal on the mid-plane

The vorticity shows that there is clear swirl around the shaft. The velocity field moves in the direction of the shaft rotation as well as the direction of the of the pressure difference over the seal. In the zoomed section the field seems to move parallel next to the leakage gap and at about a 45° angle a bit downstream of the leakage gap. This show that the flow is affected by shaft rotation.

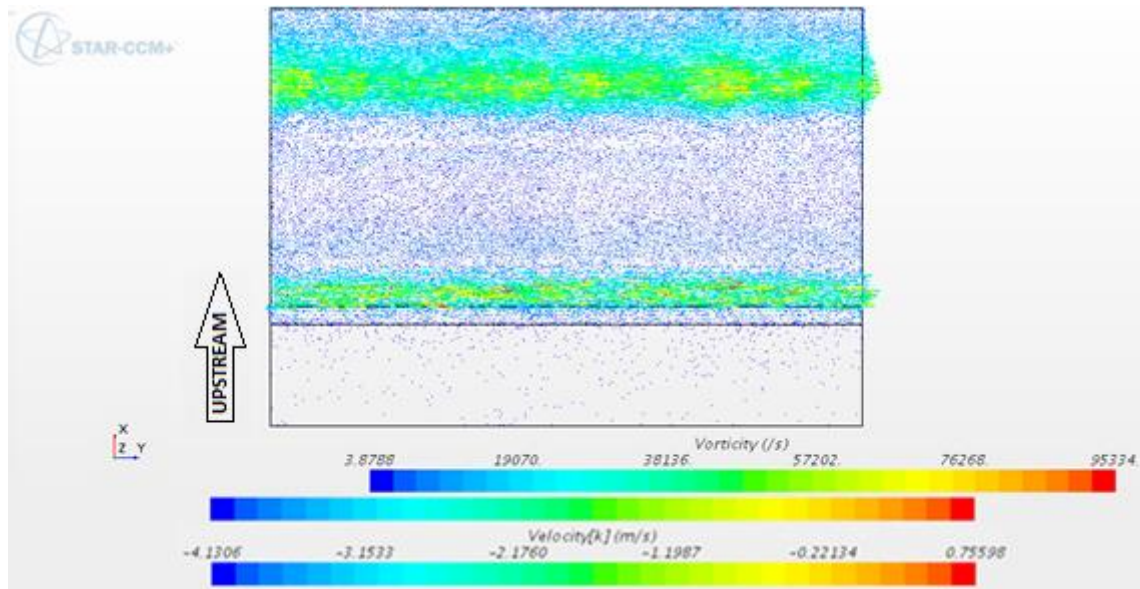


Figure 6.17. Vorticity of the Brush seal on the mid-plane

The brush seal again show a different pattern for the mid-plane. The vorticity show that the velocity field is affected by shaft rotation. The mid-plane of the brush seal is not affected to the same extend as the labyrinth's mid-plane due to the larger leakage gap which increases the plane distance from the shaft. The brush seal will have similar behaviour closer to the shaft surface.

6.2.3. Velocity triangles

As seen in the previous section the CFD simulations allow the velocity magnitude of the flow rate to be divided into an x-, y- and z-components. The components can be used to setup a graph to illustrate the effect that shaft rotation has on the leakage rate through the seal. Since the z-component magnitude has an order of 1E-16 it is neglected in the graph and therefore the 3D illustration can be simplified as a 2D graph made from the x- and y-components. With the x- and y- components the velocity magnitude can be illustrated as a vector.

The magnitude is calculated with Eq 6.3;

$$\dot{V}_{mag} = \sqrt{\dot{V}_x^2 + \dot{V}_y^2} \quad [\text{Eq 6.3}]$$

Figure 6.18 shows a schematic of how the velocity triangle is formed on the shaft.

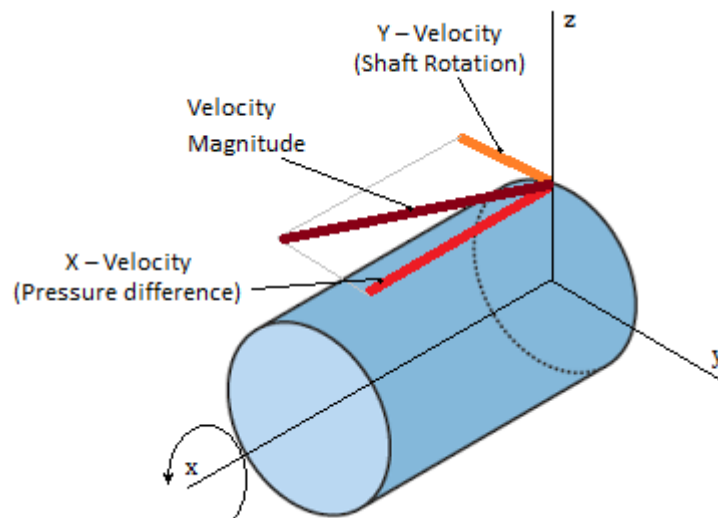


Figure 6.18 Schematic of the Velocity triangle on the shaft

In Figure 6.19 there are two axes and a diagonal line, the vertical axis has the x-component which represent the flow due to the pressure difference, horizontal axis has y-component which represent the effect of shaft rotation and the diagonal is the magnitude of the two components.

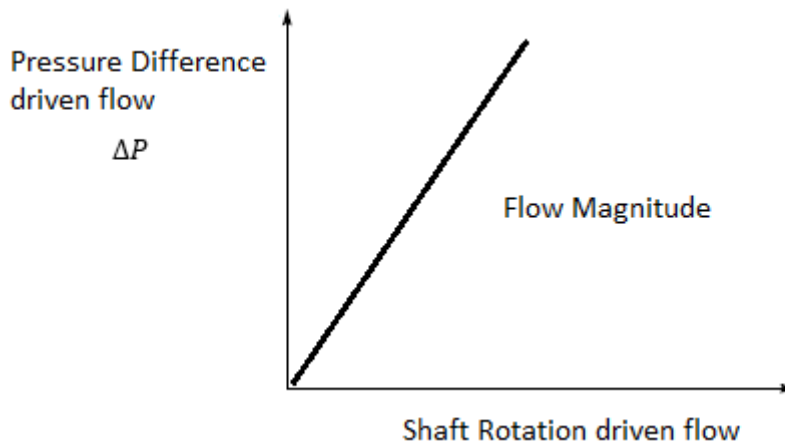


Figure 6.19 Schematic of flow velocity components

This type of 2D graph will help to explain why the leakage rate increases as the shaft speed increases.

Tables 6.6 and 6.7 and Figure 6.20 show how the velocity magnitude increases as the shaft speed increases. The 3000 rpm results are added as a midpoint between 1 000 rpm and 6 000 rpm results.

Table 6.6 Labyrinth seal leakage flow velocity components

Shaft speed [rpm]	X – Velocity [m/s] Pressure difference	Y – Velocity [m/s] Shaft Rotation	Velocity Magnitude [m/s]
0	5.29	0.0	5.29
1 000	5.29	0.03	5.29
3 000	5.29	0.16	5.30
6 000	5.29	0.44	5.31
10 000	5.29	0.96	5.38

Table 6.7 Brush seal leakage flow velocity triangle components

Shaft speed [rpm]	X – Velocity [m/s] Pressure difference	Y – Velocity [m/s] Shaft Rotation	Velocity Magnitude [m/s]
0	4.87	0.0	4.87
1 000	4.87	0.08	4.87
3 000	4.87	0.24	4.87
6 000	4.87	0.49	4.89
10 000	4.87	0.83	4.94

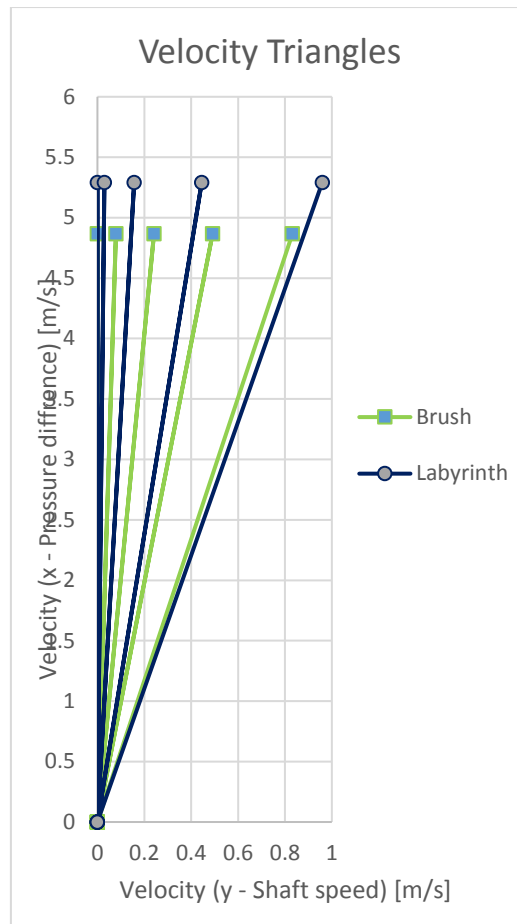


Figure 6.20 Velocity triangles of the labyrinth and brush seal

It was found that all the upstream pressures have similar mass flow velocities, and that it is the density of the fluid upstream which dictates the leakage rate through the seal. That is why only one set of velocities is shown, the full results are in **Appendix G**. It is clear that as the shaft speed increases, the speed of the surface opposing the seal also increases. As the surface speed increases so does the effect it has on the velocity y-component, which translate to an increase in velocity magnitude.

The increase of the z-component is due to the increase in surface speed and the centrifugal forces that create a suction that sucks the fluid through the seal and increases the flow rate. The y-component has just over an 18% increase in velocity relative to the x-component which translates into a 1.63% increase in velocity magnitude.

Results obtained revealed that the brush seal has the same behaviour as the labyrinth seal. When the surface speed increases as the shaft increases and this effect increases the leakage rate. The y-component has an about 17% increase in velocity relative to the x-component which translates into a 1.45% increase in velocity magnitude. The brush seal also has smaller velocity triangles which translate into lower leakage rates. In summary, the brush seal has superior performance over the labyrinth seal for the tested shaft speed and pressure ranges.

6.5. Seal Design guidelines

This section gives guidelines on things to look out for, which could assist in future seal design and research.

Draw the geometry of the seal as a 2D plane, since the seal has axial symmetric properties. This allows easier analysis of the seal. The non-contacting seal acts like a convergent-divergent nozzle, thus careful attention must be paid to the leakage gap of the seal. The seal can be simplified to a convergent-divergent nozzles due to its flow behaviour. The throat gap of the seal controls the fluid flow behaviour downstream.

The brush seal bristle pack can be simulated as a porous medium. The resistance of the bristle pack must be obtained experimentally. The thickness of the bristle pack correlates directly with the leakage rate of the seal. Therefore it is important to take note of it. The pressure range in which the seal operates must be verified with the resistance coefficients.

The various different seal can be simulated in CFD. The preferred mesh type for the simulations is Polynomial cells, since they have the highest accuracy of all the mesh types. A quarter model approach can be taken due to the axial-symmetric nature of the seals. Mesh independent study must be done to ensure that mesh independence is achieved.

The operating range must be determined. Selective parameters can be neglected if they fall within a specified range. For example for low speeds shaft rotation can be neglected.

6.6. Summary

This section summarises the main points of the labyrinth and brush seal analysis.

- Low shaft rotation speeds have little effect on the leakage rate of the non-contacting seals
- The effect of shaft rotation increases to the 3rd order on the leakage rate of the labyrinth and 2nd order for the brush seal as the shaft speed increases linearly.
- The shaft rotation creates a suction which sucks the fluid through the seal and increases the leakage rate
- These seals have similar behaviour as convergent-divergent nozzles.
- The shaft rotation causes the flow to swirl around the shaft.
- The brush seal has superior performance over the labyrinth seal for the tested shaft speed and pressure ranges.

Chapter 7 – Conclusion and Recommendations

7.1. Introduction

This chapter provides a summary of the important results that were discussed in previous chapters. From these results certain conclusions can be made which lead to recommendations for further research.

7.2. Summary

In Chapter 1, background information is given on the reasons why the study was being done. The problem statement with the relevant research goals are also given in the chapter. Emphasis is placed on the importance of understanding the leakage flow behaviour through a non-contacting seal.

In Chapter 2, a detailed literature study was conducted discussing the various types of seals available and research that has been conducted on them. It was found that in recent times experimental and numerical investigations were undertaken to analyse the effects of rotational speeds and pressure ratios on the leakage performance of labyrinth and brush seals for turbine applications. Different methods were used to evaluate the leakage in these seals. The leakage rates through the labyrinth and brush seals were measured using a rotating test rig. The leakage rate was also predicted using Reynolds-averaged Navier-Stokes (RANS) solutions coupling with the non-Darcian porous medium model for the brush seal. The resistance coefficients of the porous bristle pack were estimated and calibrated with experimental leakage values. The general conclusion is that shaft rotation has little effect on the leakage flow through these seals. The current study focused on the effect that shaft rotation has on the leakage performance of both labyrinth and brush seals. Both experimental and numerical methods are used to investigate these phenomena as were done by previous researchers. Different pressure ratios were considered as by Li et al. (2012) at various shaft speeds.

In Chapter 3 the experimental method was discussed. The dissertation makes use of two experimental setups, one for validation and the other used to simulate full size seals under operating conditions. The setups make use of high-pressure air with a range of 0 to 7 bar upstream and a rotating shaft with a range of 0 to 10 000 rpm to simulate the various conditions. The leakage flow is measured with an orifice designed with the ASME (1990) code. The uncertainty in the experimental data was calculated to be $\pm 4.7\%$.

In Chapter 4 the numerical method was discussed. The numerical method made use of commercial software to simulate the leakage flow through the non-contacting seals. The labyrinth seal was simulated as a 3D quarter model due to the axial symmetric nature of the geometry and the reduction in computational cost. The brush seal also used a 3D quarter model (for the same reasons as the labyrinth) with the brush bristles of the seal simulated as a porous medium. A porous medium was used due to the complexity of the brush bristles behaviour and shear number of entities required to simulate an actual brush's geometry accurately. The coefficients of resistance were obtained experimentally. The mesh independence study used the GCI method and showed that the refined mesh used in all the simulations are independent of the solutions. The GCI method shows that all the meshes have an asymptotic range of one. The solvers used were RANS for steady-state simulations with a $k-\omega$ turbulence solver active. The material properties are steady-state air with a reference pressure of 87 kPa.

In Chapter 5 a calibration exercise was conducted between the experimental and numerical method. The exercise showed that the two methods correlate well with percentage differences between the experimental and CFD simulations fully within the experimental uncertainty for all cases where the setup could supply sufficient air. It was found that experimental data started to deviate from the simulated CFD data above 5 bar upstream pressure for the largest tested nozzle-diameter due to the air supply limitations. This calibration exercise confirmed that the usable range of the setup is between 0 and 5 bar upstream pressure, regardless of flow rate.

In Chapter 6, the results of the experimental and numerical methods were discussed. The results were analysed to find the effect that shaft rotation has on the leakage rate. It was found that for both the labyrinth and brush the leakage rate increased as the shaft rotation speed increased. It was also found that the non-contacting seals behaviour were very similar to convergent-divergent nozzles and the shaft rotating also causes the flow to swirl around the shaft. A conclusion was drawn with seal design guidelines which could improve future seal design.

7.3. Conclusion

In this study the potential to develop an engineering tool for estimating the leakage rates through labyrinth and brush seal was investigated. The effect of shaft rotation on the leakage rates was the main parameter that was investigated. Numerical and experimental methods were used with good correlation obtained between the methods.

In the results it was found that low shaft rotation speeds have little effect on the leakage rate of the non-contacting seals. It was also found that the labyrinth seal leakage rate increases to a 3rd order polynomial as the shaft rotation speed increases linearly and the brush seal leakage rate increases to a 2nd order polynomial as the shaft rotation speed increases. The labyrinth seal leakage rate increased by about 1.6% from a stationary shaft to 10 000 rpm shaft speed, whereas the brush seal leakage rate only increased by about 1.4% for the same conditions. The shaft rotation may have greater effects on the leakage rate if the shaft speeds reach speed in excess of 15 000 rpm and higher. This knowledge may become useful for small turbine applications where the shaft rotation reaches speed of more than 100 000 rpm. Throughout the entire spectrum of upstream pressure and shaft speeds tested, the brush seal showed superior performance over the labyrinth seal.

The contributions to this field from this dissertation, was applying the behaviour of expansion wave found in nozzles to the same behaviour found in non-contacting seals. Another contribution was the quantification of the leakage flow behaviour in terms of polynomial equation for the various shafts speeds. It was also show that shaft rotation cause the velocity field to swirl around the shaft. Finally confirming the finding in known literature that shaft rotation has little contribution to the leakage rate in non-contacting seals and that brush seals have superior leakage performance to labyrinth seals.

The conclusion is that the research objectives were met. The methods that were developed show correlation between one and other. Extensive knowledge were gained in the field of non-contacting seals and their flow behaviour. The knowledge and methods can be used as an engineering design tool for more efficient seals and for future research on various effects of different seal parameters on flow behaviour through non-contacting seals.

7.4. Recommendations

In study there are some shortcomings which can be addressed in future work. The experimental setup can be upgraded to test a larger range of pressure drops and the setup must also be able to test different working fluids like steam and other gases.

Higher complex problems can also be addressed in future, for example the friction on the shaft of the brush seal, the behaviour of the stresses in the seals due to the high energy fluid's force acting on it. Other parameters like seal leakage gaps, brush bristle frictions, bristles density, temperature distribution and stage efficiency, etc. Also a detailed in-depth investigation of the behaviour of expansion waves in non-contacting seals using steam and other gasses

The numerical method developed in this dissertation can be used to simulate complex seal geometries and various combinations and layouts of these seal geometries, for example, testing multi-stage labyrinth, multi-stage brush seals, or combinations of the two and different fluids, and not just limited to air. For example Fluids like steam and pure oxygen can be simulated to determine their leakage and flow behaviour.

It is also recommended that the developed engineering tool is used to assist Eskom in improving their current non-contacting seal analysis. This will allow them to reduce leakage losses and improve reliability.

References

American Society of Mechanical Engineers, 1990, "Measurement of Fluid Flow in Pipes using Orifice, Nozzle and Venturi", ASME MFC-3M-1989.

ASME V&V 20 – 2009, 2009. Standard for Verification and Validation in Computational Fluid Dynamics and Heat Transfer, American Society of Mechanical Engineers, ISBN 9780791832097.

Ashton Z.S., 2009, "High Temperature Leakage Performance of a Hybrid Brush seal compared to a Standard Brush seal and Labyrinth seal", Mechanical Engineering Department, Texas A & M University.

Aviation.stackexchange, 2018, How is the central hub shaft casing of a two spool jet engine assembled [Online], <https://aviation.stackexchange.com/questions/27446/how-is-the-central-hub-shaft-casing-of-a-two-spool-jet-engine-assembled/27460>, Accessed 23 January 2018.

Bayley F. J., and Long C. A., 1993, "A Combined Experimental and Theoretical Study of Flow and Pressure Distributions in a Brush Seal," ASME J. Eng. Gas Turbines Power, 115(2), pp. 404–410.

Biester M.O., Mueller L., Seume J. R. and Guendogdu Y., 2011, "GT2011-45883 Time-Resolved Numerical Investigation of the Interaction of Labyrinth Seal Leakage and Main-Flow in a 1.5-Stage LP Turbine," Proceedings of the ASME Turbo Expo 2013, vol. 5, pp. 1623-1632.

Braun M. J., and Kudriavtsev V. V., 1995, "A Numerical Simulation of a Brush Seal Section and Some Experimental Results," ASME J. Turbomach., 117, pp. 190–202.

Carlile, J. A., Hendricks, R. C., and Yoder, D. A., 1993, "Brush Seal Leakage Performance with Gaseous Working Fluids at Static and Low Rotor Speed Conditions," ASME J. Eng. Gas Turbines Power, 115, pp. 397–403.

Chen L. H., Wood P. E., Jones T. V., and Chew J. W., 1999, "An Iterative CFD and Mechanical Brush Seal Model and Comparison With Experimental Results," ASME J. Eng. Gas Turbines Power, 121(4), pp. 656–662.

Chen L. H., Wood P. E., Jones T. V., and Chew J. W., 2000, "Detailed Experimental Studies of Flow in Large Scale Brush Seal Model and a Comparison With CFD Predictions," ASME J. Eng. Gas Turbines Power, 122, pp. 672–679.

Chew J. W., Lapworth B. L., and Millener P. J., 1995, "Mathematical Modeling of Brush Seals," Int. J. Heat Fluid Flow, 16(6), pp. 493–500.

Chew J. W., and Hogg S. I., 1997, "Porosity Modeling of Brush Seals," ASME J. Tribol., 119, pp. 769–775.

Choi D. C. and Rhode D. L., 2003, "Development of a 2-D CFD Approach for Computing 3D Honeycomb Labyrinth Leakage", ASME Paper GT2003-38238.

Chupp R. E. and Dowler C. A., 1991, "Performance Characteristics of Brush Seals for Limited Life Engines", 36th ASME Gas Turbine Conference, Orlando, Florida, paper no. 91-GT-281.

Chupp R. E., Hendricks R. C., Lattime S. B., and Steinetz B. M., 2006, "Sealing in Turbomachinery," J. Propul. Power, 22(2), pp. 313–349.

Cieśliewicz S.M., 2004, "CFD-Simulations for Advanced Turbomachinery Sealing Technologies: Brush Seals", Institute for Thermodynamics and Energy Conversion, University of Technology, Vienna

Cofer J.I. Reinker J.K. and Summer W.J., 1996, "Advances in Steam Path Technology", GE Power Generation, GER-3713E.

Denecke J., Farber K., Dullenkopf K. and Bauer H. J., 2005, Dimensional Analysis and Scaling of Rotating Seals, ASME Paper GT2005-68676.

Dogu Y., 2005, "Investigation of Brush Seal Flow Characteristics Using Bulk Porous Medium Approach," ASME J. Eng. Gas Turbines Power, 127, pp. 136–144.

Dogu Y., and Aksit, M. F., 2006, "Effects of Geometry on Brush Seal Pressure and Flow Fields—Part I: Front Plate Configurations," ASME J. Turbomach., 128(1), pp. 367–378.

Dogu Y., and Aksit, M. F., 2006, "Effects of Geometry on Brush Seal Pressure and Flow Fields—Part II: Backing Plate and Configurations," ASME J. Turbomach., 128(1), pp. 379–389.

Dogu Y., Akist M. F., Demiroglu M., and Dinc O. S., 2008, "Evaluation of Flow Behavior for Clearance Brush Seals," ASME J. Eng. Gas Turbines Power, 130, p. 012507.

Egli A., 1935, "Leakage of Steam through Labyrinth Seals", ASME Transactions FSP-57-5, pp. 115-122.

Ferguson J. G., 1988, "Brushes as High Performance Gas Turbine Seals," ASME Paper No. 88-GT-182.

Hiester P., 2013, "Computational Fluid Dynamic Simulation of a Straight Labyrinth Seal", Rensselaer Polytechnic Institute Hartford, Connecticut.

Kudriavtsev V. V., and Braun M. J., 1996, "Model Developments for the Brush Seal Numerical Simulation," J. Propul. Power, 12(1), pp. 193–201.

Li J., Kong S., Yan X., Obi S. and Feng Z., 2010, "Numerical Investigations on Leakage Performance of the Rotating Labyrinth Honeycomb Seal," Journal of Engineering for Gas Turbines and Power, vol. 132, no. 062501.

Li, J., Obi, S., and Feng, Z., 2009, "The Effects of Clearance Sizes on Labyrinth Brush Seal Leakage Performance Using a Reynolds-Averaged Navier-Stokes Solver and Non-Darcian Porous Medium Model," Proc. Inst. Mech. Eng., Part A, 223, pp. 953–964.

Li J., Qiu B., and Feng Z., 2012, "Experimental and Numerical Investigations on the Leakage Flow Characteristics of the Labyrinth Brush Seal", Journal of Engineering for Gas Turbines and Power, Vol. 134 102509-1

Li J., Yan X., Li G. and Feng Z., 2007, "Effects of Pressure Ratio and Sealing Clearance on Leakage Flow Characteristics in Rotating Honeycomb Labyrinth Seal", ASME Paper GT2007-27740.

Martin H.M., 1908, "Labyrinth Packing", Merriam-Webster Collegiate Dictionary, Engineering 85, pp.35-38.

Massini D., Facchini B., Miccio M., Bianchini C., Ceccherini A. and Innocenti L., 2014, "Analysis of flat plate honeycomb seals aerodynamic losses: effects of clearance", 68th CITMEA, p. 502.

Mendonca, F., Read, A., Caro, S., Debatin, K. and Caruelle, B., 2005, "Aeroacoustic Simulation of Double Diaphragm Orifices in an Aircraft Climate Cooling System". AIAA-2005-2976.

Pugachev A. O., and Helm P., 2009, "Calibration of Porous Medium Models for Brush Seals," Proc. Inst. Mech. Eng., Part A, 223, pp. 83–91.

Roache, P.J., 1998. Verification and Validation in Computational Science and Engineering, Hermosa Publishers, Albuquerque, New Mexico.

Rohan J.D., Dara W.C. and Leland T.J., 2002, "A Comparison of Rotordynamic-Coefficient Predictions for Annular Honeycomb Gas Seals Using Three Different Friction-Factor Models", ASME J. of Tribology.

Schramm V., Willenborg K., Kim S. and Wittig S., 2002, "Influence of a Honeycomb Facing on the Flow Through a Stepped Labyrinth Seal," Journal of Engineering for Gas Turbines and Power, vol. 124, pp. 140-146.

Energy.Siemens, 2018, Steam Turbines Technical Papers [Online], <https://www.energy.siemens.com/hq/en/energy-topics/publications/brush-seals/technical-papers/steam-turbines.htm>, Accessed 23 January 2018.

Soemarwoto B. I., Kok J. C., de Cock K. M. J., Kloosterman A. B. and Kool G. A., 2007, "Performance Evaluation of Gas Turbine Labyrinth Seals Using Computational Fluid Dynamics", ASME Paper GT2007-27905.

STAR-CCM+ Version 10.06.010, 2014, "User Guide and Methodology Manuals", CDadapco, London, UK.

Takenaga H., Matsuda T. and Yokota H., 1998, Proc. 8 th Int. Symposium on Flow Visualization Sorrento, Italy, Paper No 33.

Turner M. T., Chew J. W., and Long C. A., 1998, "Experimental Investigation and Mathematical Modeling of Clearance Brush Seals," ASME J. Eng. Gas Turbines Power, 120, pp. 573–579.

Vakili A. D., Meganathan A. J., Michaud M. and Radhakrishnan S., 2005, "An Experimental and Numerical Study of Labyrinth Seal Flow", ASME Paper GT2005-68224.

Vermes G., 1961, "A Fluid Mechanics Approach to the Labyrinth Seal Leakage Problem", ASME J. Eng. Power, pp. 161-169.

Whalen J.K. and Alvarez E., 2004, "Thermoplastic Labyrinth Seals for Centrifugal Compressors", 33rd Turbomachinery Symposium, Mechanical Engineering Department, Texas A & M University.

Yan, X., Li, J., Song, L., and Feng, Z., 2009, "Investigations on the Discharge and Total Temperature Increase Characteristics of the Labyrinth Seals With Honeycomb and Smooth Lands". Journal of Turbomachinery 131 (2009) 041009: 1-8.

Yan, X., Feng Z., and Feng Z., 2010, "Effect of Inlet Preswirl and Cell Diameter and Depth on Honeycomb Seal Characteristics" Journal of Engineering for Gas Turbine and Power 132 (2010) 122506: 1-13.

Zucrow M.J. and Hoffman J.D., 1976, "*Gas Dynamics Volume 1*", Wiley, New York

Appendices

List of all Appendices:

Appendices.....	70
Appendix A – Orifice Design.....	71
Appendix B – Matlab codes for Test setups calculation	80
Appendix C – Calibration Certificate	83
Appendix D – Uncertainty in Experimental Data	92
Appendix E – Coefficients of Resistance	97
Appendix F – Labyrinth seal leakage area.....	102
Appendix G – Mesh independence study	103
Appendix H – Labyrinth Seal Results.....	106
Appendix I – Brush seal Results	108
Appendix J – Calibration Exercise Results.....	110
Appendix K - Sample Conversions.....	112

Appendix A – Orifice Design

The design of the orifice and its calculations are discussed in this section. Section 7 in the ASME code (ASME, *Measurement of Fluid Flow in Pipes using Orifice, Nozzle and Venturi*, 1990) describes the physical characteristics of the orifice plate as well as that of the pressure taps to be used in the flow meter. An axial plane cross section of a standard orifice plate is shown in Figure A.1.

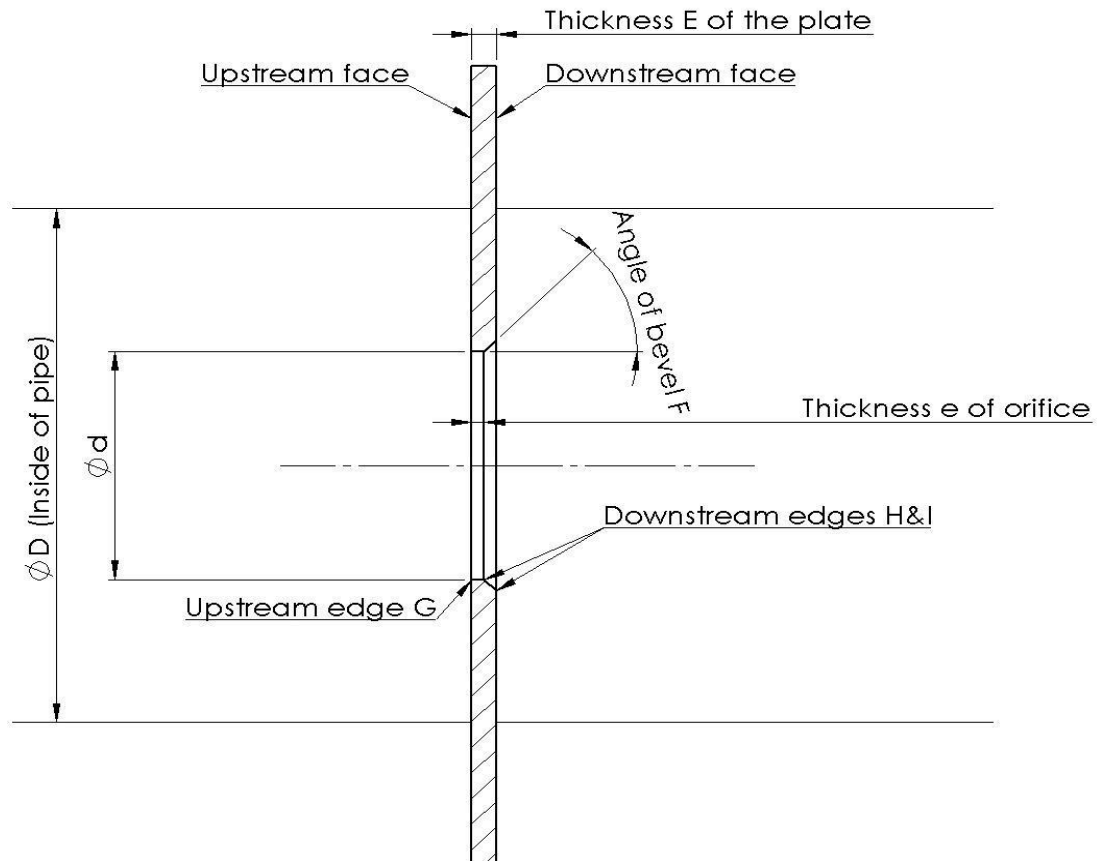


Figure A.1 Axial cross section of a basic Orifice (ASME, 1990)

Using these guidelines with a pipe diameter of $D=57.1\text{mm}$ (inner diameter), the dimensions of the orifice are as follows:

- Orifice plate thickness, E :

Table 3 [p24] of ASME (1990) gives the Minimum plate thickness $E_{\text{min}}=3\text{mm}$ for pipes with D from 50mm to 150mm. The Maximum plate thickness, $E_{\text{max}} = 1.5 \times E_{\text{min}} = 4.5\text{mm}$. The plate thickness, measured at any point, may not vary by more than $0.001D$.

- The upstream and downstream faces A & B:

Both faces must be flat. Face A may have a maximum roughness of $1.3\mu\text{m}$ and will have a circle larger than the internal diameter of the pipe. The roughness of face B may be judged by visual inspection.

- Diameter of Orifice, d :

The value of β must always be $0.2 < \beta < 0.7$ and is determined by the following ratio:

$$\beta = \frac{d}{D}$$

Thus:

$$\frac{d_{min}}{57.1} > 0.2$$

$$\frac{d_{max}}{57.1} < 0.7$$

$$d_{min} = 11.42 \text{ mm}$$

$$d_{max} = 39.97 \text{ mm}$$

- The minimum edge thickness, e :

$$e > 0.1d$$

Thus:

$$1 > e > 3.5\text{mm}$$

- Angle of bevel, $F = 45^\circ$.

- Edges G, H and I:

G must be sharp. The radius of G must be less than H and I must be sharp by visual inspection only.

- The orifice must be cylindrical and perpendicular to the upstream face.
- Maximum diameter of pressure tap holes from Table 4 [p. 25] of ASME (1990):
For $D = 50\text{mm}$; Tap holes = 10mm and 1 hole on each side of orifice.
- Minimum Pressure tap hole diameter decrease distance:
 $2.5 (\text{Tap diameter}) = 2.5(10) = 25\text{mm}$.
Thus the Pressure tap hole diameter may decrease at 25mm away from the pipe inner wall.
- Spacing of Pressure Taps, l_1 & l_2 is shown in Figure A.2.

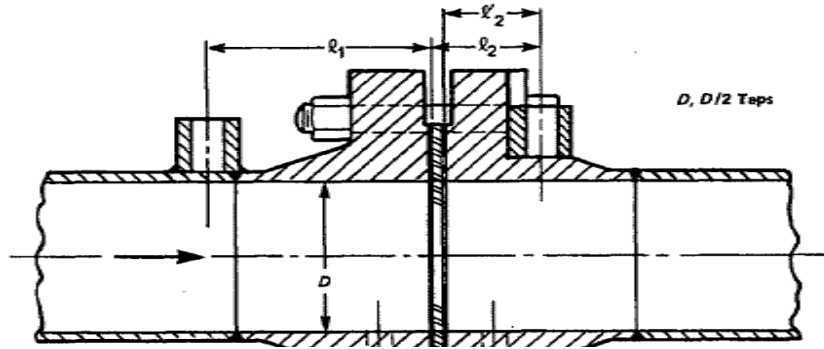


Figure A.2 Spacing of pressure taps diagram (AMSE, 1990)

Upstream spacing, $l_1 = D \pm 5.0 \%$;

$$54.25 \text{ mm} > l_1 > 59.96 \text{ mm}$$

Downstream spacing, $l_2 = 0.5D \pm 1 \text{ mm}$;

$$27.55 \text{ mm} > l_2 > 29.55 \text{ mm}$$

A.1. Isentropic flow analysis to determine Orifice size.

ASME (1990) gives the specifics of how the Orifice must be designed. The isentropic flow analysis (Zucrow & Hoffman 1976, pp. 136-140) is used to determine the appropriate orifice size for this study.

$$P_{atm} = 87 \text{ kPa}$$

$$T_0 = 293.15 \text{ K}$$

$$M_{mass} = 28 \text{ kg/kmol}$$

$$R_u = 8314 \text{ J/kmol.K}$$

$$\gamma = 1.4$$

$$\text{Area of the seal gap, } A_{leakage} = 0.113 \times 10^{-3} \text{ m}^2$$

$$\text{Area of the 57.1 mm pipe, } A_{pipe} = 2.56 \times 10^{-3} \text{ m}^2$$

Sample Calculations (From Tables C.6 [p. 709] and C.7 [p. 720] of Zucrow & Hoffman (1976)) with 1 bar upstream;

$$P_0 = 100 \text{ kPa}$$

$$\frac{P}{P_0} = 0.87 \quad M = 0.45 \quad \frac{\rho}{\rho_0} = 0.90551 \quad \frac{t}{t_0} = 0.8915$$

Upstream density, ρ_0 :

$$\rho_0 = \frac{P_0 M_{mass}}{R_u T_0}$$

$$\rho_0 = \frac{100 \times 10^3 (28)}{8314 (293.15)}$$

$$\rho_0 = 1.14884 \text{ kg/m}^3$$

Density in the seal, ρ :

$$\rho = \frac{\rho}{\rho_0}(\rho_0)$$

$$\rho = 0.90551(1.14884) = 1.0403 \text{ kg/m}^3$$

Temperature in seal, t :

$$t = \frac{t}{T_0}(T_0)$$

$$t = 0.96108(293.15) = 281.74 \text{ K}$$

Speed of sound, c at t :

$$c = \sqrt{\frac{\gamma R t}{M_{mass}}}$$

$$c = \sqrt{\frac{1.4(8314)(281.74)}{28}}$$

$$c = 342.23 \text{ m/s}$$

Air velocity in seal, v :

$$v = M c$$

$$v = 0.45(342.23)$$

$$v = 154 \text{ m/s}$$

Mass flow rate in seal, \dot{m} :

$$\dot{m} = \rho A_{seal} v$$

$$\dot{m} = 1.0403(0.113 \times 10^{-3})(154)$$

$$\dot{m} = 18.10 \times 10^{-3} \text{ kg/s}$$

Air velocity in upstream pipe, v_0 :

$$v_0 = \frac{\dot{m}}{\rho_0 A_{pipe}}$$

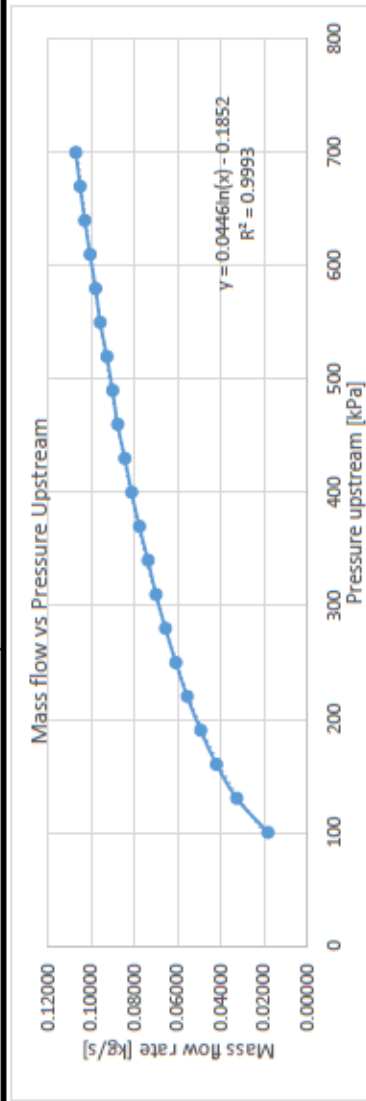
$$v_0 = \frac{18.10 \times 10^{-3}}{1.14884(2.56 \times 10^{-3})}$$

$$v_0 = 6.15 \text{ m/s}$$

The sample calculation is repeated for the entire pressure range of the compressed air supply which is 0 to 7 bar. The calculation starts at 1 bar with 0.3 bar increments all the way up to 7 bar. The results are given in Table A.1.

Table A.1: Calculation results for all P_0

P	P_0	P/P_0	M	t/T_0	ρ/ρ_0	ρ_0	β	t	c	v	\dot{m}	v_0
87	100	0.87	0.45	0.96108	0.9094	1.148836	1.044752	281.7406	342.2274	154.0023	0.01822609	6.195457
87	130	0.669231	0.78	0.89152	0.75046	1.493487	1.120802	261.3491	329.6101	257.0959	0.03264205	8.535202
87	160	0.54375	0.98	0.83887	0.64452	1.838138	1.184717	245.9147	319.7292	313.3346	0.04205098	8.933794
87	190	0.457895	1.12	0.79914	0.57143	2.182789	1.247311	234.2679	312.066	349.5139	0.04938470	8.835245
87	220	0.395455	1.23	0.76771	0.5164	2.52744	1.30517	225.0542	305.8677	376.2172	0.05562358	8.59441
87	250	0.348	1.33	0.73867	0.46895	2.872091	1.346867	216.5411	300.0269	399.0358	0.06088212	8.278078
87	280	0.310714	1.41	0.7155	0.43304	3.216741	1.392978	209.7488	295.2839	416.3503	0.06569863	7.97587
87	310	0.280645	1.48	0.69537	0.40322	3.561392	1.436025	203.8477	291.1005	430.8287	0.07008414	7.684894
87	340	0.255882	1.55	0.67545	0.37495	3.906043	1.464571	198.0082	286.9007	444.696	0.07377800	7.376117
87	370	0.235135	1.6	0.66138	0.35573	4.250694	1.512099	193.8835	283.8968	454.2349	0.07780617	7.148125
87	400	0.2175	1.65	0.64746	0.33731	4.595345	1.550056	189.8029	280.8933	463.474	0.08138155	6.915853
87	430	0.202326	1.7	0.63371	0.31969	4.939996	1.579267	185.7721	277.8947	472.421	0.08451582	6.681121
87	460	0.18913	1.74	0.62285	0.30617	5.284647	1.618	182.5885	275.5032	479.3756	0.08786335	6.492766
87	490	0.177551	1.79	0.60945	0.28997	5.629297	1.632327	178.6603	272.5235	487.8171	0.09020228	6.257506
87	520	0.167308	1.83	0.59888	0.27756	5.973948	1.658129	175.5617	270.1499	494.3744	0.09285975	6.070214
87	550	0.158182	1.86	0.59104	0.26857	6.318599	1.696986	173.2634	268.3758	499.179	0.09595948	5.930687
87	580	0.15	1.9	0.58072	0.25699	6.66325	1.712389	170.2381	266.0225	505.4427	0.09804547	5.746181
87	610	0.142623	1.93	0.57307	0.24861	7.007901	1.742234	167.9955	264.2645	510.0305	0.10065976	5.609264
87	640	0.135938	1.96	0.56551	0.24049	7.352552	1.768215	165.7793	262.5156	514.5306	0.10306223	5.473931
87	670	0.129851	1.99	0.55803	0.23262	7.697203	1.790523	163.5865	260.7737	518.9396	0.10525677	5.340169
87	700	0.124286	2.02	0.55064	0.22499	8.041853	1.809337	161.4201	259.0412	523.2632	0.10724889	5.208043



T_0 293.15
 $M_{(mass)}$ 28
 R 8314
 Y 1.4
 Aleslage 0.0001133
 Apipe 0.0025607

A.2. Isentropic flow analysis of the Orifice to verify the Orifice size.

From the data in Table A.1 performance curves were drawn to determine the orifice size. Figure A.3 shows velocity versus upstream pressure and Figure A.4 shows velocity versus pressure ratio.

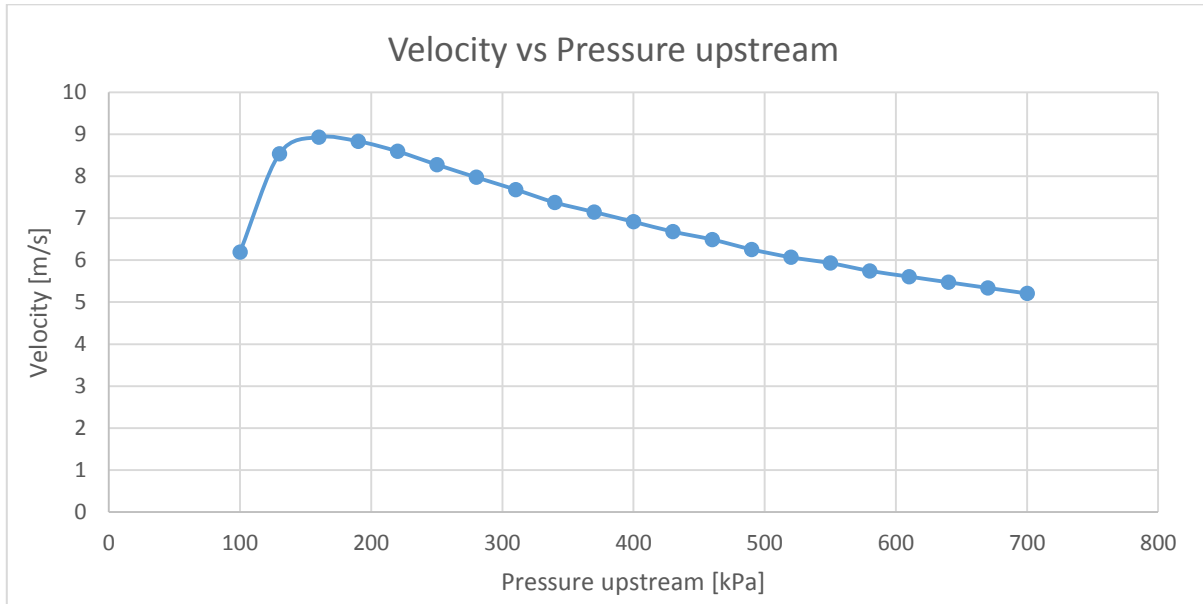


Figure A.3 Orifice design performance curve for velocity vs pressure upstream

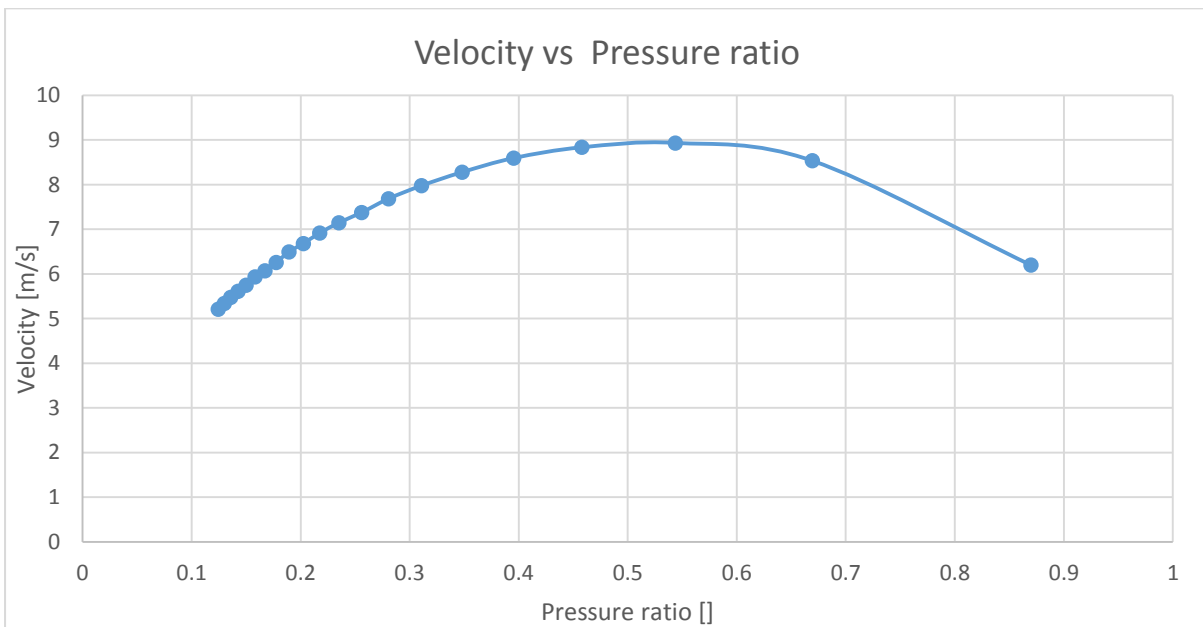


Figure A.4 Orifice design performance curve for velocity vs pressure ratio

By using the velocity-pressure ratio performance curve, a curve can be set up to show orifice sizes against different pressure ratios as in Figure A.5.

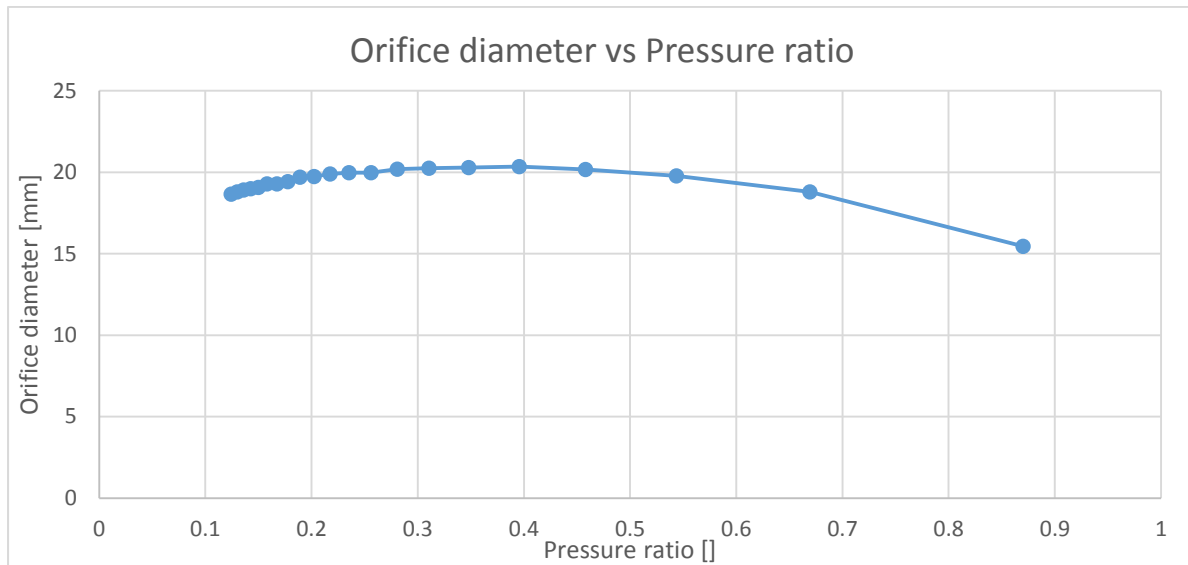


Figure A.5 Orifice diameters for different pressure ratios

The minimum and maximum sizes for the orifice were obtained from the orifice diameter against pressure ratio, and the diameter sizes are;

$$15.46 \text{ mm} < d_{orifice} < 20.35 \text{ mm}$$

Both these diameters fall within the maximum and minimum orifice diameter set out by ASME (1990) which are;

$$d_{min} = 11.42 \text{ mm} \quad d_{max} = 39.97 \text{ mm}$$

After the flow properties with upstream pipe and orifice size have been estimated, isentropic flow analysis (Zucrow & Hoffman 1976, pp. 189-204) is used to verify orifice size. Values from Table A.1 were used for the inlet and outlet pressures P_0 and P_2 , respectively, at the orifice.

$$T_0 = 293.15 \text{ K}$$

$$M_{mass} = 28 \text{ kg/kmol}$$

$$R_u = 8314 \text{ J/kmol.K}$$

$$\gamma = 1.4$$

$$\text{Area of the 57.1 mm pipe, } A_{pipe} = 2.56 \times 10^{-3} \text{ m}^2$$

Isentropic flow (From Tables C.6 [p. 709] and C.7 [p. 720] of Zucrow & Hoffman (1976)) with 2 bar upstream, $P_2 = 200 \text{ kPa}$:

$$\frac{P}{P_0} = 0.75 \quad M = 0.65 \quad \frac{\rho}{\rho_0} = 0.8164 \quad \frac{t}{t_0} = 0.9221$$

Upstream pressure of orifice, P_0 :

$$P_0 = \frac{P_2}{P_2/P_0}$$
$$P_0 = \frac{200}{0.75} = 266.67 \text{ kPa}$$

Upstream density, ρ_0 :

$$\rho_0 = \frac{P_0 M_{mass}}{RT_0}$$
$$\rho_0 = \frac{266.67(1000)(28)}{8314(293.15)}$$
$$\rho_0 = 3.064 \text{ kg/m}^3$$

Density in the seal, ρ :

$$\rho = \frac{p}{\rho_0}(\rho_0)$$
$$\rho = 0.8164(3.064) = 2.501 \text{ kg/m}^3$$

Temperature in seal, t :

$$t = \frac{t}{T_0}(T_0)$$
$$t = 0.9221(293.15) = 270.31 \text{ K}$$

Speed of sound, c at t :

$$c = \sqrt{\frac{\gamma R_u t}{M_{mass}}}$$
$$c = \sqrt{\frac{1.4(8314)(270.31)}{28}}$$
$$c = 335.22 \text{ m/s}$$

Air velocity in seal, v :

$$v = Mc$$
$$v = 0.65(335.22)$$
$$v = 217.89 \text{ m/s}$$

Mass flow rate in seal, \dot{m} :

$$\dot{m} = \dot{m}_{seal} = \dot{m}_{system} = 0.161 \text{ kg/m}^3$$

Area of orifice, $A_{orifice}$:

$$A_{orifice} = \frac{\dot{m}}{\rho v}$$

$$A_{orifice} = \frac{0.161}{2.501(217.89)}$$

$$A_{orifice} = 295.44 \times 10^{-6} \text{ m}^2$$

Diameter of orifice, d :

$$d = \sqrt{\frac{4A_{orifice}}{\pi}}$$

$$d = \sqrt{\frac{4(295.44 \times 10^{-6})}{\pi}}$$

$$d = 19.395 \text{ mm}$$

According to the results found earlier in Appendix A, an orifice with $d = 19.4$ mm will be sufficient for the experimental setup.

Appendix B – Matlab codes for Test setups calculation

B.1. Matlab code for Orifice Flow rate calculation

```
1 % Fourie Wiid (21-02-2017)
2 % Compressible flow in ASME Orifice
3 clear all; clc
4
5 D = 0.0571; %diameter of Pipe upstream [m]
6 d = 0.0194; %diameter of orifice [m]
7 B = d/D; %diameter ratio of orifice diameter to pipe diameter [dimensionless]
8
9 k = 1.4; %isentropic exponent
10 R = 0.287; %Specific gas constant [kJ/(kg·K)]
11
12 P1 = [0.1, 100, 200, 300, 400, 500]; %Pressure upstream [kPa]
13 P2 = [0.1, 85, 175, 270, 355, 430]; %Pressure downstream [kPa]
14 T1 = 15 + 273.15; %Temperature upstream [K]
15
16 dp = P1-P2; %Pressure drop over orifice [kPa]
17
18 rho1 = P1./(T1*R); %Density of fluid upstream [kg/m^3]
19
20 % e1 - expansion coefficient
21 e1 = 1 - (0.351 + 0.256*B^4 + 0.93*B^8)*(1-(P2./P1).^(1/k));
22
23 % Cd - discharge coefficient
24 Cd = 0.6; % discharge coefficient // C = 0.60 may be taken as standard,
25 % but the value varies noticeably at low values of the Reynolds number.
26
27 % Reader-Harris/Gallagher equation with discharge coefficient
28 % qm - mass flow [kg/s]
29 % qm = (Cd/(sqrt(1-B^4)))*(pi/4)*(d^2)*e1.*(sqrt(2*dp.*rho1))
30 A = (Cd/(sqrt(1-B^4)))*(pi/4)*(d^2);
31 B = (sqrt(2*dp.*rho1));
32 qm = A*e1.*B;
33
34 % u - dynamic viscosity [Pa.s] //Viscosity is independent of pressure
35 % and Viscosity increases as temperature increases
36 % Calc u with Sutherland formula
37 T0 = 291.15; %Reference Temp at 291.15 K
38 u0 = 1.827*10^(-5); %Reference viscosity at Ref temp
39 Cs = 120; %Sutherland constant for air
40 u = u0*((T0+Cs)/(T1+Cs))*(T1/T0)^1.5;
41
42 Re = (4*qm)/(pi*u*D); %Reynolds number
43
44 % Calculating Flow with Reynolds in Cd
45 err = 1;
46 i = 0;
47 while err > 1e-12 %for i = 1:1:10% Cd1 = Cd;
48 Cd = 0.5959 + 0.0312*(B^2.1) - 0.184*(B^8) + 0.039*(B^4/(1-B^4))
49 - 0.05184*B^3 + 91.71*(B^2.5)*(Re.^-0.75);
50 qm = (Cd/(sqrt(1-B^4)))*e1*(pi/4)*(d^2)*(sqrt(2*dp.*rho1)); % Re = (4*qm)/(pi*u*D)
51 err = abs(Cd1 - Cd);
52 i = i+1;
53 end
54
55 qm
56 Cd
57 Re
58
59 figure(1)
60 plot(P1,qm,'r*')
61 hold on
62 plot(P1,qm,'b-')
63 title('Pressure vs Mass Flow for 5000rpm')
64 xlabel('Pressure Upstream [kPa]')
65 ylabel('Mass Flow Rate [kg/s]')
```

B.2. Matlab code for Coefficient of Resistance calculation

```
1  % Fourie Wiid (25-03-2017)
2  % Coefficients of Resistance
3  clc; clear all;
4
5  m_dot1 = 0.00288; %Mass flow rate case 1[kg/s]
6  m_dot2 = 0.00647; %Mass flow rate case 2[kg/s]
7  P1 = 1.35; %Pressure case 1 [Pa]
8  P2 = 5.43; %Pressure case 2 [Pa]
9
10 A = 0.000113097; %Area [m^2]
11 rho = 998; %Density [kg/m^3]
12 L = 0.0015; %Length of porous medium
13
14 V1 = m_dot1/(rho*A);%Velocity case 1 [m/s]
15 V2 = m_dot2/(rho*A);%Velocity case 1 [m/s]
16
17 tau = 1; %Initial guess
18 err = 1; %Error initial
19 i = 0;
20 while err > 1e-12
21     tau1 = tau; %For iteration
22     alpha = (2/V2)*(P2/(rho*V2) -tau); %Coefficient for inertial
23     tau = P1/(V1*rho) - 0.5*alpha*V1; %Coefficient for viscous
24     err = abs(tau - tau1);
25     i = i+1;
26 end
27
28 alpha
29 tau
```

B.3. Matlab code for Iterated experimental uncertainties

```
1  % Fourie Wiid (02-02-2018)
2  % Iterated exmerimental uncertainty of Discharge coefficient
3  clear all; clc
4
5  % Experimental uncertainties of parameters
6  % Calculations are in Appendix D
7  UP = 0.25; %Pressure
8  UB = 0.22; %Beta
9  Ud = 0.1; %Orifice diameter
10 UD = 0.2; %Pipe diamter
11 Uu = 0.97; %Dynamic viscosity
12 Urho = 0.56 %Density
13 Ue = 1.98 %Expansion factor
14
15 %Initial guess
16 Uq = 0;
17 UCd = 0;
18 i = 0;
19 x = 50;
20
21 for k = 1:1:x
22 i = i + 1;
23 Uq = ((UCd)^2+(4*UB)^2+(2*Ud)^2+...
24 (Ue)^2+(0.5*UP)^2+(0.5*Urho)^2)^0.5; %Mass flow uncertainty
25 URe = ((Uq)^2+(Urho)^2+(UD)^2+(Uu)^2)^0.5; %Reynolds Number uncertainty
26 UCd = ((2.1*UB)^2+(8*UB)^2+(3*UB)^2+...
27 (2.5*UB)^2+(0.75*URe)^2)^0.5; %Discharge coefficient uncertainty
28 Uq1(i) = Uq;
29 URe1(i) = URe;
30 UCd1(i) = UCd;
31 end
32
33 figure(1)
34 plot(1:1:x,UCd1,'b');
35 hold on
36 plot(1:1:x,Uq1,'r')
37 plot(1:1:x,URe1,'g')
38 title('Iterated Experimental Uncertainties')
39 xlabel('Number of Iterations')
40 ylabel('Uncertainty [%]')
41 legend('Cd', 'Mass Flow', 'Re')
42 hold on
43 plot(0.2465,11.42,'kp')
44 plot(0.4335,8.676,'kp')
45 hold off
```

C.1. Pressure gauge – SA Gauge DPG – 502






 Reg No. 200208711523		
	146 208 308 846 1446 1546	
CERTIFICATE OF CALIBRATION		
CERTIFICATE NUMBER: 208-38449		
	Calibration of a : Standard Test Gauge Manufacturer : SA Gauge Model No : DPG-502 Serial No : 20101804	
	Calibrated for : [REDACTED] Address : [REDACTED]	
	Issue Date : 15 March 2017 Calibration Date : 15 March 2017 Recommended due date : March 2018	
	Technical Signatory : J.A. Byvelds  Calibrated by : J.A. Byvelds Checked by : M. Alvares 	
<p>The South African National Accreditation System (SANAS) is a member of the International Laboratory Accreditation Co-Operation (ILAC) for the Mutual Recognition Agreement (MRA). The MRA allows for the mutual recognition of technical test and calibration data by the member accreditation bodies worldwide. For more information on the MRA please refer to www.ilac.org</p> <p>Copyright of this certificate is owned by REPCAL SERVICES. This certificate may not be reproduced other than in full, except with prior written approval of REPCAL SERVICES</p> <p>The calibration values in the certificate were correct at the time of calibration. The continuous accuracy of the instrument will depend on such factors as the care exercised in handling and use of the instrument and the frequency of use. Re-calibration should be performed after a period which has been chosen to ensure that the item's accuracy remains within the desired limits.</p>		
508 Nupen Crescent Halfway House Midrand	P.O. Box 6093 Halfway House 1685	Phone (011) 315 3134 Fax (011) 315 8726 e-mail : service@repcal.co.za

Figure C.1 Pressure gauge – SA Gauge DPG – 502 Calibration Certificate

C.1. Pressure gauge – SA Gauge DPG – 502 (Data Sheet)

Page 15-1



PRESSURE MEASUREMENT
Digital Gauge
 Type DPG502: Digital Pressure Gauge

Service Intended
 General purpose digital gauge, suitable for media such as air, water, oil & gases that do not attack stainless steel parts or will obstruct the pressure system. Typical applications will be in the general industrial and hydraulic industry.

Description
 The DPG 502 is a digital pressure gauge with an accuracy of 0.2% of full scale. It features a max/peak pressure memory function.

Features
 Low power consumption, 1200 hours battery life.
 High accuracy and stability.
 Maximum (Peak) value function.
 Zero and full scale calibration function.


Case Dimension
 Nominal Dia: 67mm x 35mm deep

Pressure Connections
 Material: Stainless steel 316
 Sizes: 1/4" BSP Standard (other on request)

Technical Specifications

Accuracy	: +/- 0.25% Full Scale
Pressure Range	: As per standard ranges in chart
Pressure units	: kPa, MPa, bar, psi and kg/cm ²
Display	: 4 digit LCD with back light,
Digit Dimensions	: 12mm digit height
Bar Graph	: Percentage of full scale
Battery Status	: Condition display - 5 segments
Sampling Rate	: 4 times per second
Memory	: Max pressure value
Auto Power	: Selectable 1-15 min
Zero Function	: zero reset and adjustment
Reset:	: Delete max/peak value
Temp Compensation:	: -10+70 °C
Temp Stability	: 0.05% FS/°C
Operational Spec	: Ambient Temp -10+60 °C Medium Temp -10+80 °C
Relative Humidity	: 0-90% non-condensing
Burst Pressure	: 3 x FS
Over Pressure	: 1.5 x FS
Wetted Parts	: Stainless Steel 316
Power	: 9V battery (6LR61)
Weight	: 0.25kg

Optional Extras
 Calibration Certificate
 Diaphragm Seals fitted
 Rubber Cover





STANDARD PRESSURE RANGES					
Range	Accuracy (% FS)	Resolution	Range	Accuracy (% FS)	Resolution
Pressure			Pressure		
0/25 kPa	0.25	0.01	0/1 MPa	0.25	1.0
0/70 kPa	0.25	0.1	0/10 MPa	0.25	1.0
0/100 kPa	0.25	0.1	0/25 MPa	0.25	10.0
0/250 kPa	0.25	0.1	0/40 MPa	0.25	10.0
0/400 kPa	0.25	0.1	0/60 MPa	0.25	10.0
0/600 kPa	0.25	0.1	0/70 MPa	0.25	10.0
0/1000 kPa	0.25	1.0	0/80 MPa	0.25	10.0
0/1600 kPa	0.25	1.0			
0/2500 kPa	0.25	1.0			
0/4000 kPa	0.25	1.0	Vacuum		
			-1000 kPa	0.5	0.1


Customized and other scales such as bar / psi / inHG etc. are available on request

Figure C.2 Pressure gauge – SA Gauge DPG – 502 Data Sheet


C.2. Temperature gauge – Ero Electronic Monocal 2000




Certificate of Calibration



This certificate is issued without alteration, and in accordance with the conditions of accreditation granted by SANAS. It is a correct record of the measurements made at the time of calibration. Copyright of this certificate is owned jointly by SANAS and InterCal and may not be reproduced other than in full, except with the prior written approval of SANAS and InterCal. The values given in this certificate were correct at the time of calibration. Subsequently the accuracy will depend on factors such as care exercised in handling the instrument and frequency of use. Recalibration should be performed after a period which has been chosen to ensure that, under normal circumstances, the instrument accuracy remains within the desired limits. The accuracy of all measurements were traceable to the national measuring standards as maintained in South Africa, unless otherwise noted. The uncertainties of measurements were estimated for a coverage factor of k=2 which approximates a 95% confidence level.

Certificate no	: I20239	Rev: 1
Manufacturer	: Ero Electronic	
Description	: Handheld Calibrator	
Model No	: Memocal 2000	
Serial No	: 06.41.3400	
Calibrated for Address	: [REDACTED]	
Temperature	: 23 °C	
Relative Humidity	: 33 % RH	
Date of calibration	: 7 August 2016	Print Date : 7 August 2017
Expiry Date	: 7 August 2017	
Calibrated by	: J.B. Kirkland	Checked by : 

It is hereby certified that this is a true copy of the original document and that there is no indication that alterations have been made thereto by an unauthorized person on the original.
 2017-08-23
 SA POST OFFICE
 DURBAN
 031 261 1114



The South African National Accreditation System (SANAS) is a member of the International Laboratory Accreditation Cooperation (ILAC) Mutual Recognition Arrangement (MRA). This Arrangement allows for the mutual recognition of technical test and calibration data by the member accreditation bodies worldwide. For more information in the Arrangement please consult www.ilac.org

SANAS Authorised Signatory
P. Haarhoff

Page 1 of 7

InterCal CC Reg: CK1992/28397/23
 907 Richards Drive, Halfway House, Midrand
 PO Box 10907 Vorna Valley 1688
 Tel (011) 315 4321 Fax: (011) 312 1322 e-mail: intercal@intercal.co.za www.intercal.co.za
 Members: PS Haarhoff OC Snelling

Figure C.3 Temperature gauge – Ero Electronic Monocal 2000 Calibration Certificate

C.2. Temperature gauge – Ero Electronic Monocal 2000 (Calibration Data)

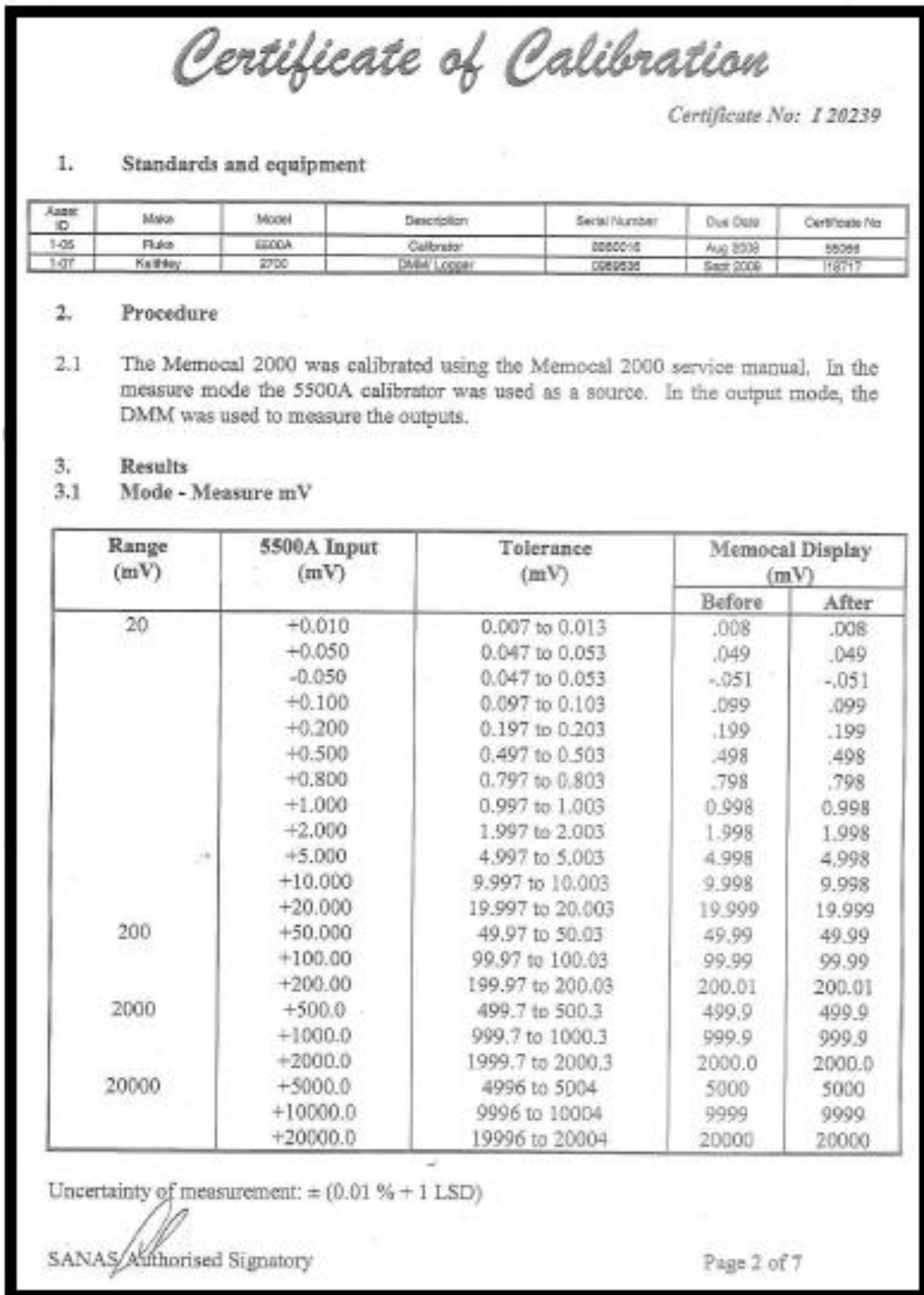


Figure C.4 Temperature gauge calibration data page 2

Certificate of Calibration

Certificate No: I 20239

3.2 Mode - Measure mA

Range (mA)	5500A Input (mA)	Tolerance (mA)	Memocal Display (mA)	
			Before	After
20	+0.0100	.007 to .013	.010	.010
	+0.0500	.047 to .053	.050	.050
	+0.1000	.097 to .103	.100	.100
	+0.5000	.497 to .503	.500	.500
	+1.0000	.997 to 1.003	1.000	1.000
	+5.0000	4.997 to 5.003	5.000	5.000
	-10.0000	-9.997 to -10.003	-9.998	-9.998
200	20.000	19.997 to 20.003	19.999	19.999
	50.00	49.97 to 50.03	50.00	50.00
	100.00	99.97 to 100.03	100.00	100.00
	200.00	199.97 to 200.03	200.02	200.02

Uncertainty of measurement: $\pm (0.01 \% + 1 \text{ LSD})$

SANAS  Authorised Signatory

Page 3 of 7

Figure C.5 Temperature gauge calibration data page 3

Certificate of Calibration

Certificate No: I 20239

3.3 Mode - Output mV

Range (mV)	Nominal Value (mV)	Tolerance (mV)	Measured Value (mV)	
			Before	After
20	0.020	.017 to .023	0.019	0.019
	0.050	.047 to .053	0.049	0.049
	0.100	.097 to .103	0.099	0.099
	0.500	.497 to .503	0.499	0.499
	1.000	.997 to 1.003	0.999	0.999
	5.000	4.997 to 5.003	4.999	4.999
	10.000	9.997 to 10.003	9.999	9.999
	20.000	19.997 to 20.003	19.999	19.999
200	50.00	49.97 to 50.03	50.00	50.00
	100.00	99.97 to 100.03	100.00	100.00
	200.00	199.97 to 200.03	200.00	200.00
2000	500.0	499.7 to 500.3	500.0	500.0
	1000.0	999.7 to 1000.3	1000.0	1000.0
	2000.0	1999.7 to 2000.3	1999.9	1999.9
20000	5000	4997 to 5003	4999	4999
	10000	9997 to 10003	9999	9999
	20000	19997 to 20003	20000	20000

Uncertainty of measurement: $\pm (0.01 \% + 1 \text{ LSD})$


SANAS Authorised Signatory

Page 4 of 7

Figure C.6 Temperature gauge calibration data page 4

Certificate of Calibration

Certificate No: I 20239

3.4 Mode - Output mA

Memocal output (mA)	Tolerance (mA)	Measured Value (mA)	
		Before	After
00.10	.097 to .103	.100	.100
00.50	.497 to .503	.500	.500
01.00	.997 to 1.003	1.000	1.000
05.00	4.997 to 5.003	5.000	5.000
10.00	9.997 to 10.003	10.000	10.000
19.00	18.997 to 19.003	19.000	19.000

Uncertainty of measurement: $\pm (0.05 \% + 1 \text{ LSD})$

3.5 Mode - Output °C

N.B Calibrated against ITS 90 tables

Output (°C)	TC Type	Tolerance (°C)	Measured value (°C)	
			Before	after
100.0	K Type	99.6 to 100.4	100.1	100.1
500.0	K Type	499.6 to 500.5	500.1	500.1
1000.0	K Type	999.3 to 1000.7	1000.1	1000.1
1000.0	R Type	999.3 to 1000.7	999.9	999.9
1000.0	S Type	999.3 to 1000.7	999.8	999.8
200.0	T Type	199.5 to 200.5	200.0	200.0
200.0	J Type	199.6 to 200.4	200.1	200.1

Uncertainty of measurement: $\pm 0.5 \text{ °C}$


SANAS Authorised Signatory

Page 5 of 7

Figure C.7 Temperature gauge calibration data page 5

Certificate of Calibration

Certificate No: I 20239

3.6 Mode - Measure Ω

Input (Ω)	Tolerance (Ω)	Memocal Display (Ω)	
		Before	After
100.00	99.9 to 100.1	100.1	100.1

Uncertainty of measurement: ± 0.1 % Equivalent to $0\text{ }^{\circ}\text{C} \pm 0.5\text{ }^{\circ}\text{C}$

3.7 Mode - Measure RTD

Range	Input (Ω)	Tolerance ($^{\circ}\text{C}$)	Memocal Display ($^{\circ}\text{C}$)	
			Before	After
Pt 100	100.00 (0.0 $^{\circ}\text{C}$)	-0.1 to 0.1	- 0.1	- 0.1
Ni 100	100.00	-0.1 to 0.1	- 0.1	- 0.1

Uncertainty of measurement: $\pm 0.1\text{ }^{\circ}\text{C}$

3.8 Mode - Measure $^{\circ}\text{C}$

N.B Calibrated against ITS 90 tables.

Nominal ($^{\circ}\text{C}$)	Int Ref. Selected	Tolerance ($^{\circ}\text{C}$)	Memocal Display ($^{\circ}\text{C}$)	
			Before	After
100.0	K Type	99.6 to 100.4	99.9	99.9
500.0	K Type	499.5 to 500.5	499.8	499.8
1000.0	K Type	999.3 to 1000.7	999.8	999.8
1000.0	R Type	999.3 to 1000.6	999.6	999.6
1000.0	S Type	999.3 to 1000.06	999.4	999.4
200.0	T Type	199.5 to 200.5	199.8	199.8
200.0	J Type	199.6 to 200.4	199.7	199.7

Uncertainty of measurement: $\pm 0.5\text{ }^{\circ}\text{C}$

SANAS Authorised Signatory 

Page 6 of 7

Figure C.8 Temperature gauge calibration data page 6

Certificate of Calibration

Certificate No: I 20239

3.9 Cold Junction Check

Short the UUT input terminals together. Set the UUT to measure K-type temperature. Measure the ambient temperature between the terminals and compare to the UUT display.

UUT Display (°C)	Measured Value (°C)
23.5	23.3

Uncertainty of measurement: Temperature ± 1 °C

4 Note

- 4.1 The results reflected on this certificate were entered directly on PC.
- 4.2 The UUT was found to meet manufacturers specifications, unless otherwise noted with a (*).

----- End of document -----


SANAS Authorised Signatory

Page 7 of 7

Figure C.9 Temperature gauge calibration data page 7

Appendix D – Uncertainty in Experimental Data

D.1. Uncertainty method

The method used to estimate the uncertainties comes from White (2011) and makes use of calculus. The uncertainty for an important variable is derived by using partial differentiation. The equation D.1 (White, 2011) shows the estimate for uncertainty δx for the single experimental variable x on which the desired results P is dependent.

$$\delta P \approx \frac{\partial P}{\partial x} \delta x$$

[eq D.1]

If P were multi variable dependent, $P = P(x_1, x_2, x_3, \dots, x_N)$, the overall uncertainty δP is estimated and show in equation D.2 with root-mean-square (White, 2011).

$$\delta P = \left[\left(\frac{\partial P}{\partial x_1} \delta x_1 \right)^2 + \left(\frac{\partial P}{\partial x_2} \delta x_2 \right)^2 + \dots + \left(\frac{\partial P}{\partial x_N} \delta x_N \right)^2 \right]^{\frac{1}{2}}$$

[eq D.2]

If the quantity P were a power-law expression of the other variables, $P = Const x_1^{n_1} x_2^{n_2} x_3^{n_3} \dots$, the each derivative in eq D.2 is proportional to P and the relevant power-law exponent and is inversely proportional to that variable (White, 2011). Equation D.3 shows how P is expressed against each relative variable.

$$\frac{\partial P}{\partial x_1} = \frac{n_1 P}{x_1}; \frac{\partial P}{\partial x_2} = \frac{n_2 P}{x_2}; \frac{\partial P}{\partial x_3} = \frac{n_3 P}{x_3}; \dots$$

[eq D.3]

Thus, from equations D.2 and D.3 the overall uncertainty can be estimated for quantity P . Equation D.4 shows the overall uncertainty estimate for quantity P (White, 2011).

$$\frac{\delta P}{P} = \left[\left(n_1 \frac{\delta x_1}{x_1} \right)^2 + \left(n_2 \frac{\delta x_2}{x_2} \right)^2 + \left(n_3 \frac{\delta x_3}{x_3} \right)^2 + \dots \right]^{\frac{1}{2}}$$

[eq D.4]

D.2. Experimental Setup

The list of components used with their accuracies are listed in Table D.1. The calibration certificates for the gauges are in **Appendix C**.

Table D.1 Components with accuracies of Experimental Setups

Component	Description	Accuracy
Pressure gauge	SA Gauge Model DPG 502 (SA Gauge)	± 0.25%
Temperature gauge	Ero Electronic Model Memocal 2000 (Eurotherm)	± 0.5%
Orifice	ASME specification, Diameter 19.4 mm	± 0.1%
VSD Motor	Brook Crompton 3kW DC motor, with U&S Power Electronic Drives system.	-
Aluminium Tube	Non-Ferrous metal works manufacturing	± 0.2%

The ASME (1990) flow equations are used to calculate the uncertainty of the experimental setup, since the setup is designed with these equations and used to calculate the mass flow rate.

The uncertainty for diameter ratio, β :

$$\beta = \frac{d}{D}$$

$$U_{\beta} = \frac{\delta\beta}{\beta} = \left[\left(\frac{\delta d}{d} \right)^2 + \left(\frac{\delta D}{D} \right)^2 \right]^{\frac{1}{2}}$$

$$U_{\beta} = [(0.1)^2 + (0.2)^2]^{\frac{1}{2}}$$

$$U_{\beta} = 0.22 \%$$

The uncertainty for expansion factor, ε :

$$\varepsilon = 1 - (0.351 + 0.256\beta^4 + 0.93\beta^8) \left[1 - \left(\frac{P_2}{P_1} \right)^{\frac{1}{\gamma}} \right]$$

$$U_{\varepsilon} = \frac{\delta\varepsilon}{\varepsilon} = \left[\left(4 \frac{\delta\beta}{\beta} \right)^2 + \left(8 \frac{\delta\beta}{\beta} \right)^2 + \left(\frac{1}{1.4} \frac{\delta\Delta P}{\Delta P} \right)^2 + \left(\frac{1}{1.4} \frac{\delta\rho}{\rho} \right)^2 \right]^{\frac{1}{2}}$$

$$U_{\varepsilon} = \left[(4 * 0.22)^2 + (8 * 0.22)^2 + \left(\frac{1}{1.4} * 0.25 \right)^2 + \left(\frac{1}{1.4} * 0.56 \right)^2 \right]^{\frac{1}{2}}$$

$$U_{\varepsilon} = 2.02 \%$$

The uncertainty for density, ρ :

$$\rho = \frac{P}{RT}$$

$$U_\rho = \frac{\delta\rho}{\rho} = \left[\left(\frac{\delta P}{P} \right)^2 + \left(\frac{\delta T}{T} \right)^2 \right]^{\frac{1}{2}}$$

$$U_\beta = [(0.25)^2 + (0.5)^2]^{\frac{1}{2}}$$

$$U_\beta = 0.56 \%$$

The uncertainties for the discharge coefficient and mass flow have to be iterated. The reason for this is that the equations are dependent of each other. A Matlab script was written to perform the iteration calculations (see **Appendix B**). The initial guesses of the discharge and mass flow rate are calculated below.

The uncertainty for discharge coefficient, C_d :

$$C_d = 0.5959 + 0.0312\beta^{2.1} - 0.184\beta^8 + 0.039 \frac{\beta^4}{(1 - \beta^4)} - 0.05184\beta^3 + 91.71\beta^{2.5} Re^{-0.75}$$

$$U_{C_d} = \frac{\delta C_d}{C_d} = \left[\left(2.1 \frac{\delta\beta}{\beta} \right)^2 + \left(8 \frac{\delta\beta}{\beta} \right)^2 + \left(3 \frac{\delta\beta}{\beta} \right)^2 + \left(2.5 \frac{\delta\beta}{\beta} \right)^2 \right]^{\frac{1}{2}}$$

$$U_{C_d} = [(2.1 * 0.22)^2 + (8 * 0.22)^2 + (3 * 0.22)^2 + (2.5 * 0.22)^2]^{\frac{1}{2}}$$

$$U_{C_d} = 2.01 \%$$

This uncertainty is used as an initial guess

The uncertainty for mass flow rate, \dot{q} :

$$\dot{q} = \frac{C_d}{\sqrt{1 - \beta^4}} \left(\frac{\pi}{4} d^2 \right) \varepsilon (\sqrt{2\rho\Delta P})$$

$$U_q = \frac{\delta\dot{q}}{\dot{q}} = \left[\left(\frac{\delta C_d}{C_d} \right)^2 + \left(4 \frac{\delta\beta}{\beta} \right)^2 + \left(2 \frac{\delta d}{d} \right)^2 + \left(\frac{\delta\varepsilon}{\varepsilon} \right)^2 + \left(\frac{1}{2} \frac{\delta\Delta P}{\Delta P} \right)^2 + \left(\frac{1}{2} \frac{\delta\rho}{\rho} \right)^2 \right]^{\frac{1}{2}}$$

$$U_q = \left[(1.92)^2 + (4 * 0.21)^2 + (2 * 0.05)^2 + (1.90)^2 + \left(\frac{1}{2} * 0.25 \right)^2 + \left(\frac{1}{2} * 1.52 \right)^2 \right]^{\frac{1}{2}}$$

$$U_q = 2.93\%$$

Figure D.1 shows that the experimental uncertainties that are iterate to specific values.

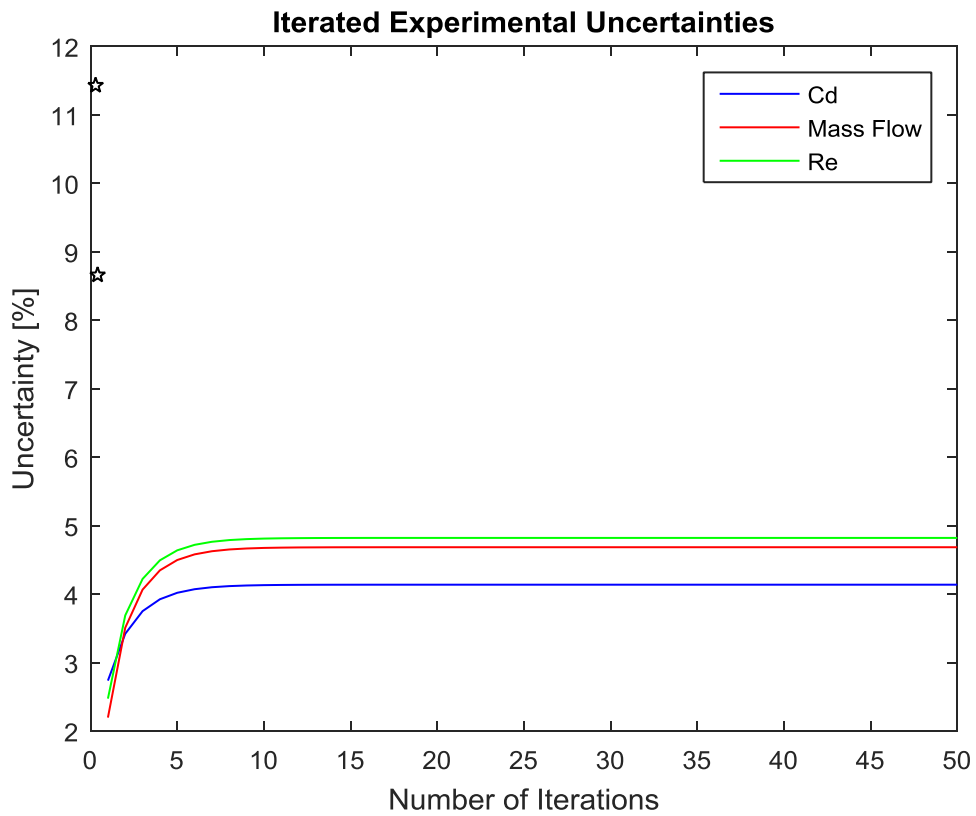


Figure D. 1 Uncertainty vs Number of Iterations

The uncertainties are as follow:

$$U_{C_d} = 4.14 \%$$

$$U_q = 4.68 \%$$

$$U_{Re} = 4.82 \%$$

The uncertainty for the final mass flow rate is $\pm 4.7\%$. Thus the uncertainty error with all variables considered in the experimental data is $\pm 4.7\%$.

D.3. Coefficient of Resistance setup

The list of components used with their accuracies are listed in Table D.2.

Table D.2 Components with accuracies of Coefficient of Resistance Setup

	Model	Accuracy
Weight Scale	Tanita -147J2 Pocket Multi	± 0.10 %
Measurements	DANIU Digital Stainless Electronic Vernier Calliper Gauge	± 0.20 %
Stopwatch	Timex Ironman 657 V4	± 0.10 %

The error of uncertainty for mass flow rate, \dot{m} :

$$\dot{m} = \frac{\text{mass}}{\text{time}} \quad [\text{kg/s}]$$

$$U_m = \frac{\delta \dot{m}}{\dot{m}} = \left[\left(\frac{\delta m}{m} \right)^2 + \left(\frac{\delta t}{t} \right)^2 \right]^{\frac{1}{2}}$$

$$U_m = [(0.1)^2 + (0.1)^2]^{\frac{1}{2}} = 0.14 \%$$

The error of uncertainty for Head pressure, P:

$$P = \rho H g \quad [\text{Pa}]$$

$$U_P = \frac{\delta P}{P} = \left[\left(\frac{\delta H}{H} \right)^2 \right]^{\frac{1}{2}}$$

$$U_P = [(0.25)^2]^{\frac{1}{2}} = 0.25 \%$$

The error of uncertainty for coefficients of resistance is estimate with the mass flow rate and pressure, since those variables are used to determine the coefficients. The velocity has the same uncertainty as the mass flow rate, since the velocity is calculated from the mass flow rate which has a linear relationship with velocity.

$$P = \rho \tau V + \frac{1}{2} \rho \propto V^2$$

$$U_\alpha = \frac{\delta \alpha}{\alpha} = \left[\left(\frac{\delta P}{P} \right)^2 + \left(2 \frac{\delta V}{V} \right)^2 + \left(\frac{\delta V}{V} \right)^2 \right]^{\frac{1}{2}}$$

$$U_\alpha = [(0.25)^2 + (2 * 0.14)^2 + (0.14)^2]^{\frac{1}{2}} = 0.35 \%$$

The coefficients of resistance α and τ have the same experimental uncertainty. The uncertainty in the coefficients of resistance results all variables included is **± 0.4%**.

Appendix E – Coefficients of Resistance

E.1. Introduction

The test setup in Figure E.1 was constructed to determine the coefficient of flow resistance of the brush used in the brush seal. The method makes use of plotting the mass flowrate versus pressure. The mass flow rate is obtained by measuring the amount of fluid that passes through the seal section during a specific time period. The fluid that is being used is water and its density is well known. Thus the pressure on the seal can be calculated with the density, height of the water column, and gravity. By repeating the experiment at different heights, a performance curve of mass flowrate vs pressure can be obtained. By using the performance curve, the coefficient of resistance can be derived.

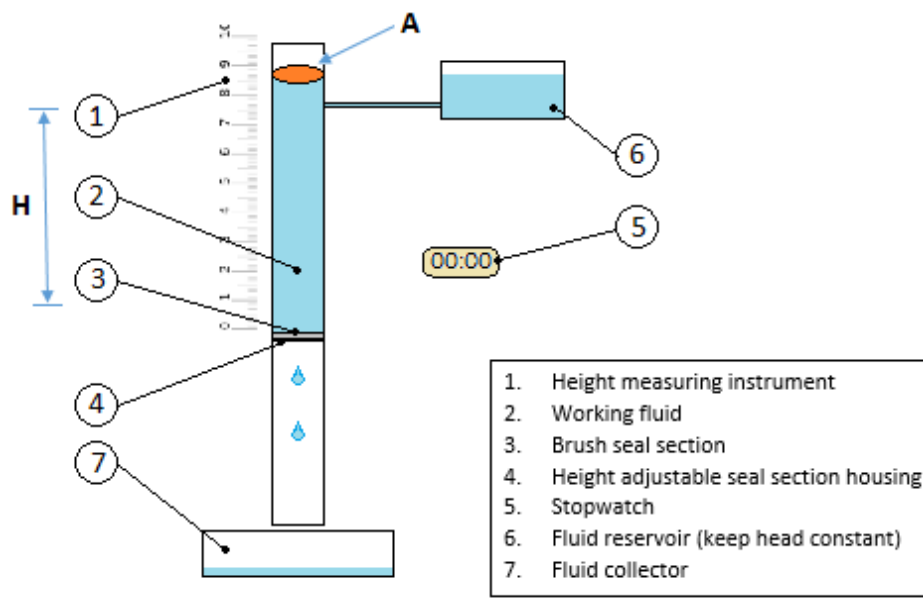


Figure E.1 Coefficient of resistance test setup

E.2. Coefficients of Resistance

The coefficients of resistance cannot directly be inserted in to STAR. The coefficients need to be rewritten in the following format:

$$P = \varphi + \rho\tau V + \frac{1}{2}\rho\alpha V^2 \quad [\text{eq E.1}]$$

The coefficients α and τ in equation E.1 are the inertial and viscous resistances. These coefficients are shown in equations E.2 and E.3 with their units.

$$\frac{\rho\alpha}{L} \left[\frac{kg}{m^4} \right]$$

[eq E.2]

$$\frac{\rho\tau}{L} \left[\frac{kg}{m^3s} \right]$$

[eq E.3]

With the L is the length of the porous medium.

The mass flow rate is calculated with equation E.4 for the test setup.

$$\dot{m} = \frac{mass}{time} \quad [kg/s]$$

[eq E.4]

The pressure is calculated with equation E.5 for the test setup.

$$P = \rho Hg \quad [Pa]$$

[eq E.5]

From the mass flow rate and head pressure the velocity is calculated and used to determine the coefficients α and τ . A Matlab script performs the mass flow rate and velocity calculations, see **Appendix B**.

E.3. Test Setup

The test setup makes use of a cylindrical column in which a section of the brush bristles used in the experimental method (discussed in Chapter 3) is mounted in. The brush section is mounted at various heights. A larger container is attached at the top of the column to keep the head in column approximate by constant. Fluid (water) is then allowed to flow through the brush section and the fluid is then capture and weighed.

E.4. Procedure

The brush bristle section is fitted in the column at a specified height from the top of the column. The heights at which the section is mounted are 100 mm, 200 mm, 300 mm, 400 mm and 500 mm. The fluid flows through the seal section for 60 seconds and the fluid which passes through the section captured. The captured fluid is measured and the mass flow rate

is calculated with time and the captured fluid is mass. The head pressure is calculated for each height. This procedure is repeated for all of the mounted heights.

E.5. Experimental Uncertainty

The list of components used with their accuracies are listed in Table E.1

Table E.1 Components with accuracies of Coefficient of Resistance Setup

	Model	Accuracy
Weight Scale	Tanita -147J2 Pocket Multi	0.10 %
Vernier Calliper	DANIU Digital Stainless Electronic Vernier Calliper Gauge	0.25%
Stopwatch	Timex Ironman 657 V4	0.10 %

The coefficients of resistance α and τ have the same experimental uncertainty. The uncertainty in the coefficients of resistance results with all variables included is **0.4%**. The full calculation is given in **Appendix D**.

E.6. Results

Table E.2 show the results of the experimental test.

Table E.2 Coefficient of Resistance results

Height [mm]	Capture Fluid [kg]	Head Pressure [Pa]	Mass flow rate [x10E-3 kg/s]
0	0.0	0.0	0.0
15	0.040	0.204	0.66
25	0.067	0.340	1.12
50	0.092	0.679	1.54
75	0.152	1.019	2.53
100	0.173	1.36	2.88
150	0.210	2.037	3.46
200	0.247	2.72	4.12
300	0.315	4.08	5.25
400	0.388	5.43	6.47
500	0.458	6.79	7.64

The coefficients α and τ were calculated to be:

$$\alpha = 4.0071$$

$$\tau = 0.0017$$

The coefficients are substituted in equation E.1 to obtain the resistance equation for STAR. Figure E.2 show the mass flow rate versus the head pressure for the result of the tests. The relation for mass flow rate versus head pressure is linear.

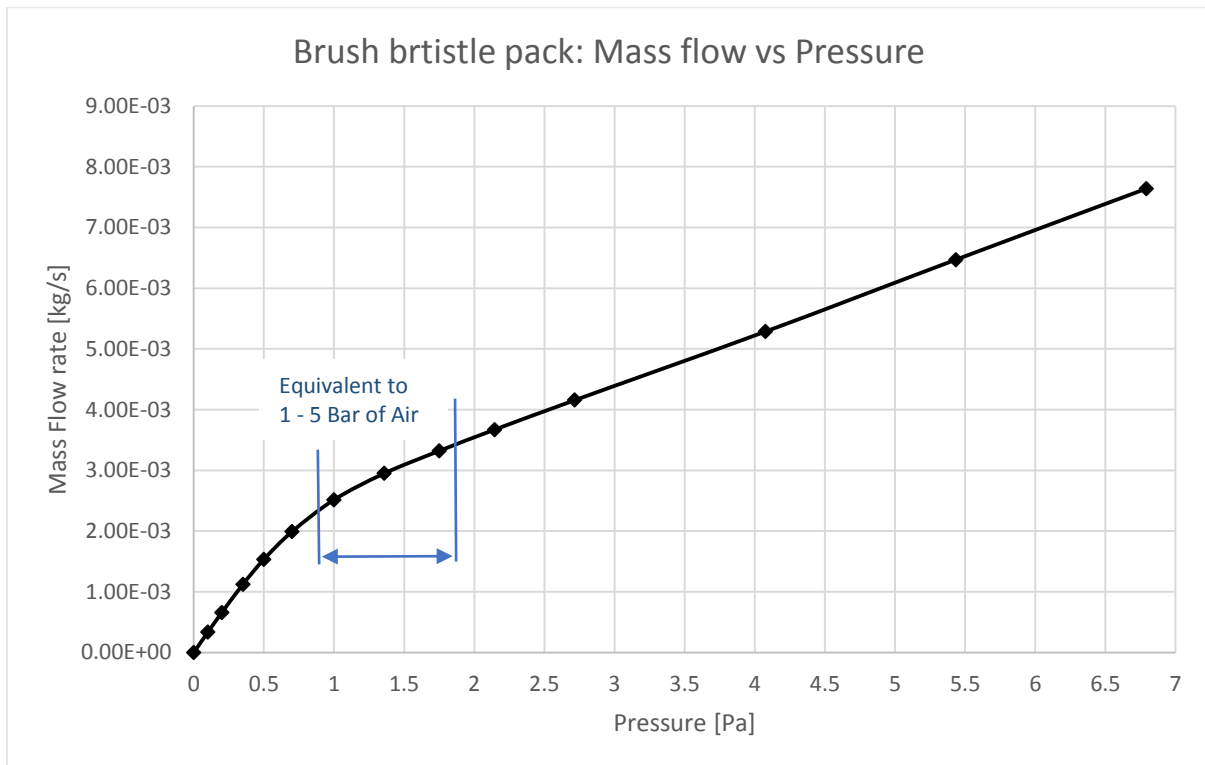


Figure E.2 Mass flow rate vs Pressure for Coefficients of Resistance

The result show that the behaviour of the bristle pack change after 0.7 Pa to a linear type trend instead of a 2nd order polynomial. This means that the fluid flow gets restricted more at the lower pressure than the higher pressures. The supply air pressure that is used in the experimental method (Chapter 3) air equivalent falls within the tested pressures of bristle pack. This means that pressures used to obtain the coefficients of resistance are relevant and useful. Figure E.3 shows the air equivalent for the mass flow vs pressure with its 2nd order polynomial trendline.

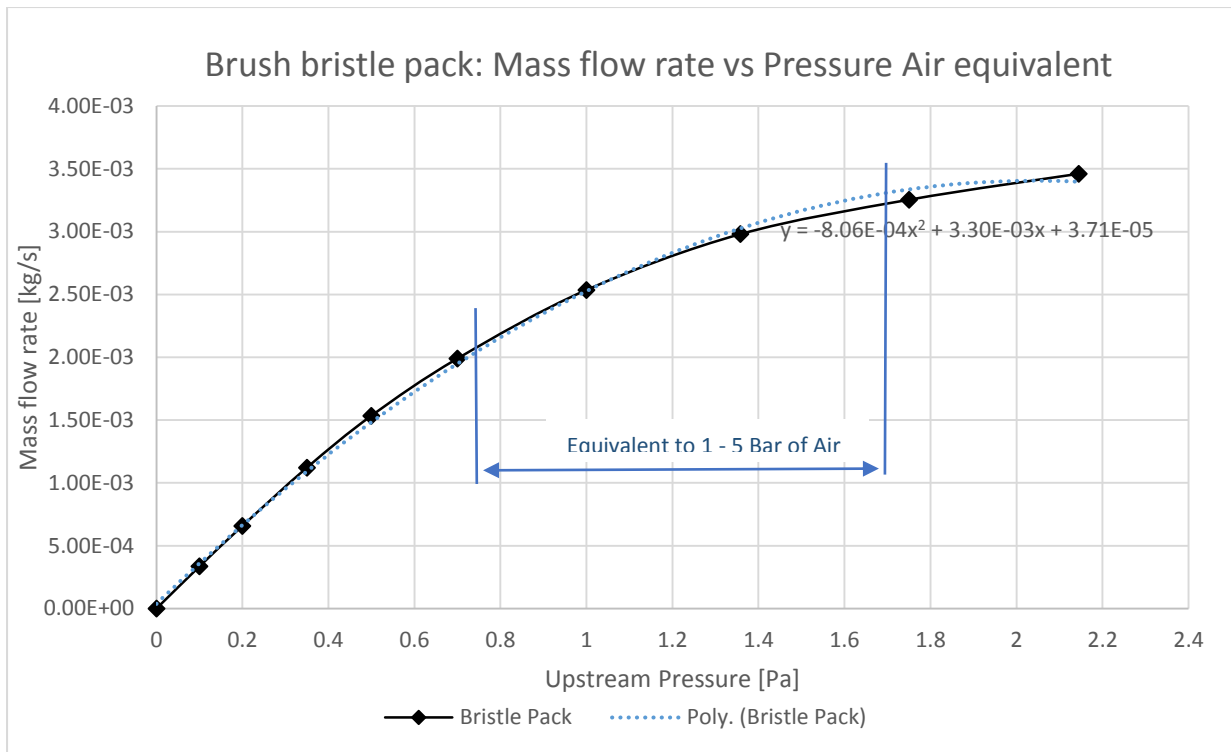


Figure E.3. Mass flow rate vs Pressure for Air equivalent

The graph that there are a slight deviation in from the trendline to the data points. The trendline further shows good correlation with the rest of the air equivalent section.

Appendix F – Labyrinth seal leakage area

The leakage area of the labyrinth seal is used in the calibration exercise described in section 5.2. Therefore an equivalent size nozzle must be found for the exercise to ensure that the system is able to accommodate the full-size labyrinth seal that will be tested.

The leakage area is calculated with Eq F.1;

$$A_{leakage} = \frac{\pi}{4} (D_{seal}^2 - D_{shaft}^2) \quad [\text{Eq F.1}]$$

The diameter used is listed below,

- Labyrinth seal inside diameter, $D_{seal} = 150.48 \text{ mm}$
- Shaft outer diameter, $D_{shaft} = 150.0 \text{ mm}$

$$A_{leakage} = 113.28 \text{ mm}^2$$

The equivalent nozzle size is calculated with Eq F.3;

$$A_{leakage} = \frac{\pi}{4} d_{nozzle}^2 \quad [\text{Eq F.2}]$$

$$d_{nozzle} = \sqrt{\frac{4}{\pi} A_{leakage}} \quad [\text{Eq F.3}]$$

By using the leakage and Eq F.3 the equivalent size nozzle is calculated.

$$d_{nozzle} = 12.01 \text{ mm}$$

Thus full-size labyrinth seal that will be tested corresponds to an equivalent size nozzle with a diameter of **12mm**.

Appendix G – Mesh independence study

For each CFD study, a mesh independence must be done. The mesh independence is where the results are independent from the mesh. The mesh has to be refined to such a level where the results do not change within a certain percentage. The study consisted of running simulations for one set of conditions with different mesh sizes.

The mesh independence study makes use of the Grid Convergence Index (GCI) from ASME V&V (2009) and Roach (1998). The method makes use of a series of meshes with different sizes that increase with a constant grid refinement ratio, r . The ratio defines the relationship between successive meshes, for example if $r = 2$ then the mesh is doubled in each of the dimensions in the domain. By using a performance parameter, f from the CFD solution, an order of convergence, z can be calculated with three successively refined CFD solutions. The order of convergence is calculated with equation G.1 (ASME V&V, 2009).

$$z = \ln\left(\frac{f_3 - f_2}{f_2 - f_1}\right) / \ln(r)$$

[eq G.1]

The GCI of the fine grid is defined in equation G.2 (ASME V&V, 2009),

$$GCI_{fine} = \frac{F_s |\epsilon|}{r^z - 1}$$

[eq G.2]

Where F_s is a factor of safety ($F_s = 1.25$ when a minimum of 3 solutions are available (Roach, 1998)) and the relative error, ϵ is defined by equation G.3 (ASME V&V, 2009),

$$\epsilon = \frac{f_2 - f_1}{f_1}$$

[eq G.3]

When three solutions are used, the GCI_{12} and GCI_{23} are given in a dimensionless form equation G.4 (ASME V&V, 2009),

$$GCI_{12} = \frac{F_s \left| \frac{f_2 - f_1}{f_1} \right|}{r^z - 1} \quad \text{and} \quad GCI_{23} = \frac{F_s \left| \frac{f_3 - f_2}{f_2} \right|}{r^z - 1} \quad [\text{eq G.4}]$$

If the asymptotic range is reached,

$$GCI_{23} \approx r^z GCI_{12}$$

Thus, if

$$\frac{GCI_{23}}{r^z GCI_{12}} \approx 1$$

Then mesh independence is achieved.

Mesh independence of Calibration setup simulations

The 8 mm-diameter nozzle with 3 bar upstream conditions is used for the calibration exercise mesh independence study. The mesh sizes are 500 thousand, 1 million, 2 million, 4 million and 8 million cells. The result of the mesh independent study are shown in Table G.1 and Figure G.1.

Table G.1 Calibration exercise Mesh independence data

Calibration exercise (case 3bar, 8mm)					
Mesh size	Performance parameter, f (Mass flow rate)	Order of Convergence, z	GCI 12	GCI 23	Asymptotic range
499110	0.2232	-	-	-	-
998 210	0.2194	-	-0.1019	-	-
1 996 306	0.2162	-0.263	-0.0324	0.0543	1.041
3 982 612	0.2153	-1.907	-0.0094	-0.0067	1.015
7 985 640	0.2149	-1.074	-	-0.0045	1.004

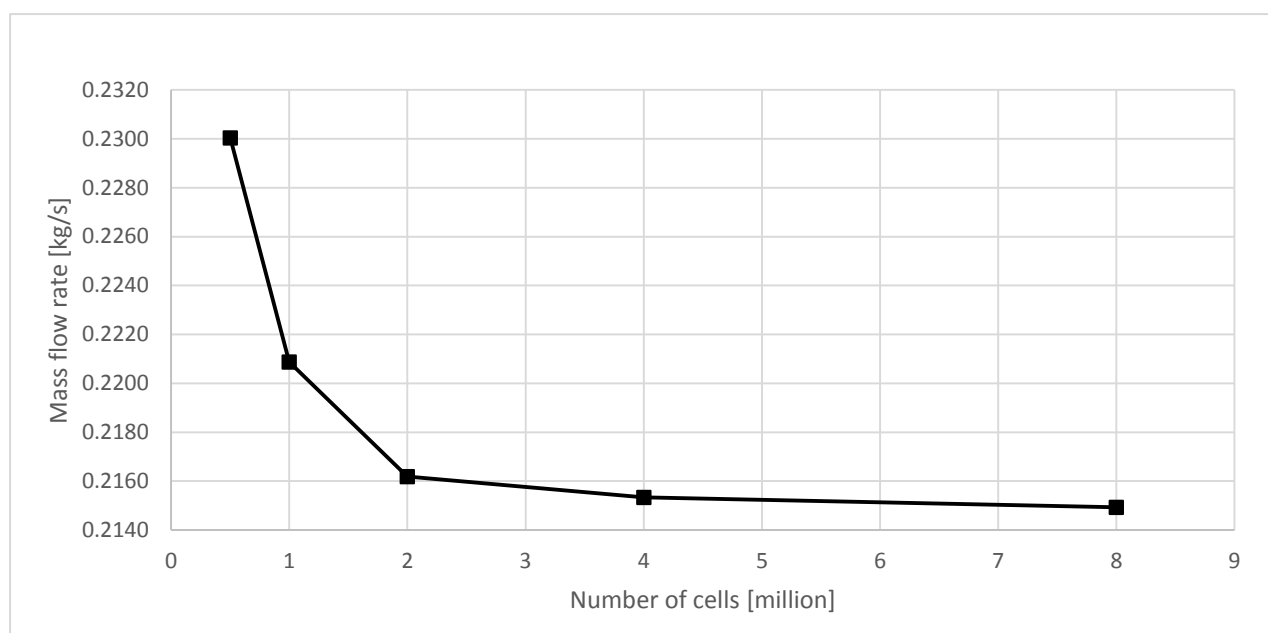


Figure G.1 Calibration exercise mesh independence result

The first three performance parameters have an asymptotic ranges of approximate by one. This means that 2 million cell mesh is sufficiently fine and that mesh independence has been achieved at 2 million cells.

Numerical method Mesh independence

The selected condition for mesh independence study of the Numerical method (in Chapter 4) is the 3 bar upstream and 2000 rpm shaft speed for the labyrinth 3D. The mesh sizes are 1 million, 2 million, 4 million, 8 million and 16 million cells. The result of the mesh independent study is show in Table G.2 and Figure G.2.

Table G.2 Numerical method Mesh independence data

Numerical method (case 3bar at 2000 rpm)					
Mesh size	Performance parameter, f (Mass flow rate)	Order of Convergence, z	GCI 12	GCI 23	Asymptotic range
1 000 416	0.004307	-	-	-	-
2 000 560	0.004204	-	-0.0680	-	-
4 001 256	0.004146	-0.837	-0.0214	-0.0390	1.025
8 002 212	0.004134	-2.322	-0.0045	-0.0043	1.014
16 004 026	0.004132	-2.107	-	-0.0011	1.003

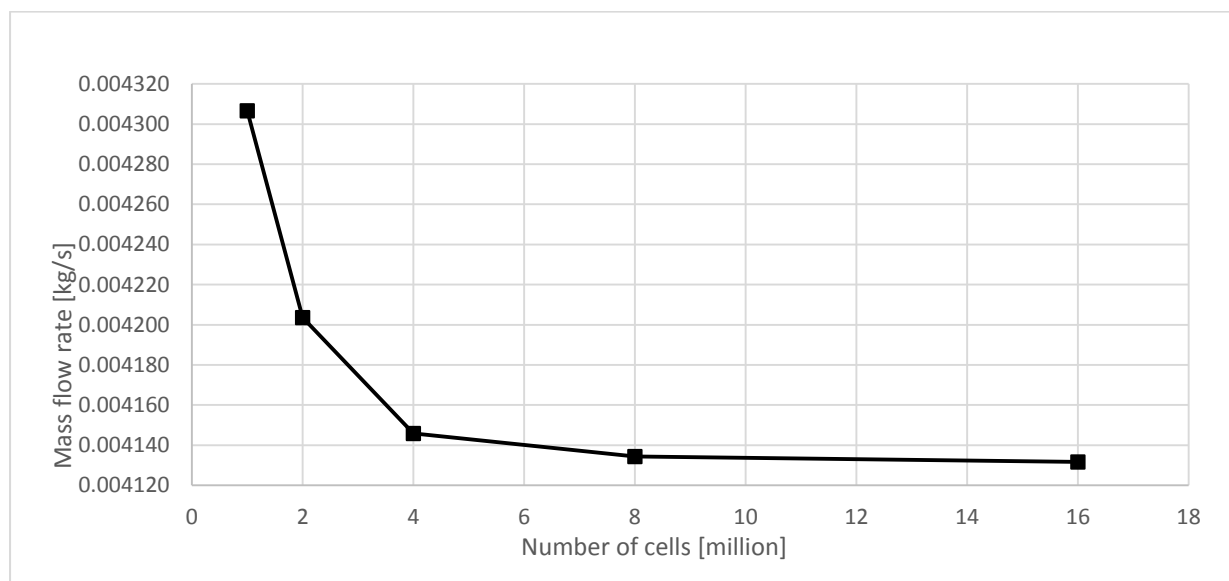


Figure G.2 Numerical method mesh independence result

The first three performance parameters have an asymptotic range is approximate one for the 4 million cell mesh and finer. This means that the 4 million cell mesh is fine enough.

Appendix H – Labyrinth Seal Results

Table H.1 Labyrinth seal Experimental Results – Mass flow rate

Experimental method - Mass flow rate [x10E-3 kg/s] for various Shaft speeds											
Pressure Upstream [kPa]	Shaft speed [x1000 rpm]										
	0	1	2	3	4	5	6	7	8	9	10
100	2.002	2.002	2.002	2.002	2.003	2.005	2.008	2.012	2.018	2.025	2.034
200	3.085	3.085	3.086	3.087	3.089	3.092	3.097	3.103	3.112	3.122	3.137
300	4.145	4.146	4.146	4.148	4.151	4.155	4.161	4.170	4.182	4.196	4.215
400	5.216	5.216	5.217	5.218	5.221	5.226	5.234	5.244	5.258	5.277	5.299
500	6.288	6.288	6.291	6.293	6.296	6.302	6.311	6.321	6.340	6.363	6.388

Table H.2 Labyrinth Numerical Results – Mass flow rate

Numerical method - Mass flow rate [x10E-3 kg/s] for various Shaft speeds											
Pressure Upstream [kPa]	Shaft speed [x1000 rpm]										
	0	1	2	3	4	5	6	7	8	9	10
100	2.031	2.031	2.031	2.032	2.033	2.035	2.038	2.042	2.048	2.055	2.064
200	3.136	3.136	3.137	3.138	3.139	3.143	3.147	3.154	3.162	3.173	3.187
300	4.227	4.227	4.228	4.229	4.231	4.236	4.242	4.251	4.262	4.277	4.296
400	5.318	5.318	5.318	5.320	5.323	5.329	5.337	5.348	5.362	5.381	5.404
500	6.413	6.413	6.414	6.416	6.419	6.426	6.435	6.449	6.466	6.489	6.517

Table H.3 Labyrinth seal Percentage difference between Experimental and Numerical methods

Percentage difference [%] between Experimental and Numerical methods											
Pressure Upstream [kPa]	Shaft speed [x1000 rpm]										
	0	1	2	3	4	5	6	7	8	9	10
100	1.45	1.45	1.46	1.47	1.47	1.48	1.49	1.48	1.49	1.49	1.48
200	1.62	1.62	1.62	1.62	1.61	1.61	1.61	1.60	1.60	1.61	1.59
300	1.93	1.93	1.92	1.91	1.90	1.90	1.90	1.89	1.90	1.90	1.89
400	1.91	1.91	1.91	1.92	1.92	1.92	1.92	1.94	1.94	1.93	1.95
500	1.94	1.94	1.91	1.92	1.92	1.93	1.93	1.98	1.96	1.95	1.99

Table H. 4 Labyrinth CFD Velocity components

Shaft speed [x1000 rpm]	Velocity components [m/s]		
	X - Component (ΔP)	Y - Component (Rotation)	Magnitude
0	5.10	0.00	5.10
1	5.10	0.03	5.10
2	5.10	0.08	5.10
3	5.10	0.15	5.11
4	5.10	0.23	5.11
5	5.10	0.33	5.11
6	5.10	0.43	5.12
7	5.10	0.54	5.13
8	5.10	0.66	5.15
9	5.10	0.79	5.16
10	5.10	0.93	5.19

Appendix I – Brush seal Results

Table I.1 Brush seal Experimental Results – Mass flow rate

Experimental method - Mass flow rate [x10E-3 kg/s] for various Shaft speeds											
Pressure Upstream [kPa]	Shaft speed [x1000 rpm]										
	0	1	2	3	4	5	6	7	8	9	10
100	1.880	1.882	1.883	1.885	1.887	1.889	1.890	1.895	1.900	1.905	1.910
200	2.890	2.892	2.893	2.896	2.898	2.899	2.900	2.910	2.920	2.930	2.940
300	3.880	3.881	3.884	3.886	3.888	3.889	3.890	3.903	3.915	3.927	3.940
400	4.847	4.850	4.853	4.856	4.859	4.862	4.865	4.880	4.895	4.910	4.924
500	5.823	5.826	5.829	5.833	5.836	5.838	5.841	5.861	5.880	5.900	5.919

Table I.2 Brush seal Numerical Results – Mass flow rate

Numerical method - Mass flow rate [x10E-3 kg/s] for various Shaft speeds											
Pressure Upstream [kPa]	Shaft speed [x1000 rpm]										
	0	1	2	3	4	5	6	7	8	9	10
100	1.930	1.932	1.933	1.935	1.937	1.938	1.940	1.945	1.950	1.955	1.960
200	2.970	2.972	2.973	2.975	2.977	2.978	2.980	2.990	3.000	3.010	3.020
300	3.990	3.992	3.993	3.995	3.997	3.998	4.000	4.013	4.025	4.038	4.050
400	4.990	4.993	4.997	5.000	5.003	5.007	5.010	5.025	5.040	5.055	5.070
500	6.000	6.003	6.007	6.010	6.013	6.017	6.020	6.040	6.060	6.080	6.100

Table I.3 Brush seal Percentage difference between Experimental and Numerical methods

Percentage difference [%] between Experimental and Numerical methods											
Pressure Upstream [kPa]	Shaft speed [x1000 rpm]										
	0	1	2	3	4	5	6	7	8	9	10
100	2.59	2.59	2.60	2.58	2.57	2.57	2.58	2.57	2.57	2.56	2.55
200	2.69	2.69	2.69	2.67	2.65	2.67	2.68	2.66	2.66	2.65	2.64
300	2.76	2.76	2.74	2.73	2.73	2.74	2.75	2.74	2.74	2.73	2.72
400	2.87	2.87	2.88	2.89	2.89	2.89	2.89	2.88	2.88	2.87	2.88
500	2.95	2.95	2.96	2.95	2.95	2.97	2.98	2.97	2.97	2.96	2.97

Table I.4 Brush seal CFD - Velocity components

Shaft speed [x1000 rpm]	CFD - Velocity components [m/s]		
	X - Component (ΔP)	Y - Component (Rotation)	Magnitude
0	4.866	0.000	4.866
1	4.866	0.083	4.867
2	4.866	0.166	4.869
3	4.866	0.249	4.872
4	4.866	0.332	4.877
5	4.866	0.415	4.884
6	4.866	0.498	4.891
7	4.866	0.581	4.901
8	4.866	0.664	4.911
9	4.866	0.748	4.923
10	4.866	0.832	4.937

Appendix J – Calibration Exercise Results

J.1. Calibration Exercise Results

Table J.1 Experimental Results – Mass flow rate

Experimental method - Mass flow rate [kg/s] for various Nozzle diameters												
Pressure Upstream [kPa]	Nozzle diameter [mm]											
	1	2	3	4	5	6	7	8	9	10	11	12
100	6.99E-03	1.40E-02	2.10E-02	2.81E-02	3.51E-02	4.22E-02	4.93E-02	5.63E-02	6.33E-02	7.03E-02	7.72E-02	8.41E-02
200	1.59E-02	3.31E-02	5.04E-02	6.78E-02	8.51E-02	1.02E-01	1.19E-01	1.34E-01	1.47E-01	1.59E-01	1.68E-01	1.77E-01
300	2.48E-02	5.22E-02	7.98E-02	1.07E-01	1.35E-01	1.62E-01	1.89E-01	2.12E-01	2.31E-01	2.47E-01	2.59E-01	2.69E-01
400	3.36E-02	7.13E-02	1.09E-01	1.47E-01	1.85E-01	2.21E-01	2.58E-01	2.89E-01	3.14E-01	3.35E-01	3.49E-01	3.60E-01
500	4.25E-02	9.04E-02	1.38E-01	1.86E-01	2.34E-01	2.80E-01	3.27E-01	3.66E-01	3.96E-01	4.20E-01	4.35E-01	4.46E-01
600	5.15E-02	1.10E-01	1.68E-01	2.26E-01	2.83E-01	3.39E-01	3.95E-01	4.41E-01	4.74E-01	5.00E-01	5.13E-01	5.22E-01
700	6.04E-02	1.29E-01	1.97E-01	2.65E-01	3.33E-01	3.98E-01	4.63E-01	5.16E-01	5.44E-01	5.63E-01	5.59E-01	5.37E-01

Table J.2 Numerical Results – Mass flow rate

Numerical method - Mass flow rate [kg/s] for various Nozzle diameters												
Pressure Upstream [kPa]	Nozzle diameter [mm]											
	1	2	3	4	5	6	7	8	9	10	11	12
100	7.10E-03	1.42E-02	2.13E-02	2.84E-02	3.55E-02	4.26E-02	4.97E-02	5.68E-02	6.39E-02	7.10E-02	7.81E-02	8.52E-02
200	1.61E-02	3.35E-02	5.10E-02	6.85E-02	8.59E-02	1.03E-01	1.20E-01	1.35E-01	1.48E-01	1.60E-01	1.70E-01	1.79E-01
300	2.51E-02	5.29E-02	8.07E-02	1.09E-01	1.36E-01	1.63E-01	1.90E-01	2.13E-01	2.33E-01	2.50E-01	2.62E-01	2.72E-01
400	3.41E-02	7.22E-02	1.10E-01	1.49E-01	1.87E-01	2.23E-01	2.60E-01	2.92E-01	3.18E-01	3.39E-01	3.54E-01	3.66E-01
500	4.31E-02	9.16E-02	1.40E-01	1.89E-01	2.37E-01	2.84E-01	3.30E-01	3.70E-01	4.02E-01	4.29E-01	4.46E-01	4.60E-01
600	5.21E-02	1.11E-01	1.70E-01	2.29E-01	2.87E-01	3.44E-01	4.01E-01	4.48E-01	4.87E-01	5.18E-01	5.38E-01	5.53E-01
700	6.11E-02	1.30E-01	1.99E-01	2.69E-01	3.38E-01	4.04E-01	4.71E-01	5.27E-01	5.71E-01	6.08E-01	6.30E-01	6.47E-01

Table J.3 Percentage difference between Experimental and Numerical methods

Percentage difference [%] between Experimental and Numerical methods												
Pressure Upstream [kPa]	Nozzle diameter [mm]											
	1	2	3	4	5	6	7	8	9	10	11	12
100	1.492	1.363	1.233	1.104	0.974	0.845	0.715	0.815	0.915	1.015	1.115	1.215
200	1.434	1.316	1.197	1.079	0.960	0.842	0.724	0.824	0.925	1.025	1.126	1.226
300	1.380	1.272	1.165	1.057	0.949	0.841	0.734	0.856	0.978	1.101	1.223	1.345
400	1.341	1.264	1.187	1.110	1.033	0.956	0.879	0.894	1.110	1.325	1.541	1.756
500	1.284	1.262	1.241	1.219	1.197	1.176	1.154	1.202	1.650	2.098	2.546	2.984
600	1.236	1.279	1.321	1.364	1.406	1.449	1.491	1.556	2.571	3.586	4.600	5.615
700	1.223	1.309	1.396	1.482	1.569	1.655	1.741	1.995	4.731	7.468	11.204	16.940

Table J.4 Upstream Velocity of Numerical Method

Upstream Velocity [m/s] of Numerical Method												
Pressure Upstream [kPa]	Nozzle diameter [mm]											
	1	2	3	4	5	6	7	8	9	10	11	12
100	2.50	5.14	7.78	10.43	12.91	15.66	18.26	20.66	22.86	24.82	27.46	28.42
200	2.60	5.42	8.24	11.06	13.87	16.62	19.36	21.82	23.98	25.92	27.47	28.87
300	2.70	5.70	8.69	11.69	14.67	17.57	20.47	22.97	25.10	26.91	28.22	29.33
400	2.75	5.83	8.91	12.01	15.08	18.05	21.02	23.55	25.65	27.41	28.59	29.55
500	2.78	5.92	9.05	12.20	15.32	18.33	21.35	23.90	25.99	27.71	28.82	29.69
600	2.80	5.97	9.14	12.32	15.48	18.52	21.57	24.13	26.21	27.91	28.97	29.78
700	2.82	6.01	9.21	12.41	15.59	18.66	21.73	24.30	26.37	28.05	29.07	29.84

Appendix K - Sample Conversions

This section shows an example of how the solvers converge in the simulations. Figure K.1 shows the residuals of the simulation with their conversions rates for the Labyrinth seal at 1 bar upstream and shaft speed at 1000 rpm. The graph shows that all the energy and momentum solvers converge to an order $10E-5$ of after 10 000 iterations.

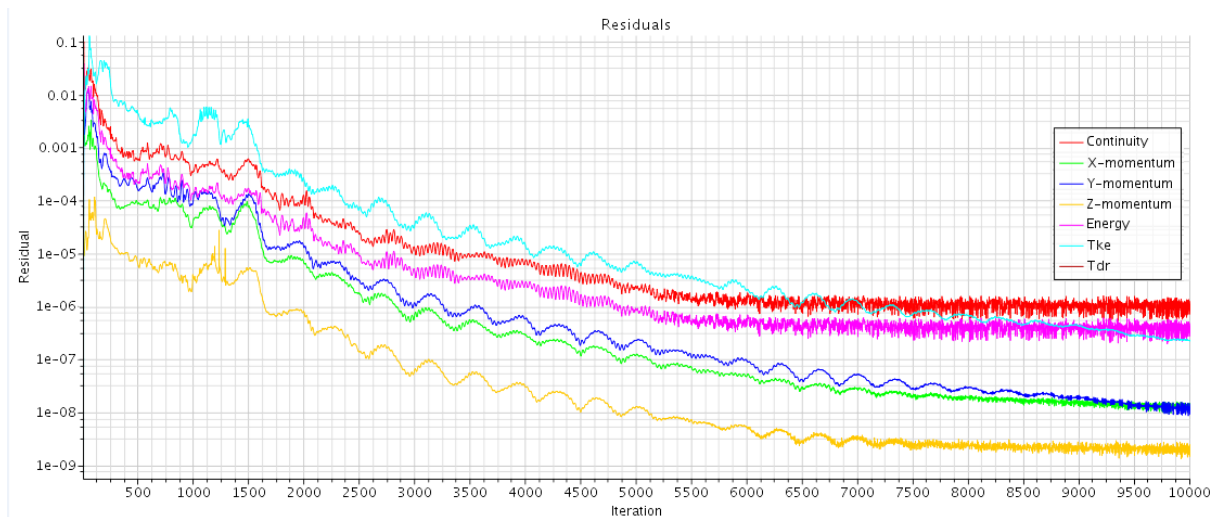


Figure K.1 Graph of residuals after 10 000 iterations

The sample converges show that a solvers stoppage criteria can be set at $10E-5$ converges for each simulation to save on computational time.